THE RELATIONSHIP OF IMPACT PROPERTIES TO MICROSTRUCTURE FOR A SERIES OF ALLOY STEELS CONTAINING 0.3 WT.% CARBON

by GEOFFREY EDWIN OSBORNE,

B.Sc.(Eng.), A.R.S.M.

ABSTRACT

Five alloying elements, silicon, nickel, phosphorus, tin and nitrogen have been added singly to a 0.3 weight per cent carbon steel. Consequent changes in microstructure owing to the presence of these elements have been observed using transmission electron microscopy of thin foils of each alloy in two fully-hardened-and-well-tempered conditions. Fracturing behaviour has been examined using the Charpy impact test on standard Izod-notched specimens.

An attempt is made to correlate various microstructural and impact fracture parameters and it is remarked that microstructural changes are usually relatively slight whereas corresponding changes in impact fracture ductile/brittle transition curves may be considerable. In a number of cases, however, the changes in microstructure could account for the observed fracture characteristics.

CONTENTS

		Page
Title		1
Abstract		2
Contents		3
Chapter 1.	Introduction	9
1.1.	Introduction	9
1.1.1.	Brittle fracture compared with ductile fracture	11
1.1.2.	Measurement of fracture characteristics	12
1.1.3.	Methods of observation of fracture phenomena	13
1.2.	Effects of microstructure	16
1.2.1.	Carbide morphology	16
1.2.2.	Grain size	16
1.2.3.	Alloying	18
1.2.4.	Cooling rate	20
1.3.	Theory of fracture	20
1.3.1.	Crack propagation	20
	(i) Griffith-Orowan	20
	(ii) Mechanisms of energy dissipation	21
	(iii) Fracture mode	22
1.3.2.	Crack nucleation	23
	(i) Inclusion mechanisms	25
	(ii) Location of crack nucleus	26
1.3.3.	Factors favouring brittle fracture	26

1.4.	Summary of possible causes of brittle fracture in well-tempered low alloy steels	29
1.4.1.	Grain size	29
1.4.2.	Subgrain size	29
1.4.3.	Carbide size	30
1.4.4.	Segregation	30
1.4.5.	Solution effects	30
Chapter 2.	Materials, Apparatus and techniques	31
2.1.	Alloy composition	31
2.1.1.	General metallurgy	33
2.1.2.	Constitution of the six alloys	33
2.1.3.	Optical metallography	35
2.2.	Electron microscopy	36
2.2.1.	Resolution	37
2.2.2.	Depth of field	38
2.3.	Sectioning	38
2.4.	Heat treatment	40
2.4.1.	Furnace for austenitising	40
2.4.2.	Furnace for tempering	43
2.4.3.	Temperature control and measurement	46
2.4.4.	Furnace atmosphere	47
2.5.	Grinding	48
2.6.	Electropolishing	51
2.6.1.	Power supply unit	51
2.6.2.	Electropolishing apparatus	54

2.6.2. (i)	Perspex framework	54
2.6.2.(ii)	Electrode design	56
2.6.3.	Optimum polishing conditions	59
2.6.4.	Primary electropolishing	60
2.6.5.	Secondary electropolishing	62
2.6.6.	Mounting	64
2.7.	Replica techniques	65
2.7.1.	Shadowing	66
2.7.2.	Carbon coating	66
2.7.3.	Mounting of replicas	67
2.8.	The electron microscope	67
2.8.1.	Image contrast	68
2.9.	Electron-optical theories of transmission image contrast	70
2.10.	Image interpretation for thin foils	72
2.11.	Selected area electron diffraction	74
2.12.	Image interpretation for replicas	75
2.13.	Notched bar impact testing	76
2.13.1.	Testpiece design	76
2.13.2.	Testing machine and procedure	77
2.13.3.	Interpretation of results	79
Chapter 3.	Experimental Results	81
3.1.	Characterisation of microstructure	81
3.1.1.	Optical microscopy	81
3.1.2.	Electron microscopy after tempering for 1 hr.	81

(i) Plain carbon steel, alloy No. 1 81

(ii) Silicon steel, alloy No. 2 89

(iii) Nickel steel, alloy No. 3 93

(iv) Phosphorus steel, alloy No. 4 93

(v) Tin steel, alloy No. 5 100

(vi) Nitrogen steel, alloy No. 6 100

3.1.3. Electron microscopy after tempering for 17 hrs. 107

(i) Plain carbon steel, alloy No. 1 107

(ii) Silicon steel, alloy No. 2 107

(iii) Nickel steel, alloy No. 3 114

(iv) Phosphorus steel, alloy No. 4 114

(v) Tin steel, alloy No. 5 121

(vi) Nitrogen steel, alloy No. 6 121

3.1.4. Selected area electron diffraction results 128

(i) Ferrite matrix 129

(ii) Cementite precipitates 134

3.2. Characterisation of fracturing 136

3.2.1. Fractography 136

3.2.2. Charpy results 139

(i) Plain carbon steel, alloy No. 1 147

(ii) Silicon steel, alloy No. 2 147

(iii) Nickel steel, alloy No. 3 148

(iv) Phosphorus steel, alloy No. 4 148

(v) Tin steel, alloy No. 5 149

	(vi) Nitrogen steel, alloy No. 6	149
	(vii) Summary of notched-bar impact test results	150
Chapter 4.	Discussion	151
4.1.	Composition	151
4.2.	Thermal history	151
4.2.1.	Tempering times	152
4.2.2.	Rate of cooling from tempering temperature	152
4.3.	Microstructural effects	153
4.4.	Solution and segregation effects	153
4.5.	Impact fracture characteristics	154
4.6.	Effects of alloying elements on fracture characteristics after tempering	159
4.6.1.	Effect of alloying elements on TT after tempering	159
4.6.2.	Effect of alloying elements on ΔE after tempering	162
4.7.	Effect of alloying elements on subgrain and carbide sizes during tempering	163
4.7.1.	Effect on subgrain size, D	163
4.7.2.	Effect on carbide length, L	163
4.7.3.	Comparison of effects on subgrain and carbide sizes	164
4.8.	Microstructural changes during tempering	165
4.9.	Analysis of effects of microstructural changes on impact parameters	166

4.10.	Effect of subgrain size on impact parameters	172
4.11.	Effect of carbide size on impact parameters	172
4.12.	Effect of alloying elements on impact parameters	173
4.12.1.	Silicon	173
4.12.2.	Nickel	173
4.12.3.	Phosphorus	173
4.12.4.	Tin	173
4.12.5.	Nitrogen	174
4.12.6.	Concluding remarks	174
Chapter 5.	Summary	175
Appendix 1.	Calculation of solute density possible on boundaries	176
Appendix 2.	(a) Acknowledgements	179
	(b) Statement	180
Appendix 3.	References	181

CHAPTER 1. INTRODUCTION

1.1 Introduction

The phenomenon of brittle fracture has been in evidence in steels from the earliest days of the use of steel in engineering structures. Shank (1) described 28 cases of catastrophic brittle failure of steel structures between 1886 and 1952, e.g. (2). He cites evidence from the enquiries into the failures to show that they were brittle in nature.

The reason why brittle fracture is so dangerous is because of the lack of warning of imminent failure, and the extremely rapid propagation of the fracture once nucleated. This can easily give rise to almost explosive failure with consequent injuries to personnel.

The use of steel in armaments and armour caused brittle fracture to be of great consequence to military authorities. N. P. Allen (3) mentioned the importance of brittle fracture in connection with tank armour during the second world war. He emphasised the importance of strain rate, as many samples of armour behaved in a brittle manner under impact from shells but appeared quite tough in static tests. It was found that alloy steels, if given precise and proper heat treatments gave good results, which in practice, however, were dependent on the precision of control of the heat treatment and the cleanliness of the steel.

Paul (4) has detailed the interest of armies recently in brittle fracture since temperatures down to -40°F might be encountered in service. Intensive work in this field since 1945 had, by 1953, increased the toughness of armour severalfold and had even doubled the muzzle velocity of some guns, with consequent increases in the stresses in the barrels. However, the wall thickness of barrels had been reduced to lessen the weight and there was also a desire to lower the alloying additions to the steels without adversely affecting the other qualities. This was successful and the trends are continuing. It is not necessary to have very much ductility at -40°F, but a certain amount is necessary to prevent brittle failure in service, which obviously must not be allowed to occur.

There are several conventional approaches to the improvement of toughness in steels. Trial-and-error experimentation to discover compositions of steels which possess low ductile/brittle transition temperatures has been relatively successful and information is now available on those elements and combinations of elements which are beneficial and those which are deleterious. However, little real understanding of the mechanisms by which different elements have their effects has yet been obtained. This is mainly due to the extreme complexity of the systems under observation, and the wide range of experimental

techniques which may be applied to the problem. These techniques range from fracture toughness testing to observations of microstructure using optical microscopy. Electron microscopy has been applied to the subject largely indirectly in that it has not often been used in conjunction with one other major method. This investigation seeks to correlate results from thin foil transmission electron microscopy with standard Charpy impact test results.

1.1.1 Brittle fracture compared with ductile fracture

Brittle fracture is defined here as the propagation of a crack such that the plastic deformation on a macroscopic scale is negligible. It has a number of other characteristics which include the very rapid velocity of propagation, the relatively smooth fracture surfaces produced and the negligible energy absorbed during fracture. Conversely, ductile fracture is characterised by possibly extensive macroscopic plastic deformation, 'fibrous' or rough appearance of the fracture surface, relatively slow crack propagation, and high energy absorption during fracture.

Both types of fracture may be considered as the resultant of two processes, crack nucleation and crack propagation.

Apart from the determination of those elements which improve ductility and those which make it worse, and the

study of the reasons for this from the microstructural point of view, the majority of research has been centred on the mechanisms of crack nucleation and propagation both from the theoretical point of view and from observation of the fracture surfaces.

1.1.2 Measurement of fracture characteristics

One method of obtaining quantitative data on fracture processes is the use of the notched-bar impact test (Charpy or Izod test) which is described fully in a later section (2.13). A recent alternative to this is 'fracture toughness testing' which is often preferred to the Charpy type.

Normally in the Charpy impact test only the energy absorbed during fracture of a standard test-piece at a particular temperature is recorded. It is possible, however, to instal strain gauges to reveal the load on the test-piece during fracture. Wilshaw and Pratt (5) tested mild steel Charpy specimens at temperatures ranging from +100°C to -196°C and obtained two conclusions :

(1) A transition was observed from ductile tearing at the notch root to internal cleavage.

(2) A decrease in fracture load was coincident with the onset of mechanical twinning during fracture.

When results have been obtained over a range of temperatures the energy absorbed may be plotted against

the test-piece temperature to derive a curve which has a characteristic shape for steels. The energy absorbed during fracture is usually observed to increase rapidly over a limited range of temperature. A 'transition temperature' may be defined on this transition region of the graph as signifying the changeover from brittle to ductile fracture. Various definitions of this temperature have been used and are discussed later.

1.1.3 Methods of observation of fracture phenomena

The primary technique for visual characterisation of a fracture involves the study of the topography of the fracture surface. Optical microscopy is of little value for this purpose in view of its inadequate depth of focus. The introduction of electron microscopy, however, with its very large depth of focus made the serious investigation of fracture surfaces a practical possibility.

Electron microscopy of fracture surfaces is discussed by Pelloux and McMillan (6) who described the types of fracture and their microscopic appearance. In particular they note that in fact most 'brittle' fractures reveal the presence of some plastic deformation on the fracture surfaces.

Various modes of fracture are defined by Pelloux and McMillan (6), namely :

(i) Intergranular brittle,

(ii) Intergranular ductile,

(iii) Transgranular along crystallographic planes (either by cleavage or by corrosion),

(iv) Transgranular by the formation and coalescence of microvoids,

(v) Slow progression of a fatigue crack.

With regard to the types of fracture which may occur in impact test bars, there are several topographical features which are characteristic of particular fracture modes.

In cleavage fracture which is common in steels at low temperatures, many cleavage planes are involved and the steps between these planes form a pattern, usually referred to as 'river markings'. The direction of the river markings gives the local direction of cleavage which can vary widely between neighbouring regions. The transition region between two cleavage planes may be a secondary cleavage plane or a region of shear rupture, i.e. tear ridges. Where cleavage intersects a deformation twin the resultant phenomenon is termed a 'tongue' and occurs by cleavage of the twin. Both these effects (river markings and tongues) are observed in Figs. 61 to 64.

Plastic fracture in most metals occurs by the formation and coalescence of microvoids. This results in a dimpled

fracture surface where each dimple is the result of one void. The fracture path is usually transgranular but may be intergranular, in which case the macroscopic plastic deformation is negligible. The shapes of the dimples can give information on the stress configuration resulting in fracture, i.e. whether it is normal, shear, or tear.

Brittle intergranular fracture occurs under certain conditions, whereupon the fracture surface consists of grain boundaries and its appearance depends on the shape and size of the grains involved.

As an alternative to the study of the fracture surface it has become possible in recent years to make use of the technique of ultra-high-speed photography to follow the propagation of the crack itself. As an example of this approach, Verbraak (7) found that the propagation of brittle fracture is discontinuous, advancing by a series of equal steps. The length of the advances and the period between them were observed to increase with temperature. When the main fracture was stationary, isolated cracks ahead of it were observed to grow.

A shock-wave was emitted as each fracture step occurred and the brittle fracture was observed to attain its final propagation velocity only 10 to 30 microseconds after initiation.

Strain birefringent coatings may be applied to the

surfaces of test-pieces to allow stress fields to be photographed.

1.2 Effects of microstructure

1.2.1 Carbide morphology

The effect of steel microstructure on impact properties was discussed by Rinebolt (8). He used Charpy V-notched specimens to compare the susceptibilities to brittle fracture of spheroidite structures produced by decomposition (tempering) of martensite, spheroidisation of pearlite, and normalising. The spheroidised pearlite had the highest transition temperature, while the tempered martensitic spheroidite and the normalised structure possessed approximately equally low transition temperatures. The maximum energies revealed a different sequence. The spheroidite produced from martensite had the highest maximum energy and the normalised structure had the lowest value. Thus tempered martensitic spheroidite possesses the best properties, namely low transition temperature and high maximum energy values.

1.2.2 Grain size

Hodge et al (9) (using the Charpy keyhole-notched test-piece) found that the transition temperature of ferrite was lowered by about 25°F (13.9°C) per grain size number as the grain size decreased.

Meakin and Petch (10) discuss the effect of grain size on ductility. The yield and flow stress is raised by decreasing the grain size according to the empirical relationship involving (grain diameter)$^{-0.5}$ and this favours brittleness. However, a fine grain size also limits the ease of nucleation of a crack, thus favouring ductility. Meakin and Petch mention the problem of whether the subgrain diameter or the grain diameter is the ruling parameter but do not reach a conclusion.

Sakui and Mori (11) note the effect of grain size on elongation under impact tensile conditions. Fine-grained specimens showed much less ductility of a macroscopic scale than did coarser-grained specimens. This is opposite to the result obtained from the static tensile test when finer-grained specimens showed larger elongations than did coarse-grained ones. They called the effect under impact conditions pseudo-brittle fracture, as the fine-grained specimens, although showing negligible macroscopic elongation did reveal plastic flow locally at the fracture surface.

Baeyertz et al (12) used quenched and tempered steels which had been tempered differently to develop different hardnesses, and in 1950 (13) studied the relationship between ferrite grain structure and impact properties of 0.8% C. spheroidite. Prior austenite grain size was found to have no effect on the final transition curves. However

the small, non-equiaxed ferrite grains in spheroidites from tempered martensite gave considerably lower transition temperatures than the larger, equiaxed ferrite grain structure of spheroidite produced from pearlite. The difference in transition temperatures amounted to approximately 120°F (67°C). They conclude that the fracture characteristics are influenced by the shape of the ferrite grains.

1.2.3 Alloying

Certain alloying elements were found to give similar effects in each of the spheroidite structures (tempered martensite, spheroidised pearlite, normalised) studied by Rinebolt (8). Carbon, phosphorus and silicon raised the transition temperature, whilst manganese and nickel lowered it. Rinebolt and Harris (14) studied pearlitic steels and confirmed the effects of carbon, phosphorus, silicon, manganese and nickel, adding that molybdenum and copper also raised the transition temperature.

When brittle fracture occurs after heat treatment (e.g. hardening and tempering), precipitation or segregation at grain boundaries is often suspected. Thus, microhardness measurements on grain boundaries have shown a higher hardness than that in the body of the grains. Westbrook and West (15) proposed that solute segregation was responsible for the higher grain boundary hardness.

Ainslie et al (16) reported an observation of dislocation tangles at grain boundaries in iron containing sulphur, and concluded that this was due to grain boundary segregation. Low (17), however, failed to verify this finding; in addition he was unable to detect, using electron microscopy, any evidence for segregation to the grain boundary regions in a number of steels in various heat treatment conditions.

Allen (3) mentions work between 1951 and 1961 on the effects of alloying elements on the transition temperature of iron. For pure iron the transition temperature is -15°C and is sharply defined. Small additions of oxygen, nitrogen and phosphorus raise the transition temperature. The presence of carbides also raises it; the coarser the carbides are, the greater is the effect. Manganese additions lower the transition temperature and refine the structure.

Hodge et al (9) obtained quantitative results on the effects of five elements on the transition temperature :

ELEMENT	CHANGE IN TRANSITION TEMPERATURE	
symbol	direction of change, up or down	magnitude of change, in °F per 0.01% solute
C	up	3.5°
P	up	8.5°
Si	up	0.5°
Mn	down	0.07°
Ni	down	2.3° (up to 0.3% Ni, then levelled off)

1.2.4 Cooling rate

Baeyertz, Craig and Sheehan (18) investigated the effect of cooling rate after tempering on the impact properties of a series of steels and found that embrittlement could occur if the cooling rate were too slow. They concluded that a water quench after tempering may, for some steels, be too slow to avoid embrittlement.

1.3 Theory of fracture

1.3.1 Crack propagation

1.3.1(i) Griffith/Orowan Theory

In 1921, A. A. Griffith (19) published a theory of fracture which is now known to be applicable only to the type of material with which he worked, which was glass. In such a material, which fractures in a totally brittle manner, the decrease in potential energy during fracture (i.e. external work done) may be equated to the energy of the new surfaces created. Thus, the breaking stress, $\sigma_b = \left(\frac{2 E \gamma}{\pi c} \right)^{\frac{1}{2}}$, where E is Young's modulus, γ is the surface energy and c is the critical crack length which must be exceeded before fracture can occur at σ_b.

Both Orowan (20) and Irwin (21) extended the Griffith theory to materials where irreversible deformation occurs during fracturing. They replaced the surface energy term in the Griffith equation by the sum of the energy of the

new surface and the work of plastic deformation. The breaking stress is then given by the following equation :

$$\sigma_b = \left(\frac{2 E \gamma}{\beta \pi c} \right)^{\frac{1}{2}} ;$$

where $\beta = \left(1 - \frac{2 E \alpha}{\pi c} \right)$.

The terms σ_b, E, γ and c are as defined above and α is a constant such that $\alpha \sigma_b^2$ represents the plastic work done during fracturing.

McLean (22) inserted values of stress for crack propagation in a brittle steel in the Griffith equation and the 'surface energy' calculated was about 30 times larger than that which would be reasonable. From this he concluded that most of the energy dissipated during fracture went as plastic deformation at the crack tip. Even in a fracture by brittle cleavage the energy dissipated is largely due to the plastic deformation which occurs locally.

1.3.1(ii) Mechanisms of energy dissipation

The mechanisms of dissipation of energy during brittle fracture are discussed by Bartenev (23). He divided the total energy into three components :

(1) losses due to plastic deformation

(2) losses due to converting elastic energy into kinetic energy as the surfaces separate

(3) energy required to break atomic bonds at the crack tip.

Bartenev showed that most of the energy absorbed during fracture was due to mechanical losses, i.e. (1) and (2), and these were much greater than the surface free energy of the surfaces created.

McEvily and Johnston (24) stated an argument for the process of cross slip being the ruling factor in determining the ductile/brittle transition temperature.

During the actual process of brittle fracture a significant amount of ductile failure occurs but only very locally. Even so, because of the speed of the propagation of the crack, local temperatures may rise [Gruntfest (25)].

1.3.1(iii) Fracture mode

Brittle fracture may occur by transgranular cleavage or by intergranular separation or by a combination of both. The process of crack nucleation may influence the mode of propagation. Thus cleavage methods of nucleation such as intersecting deformation twins may tend to result in cleavage propagation. This is supported by reports that cleavage failure repeatedly renucleates ahead of the main crack tip. Crussard et al (26) showed that in poly-crystalline aggregates, cleavage fracture is a discontinuous process. Many cleavage cracks are nucleated ahead of the main crack and these often propagate in different directions. Junction of these cracks with the main crack may occur by

secondary cleavage or by ductile failure or separation at boundaries.

If fracture is nucleated on grain or subgrain boundaries the crack will propagate along the boundary until it branches along another one or transfers to a cleavage plane.

The appearance of the fracture surface at high magnifications enables the two modes of fracture to be distinguished. Cleavage is characterised by flat facets and frequent tongues and river markings (described earlier); whereas intergranular fracture surfaces do not show river markings or tongues but may exhibit very flat dimples owing to the presence of precipitate particles on the boundaries.

1.3.2 Crack nucleation

Meakin and Petch (10) state the five generally-accepted mechanisms which could nucleate a crack. Controversy arises if it is necessary to decide which one is operative in a particular system.

(1) Slip band / grain boundary impingement [Zener (27)].

(2) Coalescence of dislocations on intersecting slip planes. Initially proposed by Cottrell for α-iron (see ref. 10).

(3) Twin / twin intersection [Cahn (28); Hull (29)].

(4) Slip band intersections [Argon and Orowan (30)].

(5) Separation along a slip plane due to discontinuity of strain where a slip band crosses a tilt boundary [Orowan (31)].

Hull (32) discusses the arguments concerning twinning as a mechanism of crack nucleation in steels. Body-centred cubic metals are subject to deformation twinning which makes it likely that, at an early stage in stressing, twins will form and it is likely that they will intersect with twins formed a short time beforehand or with grain boundaries or precipitates.

In the case of intersecting twins the stress concentration at the intersection can be very severe and it may be relieved by slip or twinning and detwinning may sometimes occur. With grain boundaries the stress concentration may be more easily relieved by separation along the boundary than by slip. Unfortunately for this sort of theory, not much is known of the effects of alloying additions on twinning behaviour. Owen and Hull (33) discussed twin/twin intersections and slip or twin interaction with grain boundaries. It was suggested that subgrain boundaries may have as great an effect as high-angle boundaries.

The composition plane in b.c.c. metals is $\{112\}$ and the twinning direction is $\langle 111 \rangle$. The twinning shear is

$1/\sqrt{2}$ which works out as a displacement per plane of $(a/6)\langle 111\rangle$, which may be represented as a set of partial dislocations; accounting for the large strain produced in the neighbouring lattice by a twin. This strain has to be accommodated in the lattice, and will extend for a considerable distance. The rate of growth of twins is very rapid because of the large difference between the nucleation and growth stresses. Therefore, when a forming twin impinges on a barrier the stress build-up is very rapid and relaxation of this by the usual processes is virtually impossible.

Hull (32) mentioned that twins are not a very strong barrier to the passage of slip dislocations, but that they can be very strong barriers to deformation twins. Only in the case of very special circumstances (Smith et al (34)) can twins intersect each other without distortion, and therefore without stress concentration.

1.3.2(i) Inclusion mechanisms

The role of inclusions in the nucleation of cracks was discussed by Smith (35) who states that for very brittle steels, inclusions of small defects may act as the micro-cracks from which fracture is initiated. He concludes that numerous small defects can be as dangerous as a few large ones ever though the former comprise a lower volume fraction of the material.

1.3.2(ii) Location of crack nucleus

Allen (3) noted that at temperatures well above the notched-bar impact transition temperature, fracture begins at the surface, whereas at temperatures well below the transition temperature it begins below the surface.

For the standard Izod v-notch, Allen gives a figure of 1.93 x the uniaxial yield stress, (σ_y), as the maximum stress attained in the test-piece, when the nominal stress at the notch root is 0.8 x σ_y. Therefore, if fracture stress $< 1.93\ \sigma_y$, fracture begins below the surface, and if $> 1.93\ \sigma_y$ it occurs at, or very close to, the root of the notch when the local plastic strain has become comparable with that observed at fracture in a simple tensile test.

As described in Section 1.1.3(ii), ultra-high speed photography shows that brittle fracture propagates discontinuously, in a series of equal steps, and that even when the main fracture is stationary small cracks appear ahead of it.

1.3.3 Factors favouring brittle fracture

When the tip of the moving crack is considered, it is apparent that plastic deformation occurs locally. Tetelman (36) concluded, therefore, that the density of mobile dislocation sources in the neighbourhood of the crack tip is the most important parameter in the fracturing

of metals. The availability of a large number of dislocations allows substantial plastic deformation to occur during fracturing. If there are only a few dislocation sources or if the dislocations are pinned or obstructed in moving by precipitated or segregated impurities, plastic deformation will be very limited and will occur at high stress levels. The stress concentrations at interphases between phases and between grains will be very high in this case as they have not been relaxed sufficiently by plastic deformation. Under these conditions brittle fracture occurs.

Assuming the resistance to plastic deformation at the tip of the crack to be the controlling factor in propagation of the crack, Low (17) points out that this plastic deformation will be controlled by microstructure, composition and temperature. The orientation changes at grain and subgrain boundaries will obviously affect this zone of plastic deformation at the crack tip and Low states that a reduction in the grain size is therefore expected to decrease the likelihood of brittle fracture occurring (cf. Section 1.2.2). However, he also notes that if segregation of solutes or precipitation occurs at grain boundaries so as to produce regions of high resistance to plastic deformation, then these boundaries may become paths of easy crack propagation.

Solutes also affect the lattice frictional stress, σ_o,

considerably. For example, σ_0 for iron is increased by 3 tons/in^2 per 0.01 weight % carbon or nitrogen. Meakin and Petch state that this effect is one reason why purification generally decreases brittleness.

The energy required to nucleate and propagate a crack consists of the true surface energy of the new surfaces formed with the addition of the energy absorbed in plastic deformation at the tip of the crack. This total energy, γ, is called the effective surface energy by Meakin and Petch. Since a fracture of low energy is a brittle one, the total energy, γ, must be raised to minimise the likelihood of brittle fracture. Meakin and Petch assert that the locking of dislocations in b.c.c. metals interferes with the relief of stress concentration by plastic deformation, thus resulting in a low value of γ. There are plenty of slip systems available in these metals, so the dislocations in them must be obstructed or pinned or locked to account for the general lack of deformation under certain circumstances in b.c.c. metals, i.e. when they fracture in a brittle manner.

Meakin and Petch (10) used a theoretical approach and summarised factors which might be expected to favour brittle fracture. A rise in the ~~fracture~~ yield stress may occur because of the frictional stress, σ_0, increasing, and this may favour brittle fracture. Dislocation movement cannot occur

unless σ_0 is exceeded, so σ_0 is a measure of the ease of dislocation movement. The precise nature of this σ_0 is not yet established. It may be the Peierls-Nabarro stress (i.e. a true lattice resistance) or an effect of impurity segregation. σ_0 is strongly temperature-dependent and also dependent on the strain rate. This implies a strain rate dependence of the ductile/brittle transition temperature.

Another factor of importance in determining the value of the fracture stress in the stress configuration present during fracture. Triaxial tension (e.g. at the root of a notch) raises the axial tensile stress for yield and flow by a factor of almost three. The presence of a notch also introduces a strain rate effect on the σ_0 since the volume deforming is very small. These two effects, according to Meakin and Petch, raise the ductile/brittle transition temperature for steel from about -200°C without a notch, to about +20°C with a standard Izod notch.

1.4 Summary of possible causes of brittle fracture in well tempered low alloy steels

1.4.1 Grain size

Grain size has been shown to affect the transition temperature (see Sections 1.2.2 and 1.3.3).

1.4.2 Subgrain size

In alloys having a well defined subgrain structure the

spacing of the low-angle boundaries may control the plastic deformation energy, which affects the mode of fracture.

1.4.3 Carbide size

The interface between a carbide and the matrix may act as an incipient Griffith crack. Carbide length is therefore a potentially important parameter in determining brittleness.

1.4.4 Segregation

When embrittlement is not accompanied by obvious changes in microstructure, segregation of alloying elements to boundaries is frequently postulated. Such segregation has not been directly observed but some supporting evidence has been provided by microhardness measurements.

1.4.5 Solution effects

Alloying elements in solution may lead to embrittlement by raising the Peierls-Nabarro stress thereby rendering plastic deformation more difficult.

CHAPTER 2. MATERIALS, APPARATUS AND TECHNIQUES

Some of the apparatus was immediately available, but a considerable amount had to be constructed or acquired specifically for this investigation.

2.1. Alloy composition

The types of steel used in this investigation were similar to those which might be used for tank armament and armour (see ref. 4). Brittleness in any form is extremely undesirable and in effect this necessitates the production of special steels with low transition temperatures and high toughness and good abrasion resistance. Many investigators have considered the effects of individual solute elements in steels, and this investigation is an attempt to obtain and correlate results from two widely different approaches, thin foil electron microscopy and notched bar impact testing.

Brittleness may occur in varying degrees and the commonly-used measure of this is a test under carefully specified conditions of an arbitrary design of testpiece. The results from this test are usually expressed as a transition temperature, but this concept is merely a way of obtaining a quantitative comparison between materials and does not appear to have a fundamental definition in the way that the yield stress does. The intention of this study is to examine the effects of five different alloying additions

on the microstructure of the steel and to try to relate this to the Charpy Impact Test results.

The steels were fully hardened and well-tempered. Brittleness is frequently observed after tempering and one experiment is designed to discover whether the ductility of these alloys is affected only by their composition or whether the rate of cooling from the tempering temperature is important.

The alloys were provided by R.A.R.D.E. (see acknowledgements), and the compositions were specified by them also. They were prepared by the fusion of research grade iron and addition of the necessary alloying elements. The melts were chill cast into small ingots and hot-rolled down to bar stock of approximately $\frac{5}{8}$ inch diameter. These bars were used for the machining of Charpy Impact specimens and for metallography.

The following analyses were provided by R.A.R.D.E. from samples taken from the bar stock.

TABLE 1. COMPOSITIONS OF THE SIX ALLOYS

Alloy No.	Percentages by weight							
	C	P	S	Mn	Si	Sn	Ni	N
1	0.29	<0.002	0.007	0.15	0.02	<0.007	<0.01	0.0027
2	0.31			0.15	2.0			
3	0.25	0.004	0.005	0.13	0.01	<0.007	2.94	0.0043
4	0.28	0.026		0.015				
5	0.27	0.010	0.006	0.016	0.03	1.03	0.01	0.0012
6	0.31			0.015				0.014

2.1.1. General metallurgy

Virtually all the techniques of metallurgical investigation have been applied to steels, but not much work has been published concerning 0.3 weight % carbon steels. The stable system, thermodynamically speaking, is the iron-graphite one. However, the only one which need be considered in these steels is the thermodynamically metastable one, namely that between iron and cementite (Fe_3C). Other metastable phases may also be very important, for example epsilon-carbide, martensite and bainite.

2.1.2. Constitution of the six alloys

As received, the alloys consisted of ferrite and pearlite and had been hot rolled. They were heated to 950°C. for three hours and then quenched in a mixture of

ice and brine. The treatment at 950°C., which is well inside the austenite field, allowed sufficient time for the cementite to dissolve and the carbon and other alloying elements to diffuse through the austenite and to approach their equilibrium distributions. Thus, one phase, austenite, was present. On quenching in the ice/brine mixture, the cooling was so rapid that the austenite transformed completely to martensite. The transformation to martensite is usually athermal and commences at a temperature known as M_s and is completed by the time the temperature M_f is reached. The two temperatures differ for steels according to their composition. To avoid any possibility of retained austenite being present in any of the alloys, the samples were then cooled in liquid nitrogen, and maintained at -197°C. for about 15 minutes, after which they were removed and stored at room temperature until they were tempered.

Tempering is a simple process to perform, but the progressive changes which occur in the structure of the steels as tempering proceeds are very complex. In this investigation one tempering temperature was specified, namely 650°C., and the steels were well-tempered so that the only carbide present would be cementite. This avoided the complexities which would have arisen if even more highly metastable carbides were present, for example epsilon carbide

which is important in the early stages of tempering. The structure which resulted from this tempering treatment was therefore ferrite with cementite precipitates, which was confirmed by the use of selected area electron diffraction (Section 2.11).

Some of the alloying elements present in these alloys can form compounds with carbon or with iron, but it is unlikely that separate compounds will be formed owing to the solubilities of the elements in the system (37). However, the possibility of secondary precipitation of compounds must be considered for the longer tempering times.

2.1.3. Optical metallography

Specimen preparation for optical microscopy will not be considered here.

Tempering for one hour and for seventeen hours both resulted in structures typical of tempered martensite. The shapes of the prior martensite crystals could be recognised and macroscopic segregation effects observed (see Ch. 3). The prior austenite grain boundaries could also be observed by their effect on the distribution of the martensite crystals. Hence observation of the microstructure in the quenched and tempered state gave information on the thermal history of the steel over three stages; austenite, martensite and ferrite-cementite.

2.2. Electron microscopy

Electron-optical devices are the most valuable techniques available to physical metallurgy at the present time. Of the various types of instrument, the transmission electron microscope is the most versatile. It may be used for the high-resolution and high-magnification observation of replicas of surfaces and of the internal structures of ultra-thin sections of materials, including metals. In addition to the micrography of such objects it is possible to alter the operating conditions of the instrument to obtain electron diffraction patterns from the specimen. This may be accomplished either as a simple diffraction camera viewing all or a large unspecified area of the specimen, or, with more complex optics, allowing diffraction patterns to be obtained from selected, small areas of the specimen. The latter technique is more useful in metallurgy where it is used to identify the structures present in thin foils and the structures of precipitates and inclusions extracted on replicas. Both replica and thin foil techniques were used in this investigation and the methods are described later.

The principal reason for the use of electrons rather than light in high-resolution microscopes is due to the difference in wavelength. Other important advantages of the use of electrons are their ability to penetrate materials

which are opaque to light, and the possibility of altering their wavelength and penetrating power by altering their acceleration potential. Also, the particular electron-optical system used gives a large depth of field. Thus replicas of fracture surfaces may be observed at high magnifications and will be sharply focussed over the whole field of view.

2.2.1. Resolution

The resolution which may be attained by using electrons is very high.

The theoretical maximum resolution for light microscopy is about 5000 Å. ($\approx \lambda$, the wavelength).

For electron optics, it may be shown that:
$\approx \lambda \sqrt{[150/V]}$ where λ is the wavelength of the incident electron beam in Angstroms and V is the electron accelerating potential in volts.

For V = 100 kV., $\lambda \approx$ 0.04 Å., which is therefore the approximate theoretical limit to resolution at this accelerating potential. In practice, the resolution attained is severely limited by the electron-optical system, i.e. the imperfections in the electro-magnetic and/or electrostatic lenses in the microscope and by the specimen observed. The maximum resolution obtainable using the Siemens Elmiskop I was 15 Å. and that with the J.E.O.L. JEM 7 was about 4 Å., and both require very great care and

very good specimens to approach these figures. The resolution obtained when observing thin foils was less than this, probably approximately 20 Å.

2.2.2. Depth of field

The depth of field in the Siemens Elmiskop was approximately $\frac{1}{3}$ um. which meant that the whole thickness of the specimen was in focus at the same time. This accounts for the value of the electron microscope apart from the observation of specimens at high magnifications and with high resolutions, namely the observation of rough surfaces such as fracture surfaces, or more correctly, the observation of replicas of such surfaces.

In order to be able to use the electron microscope, very stringent specimen requirements have to be satisfied. This necessitates the use of specimen preparation techniques which are described in the following sections.

2.3. Sectioning

The starting material, bar stock of $\frac{5}{8}$-inch diameter was cut on a power saw into 2.5 inch lengths for machining into Izod notched Charpy testpieces and a few six inch lengths for preparation of thin foil blanks.

The six inch billets were heated to 950°C. for one hour and quenched in cold water to harden them sufficiently for cutting-off into thin discs. Three of the hardened billets

could then be positioned side by side on a 2-inch by 6-inch piece of unglazed porcelain tile and embedded in cold-setting mounting plastic. When this block had thoroughly hardened, it was ready for sectioning using an abrasive cut-off wheel.

The cut-off machine which was available consisted of a small electric motor driving a 12-inch diameter abrasive disc which was 1/16 th. inch thick. Water was directed at the sides of the rotating wheel through copper tubes, and drained away through a port in one corner of the tray in which the whole apparatus was mounted. The wheel was enclosed at the sides, back and top by a Perspex box which confined most of the spray and fragments of the wheel, should it shatter. The front of the wheel was partly enclosed by means of a hinged Perspex flap.

An aluminium alloy trolley was used to support the specimen block to be sectioned. This trolley was on rails which allowed it to be pushed towards the wheel, but which located it as far as lateral movement was concerned. The discs cut off were dried and the plastic broken away. The optimum thickness of the discs was between $\frac{1}{4}$ and $\frac{3}{4}$ mm., and this was easily obtained in practice. The grade of wheel finally selected was soft and resulted in a reasonable rate of cutting with no noticeable flowing of the steel and no observable heating either. The discs produced had

reasonably parallel sides which helped the later electro-chemical thinning.

2.4. Heat treatment

Two electric furnaces were constructed to permit heat treatment to be carried out under inert atmospheres. Both were vertical tube furnaces but one was designed to facilitate quenching.

2.4.1. Furnace for austenitising

In order that the temperature in the central region of the furnace should be as uniform as possible over as great a length as possible, the end quarters of the windings were 20% closer spaced than the central half.

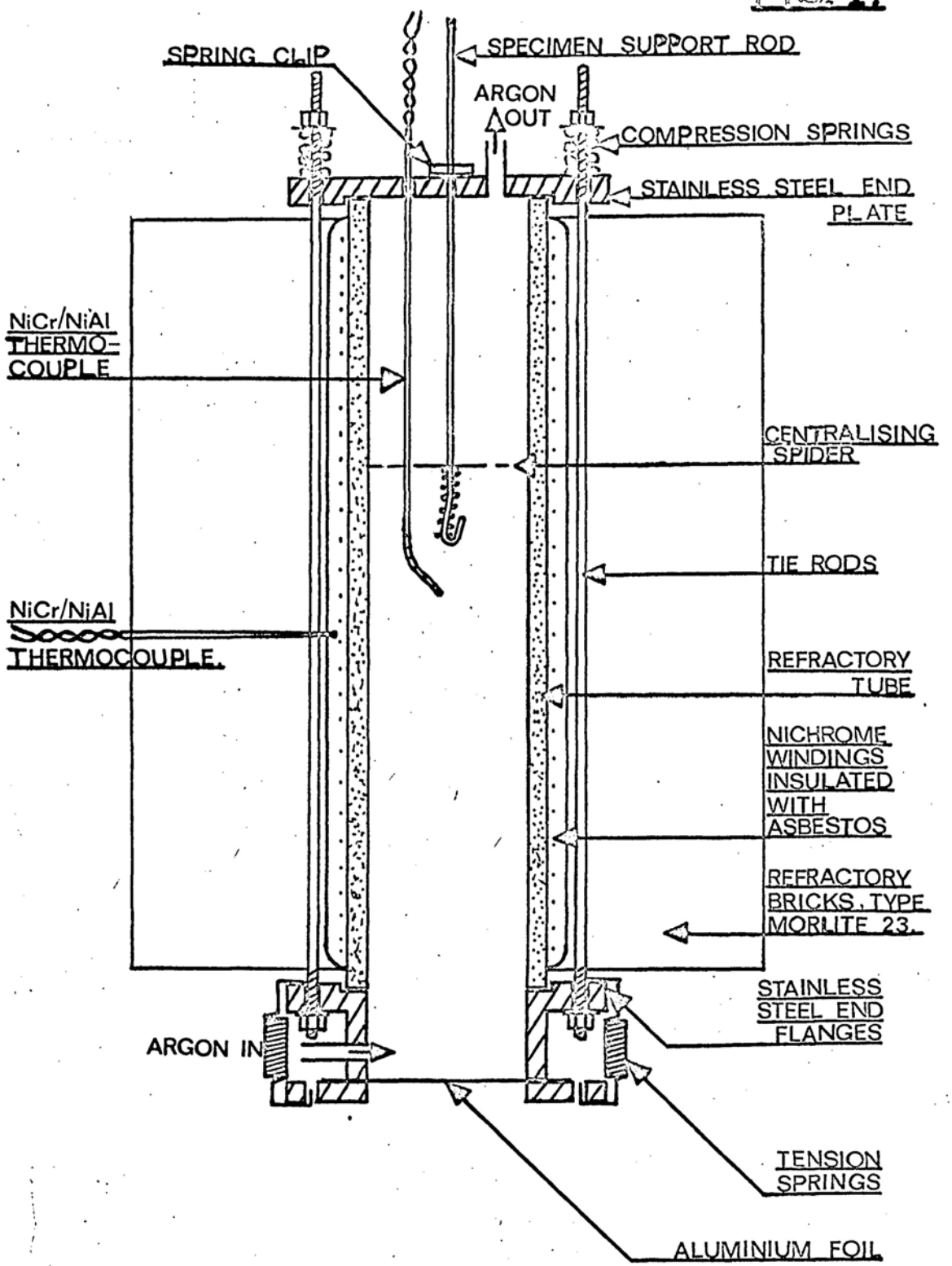
The refractory tube (Anderman type 10A) was 50 cm. long and had an internal diameter of 5 cm. It was double wound with 80/20 Nichrome wire, the two windings having resistances of 57 and 108 ohms. The tube was fitted with stainless steel end-plates which were held in place by means of spring-loaded steel tie-rods. The lower end was closed by a piece of aluminium foil. (See Fig. 1.)

Electrical insulation of the windings was by means of asbestos string and tape.

Thermal insulation was by means of eight hot-face insulating refractory bricks by Morgan Refractories Ltd., type Morlite 23, which were shaped to fit around the furnace

FURNACE FOR AUSTENITISING.

FIG. 1.



THIS DIAGRAM IS NOT TO SCALE.

tube and windings. The whole assembly was held in a box frame of Handy Angle such that the lower end of the furnace tube was ten inches above the supporting surface.

The samples to be heat treated were held in a cage of stainless steel mesh hooked onto a thin rod of stainless steel which could be clamped by means of a large battery clip at the top of the furnace. The quenching liquid was placed directly beneath the furnace.

Two chromel/alumel thermocouples sheathed in silica except for the junction were suspended inside the furnace via small holes in the top end-plate. The small gaps remaining where the silica sheath of the thermocouples passed through the holes were sealed with aluminium foil wrapped around the silica and with Apiezon Q compound which dried at the high temperature to a hard, black mass, which effectively rendered the end-plate gas tight.

The furnace atmosphere of purified argon was admitted through the lower steel flange and a small positive pressure was maintained in the furnace by bubbling the exit gases through water in a test tube.

The operating sequence of the furnace during austenitising was as follows. The billets or discs to be heat treated were loaded into the steel mesh cage, which was then hooked onto the support rod which projected through the base of the furnace for loading. The rod was raised until the specimen

cage was just inside the furnace and the end flange with its disc of aluminium foil could be placed in position to close the furnace. The argon supply was connected and flushed through, after which the flow rate was greatly reduced so as to maintain a very small pressure above atmospheric in the furnace. The rod could then be raised to bring the specimen cage to the centre of the furnace and clamped in that position by means of the battery clip until the time of the heat treatment had expired. The clip was then released and the hot specimens fell through the aluminium disc out of the furnace into the quenching medium, which was a mixture of crushed ice and brine in a bucket underneath the furnace.

Austenitising was carried out at 950°C. for three hours which was considered to be adequate for sufficient homogenisation or segregation as the case may be, in these research purity alloys. The six alloys all received similar austenitising treatment.

2.4.2. Furnace for tempering

Silica was used for the tube of this furnace. The main part of the tube was 5 cm. in diameter and 50 cm. long. This was closed at the top end and a B.10 socket and a small hole included. A gas exit tube was inserted in the side of the tube, near the top. The lower end of the wide tube was fused to the smaller diameter tube associated with a B.34

quartz socket. Into the side of this narrower tube was inserted a short length of quartz tubing to admit the furnace atmosphere, which was purified argon. The tube attached to a B.34 quartz cone was closed off and a wad of glass wool was placed inside it to act as a buffer, should any part of the furnace charge be inadvertently dropped. (See Fig. 2.)

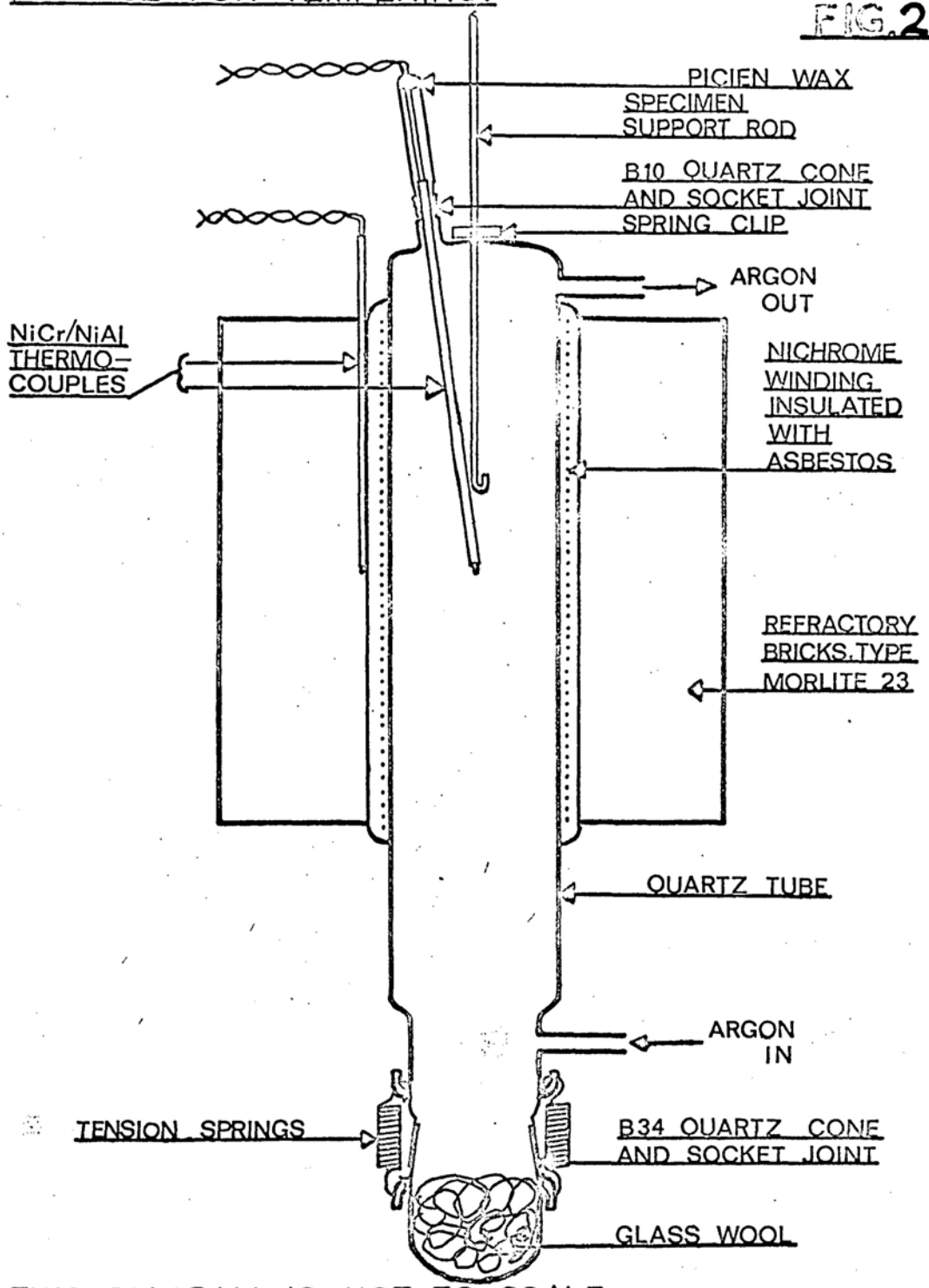
The winding on this furnace was of 80/20 Nichrome wire and was spaced so that the end quarters of the tube had the windings spaced 20% closer than the central half. The resistance of the winding was 55 ohms, and electrical insulation was by means of asbestos string and tape, which were both applied wet and kneaded so that they formed a continuous coat of asbestos fibres over and around the wire. Thermal insulation was by means of eight hot-face insulating refractory bricks which were shaped to fit around the tube and windings.

The B.10 socket at the top of the furnace afforded entry to silica thermocouple sheaths which enclosed chromel/alumel thermocouples to within a few millimetres of their junctions. All cones and sockets were lubricated with silicone grease which is not affected by temperatures up to 200°C., and is only slowly affected at even higher temperatures.

The mode of operation was similar to that of the

FURNACE FOR TEMPERING.

FIG. 2.



THIS DIAGRAM IS NOT TO SCALE.

austenitising furnace, except that at the end of the heat treatment the specimen cage was lowered gently to the bottom of the furnace and resecured until the charge had cooled sufficiently to be handled. Operation of the furnace at temperatures above about 800°C. was not advisable due to slow devitrification of the fused silica.

2.4.3. Temperature control and measurement

Two furnace controllers were purchased which differed in their accuracy and could be used with either furnace. Both could control over the range of 0-1200°C. using chromel/alumel thermocouples and both instruments included cold-junction compensation and thermocouple break protection.

The Ether 3 kW. portable controller, model 15-98, had a proportional band width of less than 10% and used a silicon controlled rectifier output stage to give stepless and switchless control of temperature to ± 5° at 1000°C. This accuracy was sufficient for the austenitising heat treatment at 950°C. The Eurotherm PID-SCR-15 was capable of much greater control accuracy and, when the circuit characteristics had been adjusted in accordance with the makers' instructions, controlled the temperature of the furnace to within 1°C. It was used when tempering at 650°C.

The chromel/alumel thermocouples used by the

temperature controllers were situated inside the furnaces, in close proximity to the specimens being heat treated. A second thermocouple was situated similarly in each furnace and could be used in the event of failure of the other thermocouple or for independent monitoring of the temperature. During the normal course of a heat treatment cycle the temperature was periodically checked by means of a manual potentiometer using the spare thermocouple. Initial tests of the control characteristics of the furnaces were carried out by using the spare thermocouple to generate a millivolt versus time plot on a potentiometric chart recorder.

Base metal thermocouples such as these, which are exposed to the furnace atmosphere and to mechanical damage by collision with the specimens, deteriorate eventually. Consequently it was considered to be desirable to replace them frequently, particularly those used for long periods at 950°C. (Although argon was used during heat treatments, some air was able to enter the furnace during specimen quenching or loading, with consequent oxidation of the thermocouple junctions.)

2.4.4. Furnace atmosphere

To minimise decarburisation of the steels and possible absorption of oxygen or nitrogen it was necessary to use an inert atmosphere. Argon was chosen as the atmosphere for

austenitising and for tempering, and was supplied from cylinders. As a final safeguard a gas purification line was designed and built to reduce the concentration of oxygen, water vapour and organic vapours in the cylinder argon. It was designed to be quickly and easily demountable for replenishment or regeneration of the various agents used. Self-indicating silica gel was used to remove gross water vapour, and molecular sieve (Linde type 5A) to remove traces of any vapours. (See Figs. 3 and 4.)

Copper clippings at approximately 500°C. were used to remove traces of oxygen. They were contained in a small silica tube furnace wound with Nichrome wire and wired across the single phase mains (240 v.) in series with ballast resistors to limit the current to 2 amperes. This was found to give a temperature in the copper of around 500°C., depending on the rate of flow of argon.

A cold trap was available but liquid nitrogen could not be used for its cooling as argon condensed when this was done.

2.5. Grinding

When thin foils were to be prepared, the discs cut off were heat treated prior to grinding. Any scale, therefore, present as a result of heat treatment, was removed together with marks left by the cut-off wheel, in one operation. Wet grinding on silicon carbide papers down to 600 grit was

ARGON PURIFICATION LINE.

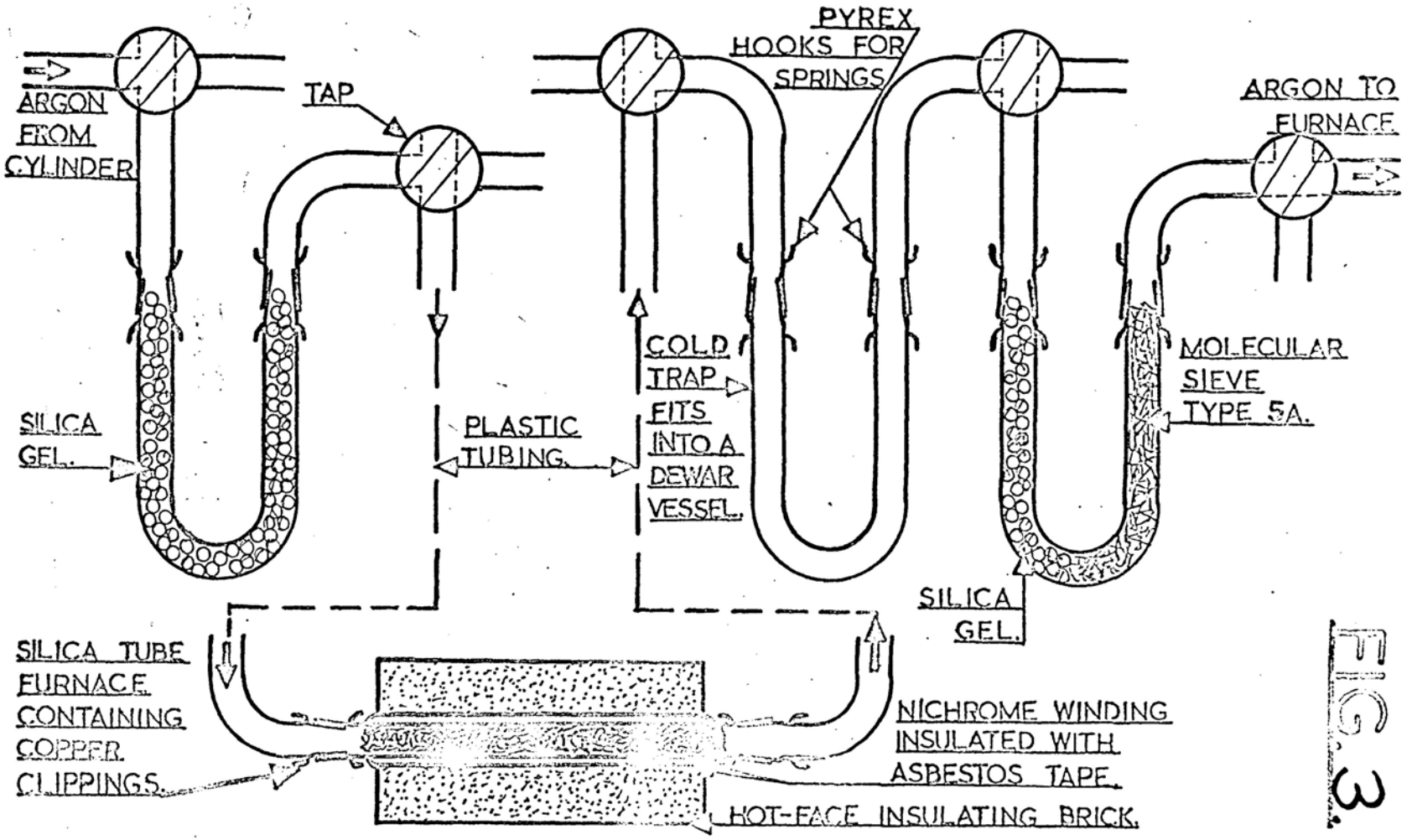


FIG. 3.

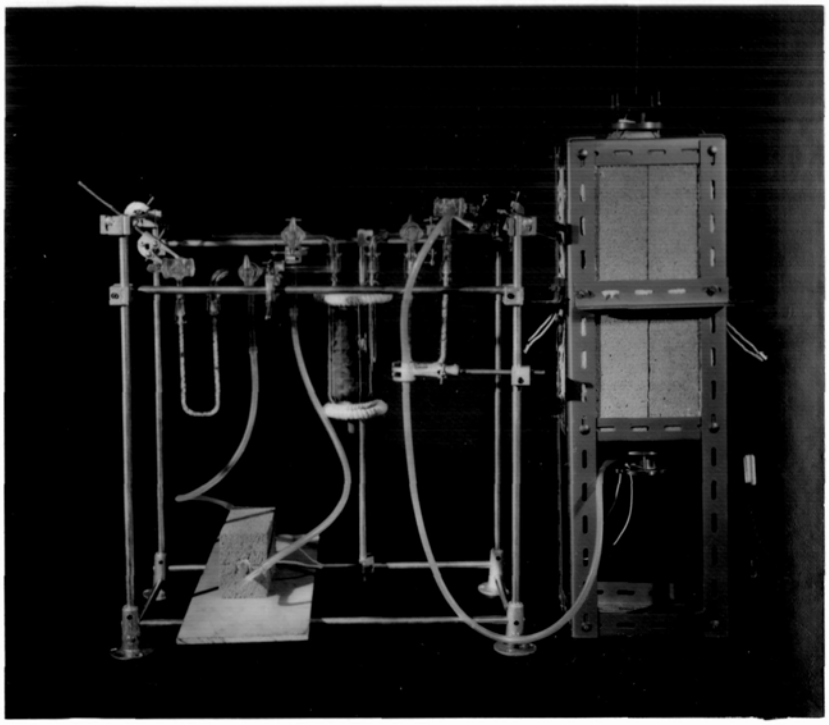


FIGURE 4. The furnace for austenitising and the argon purification line.

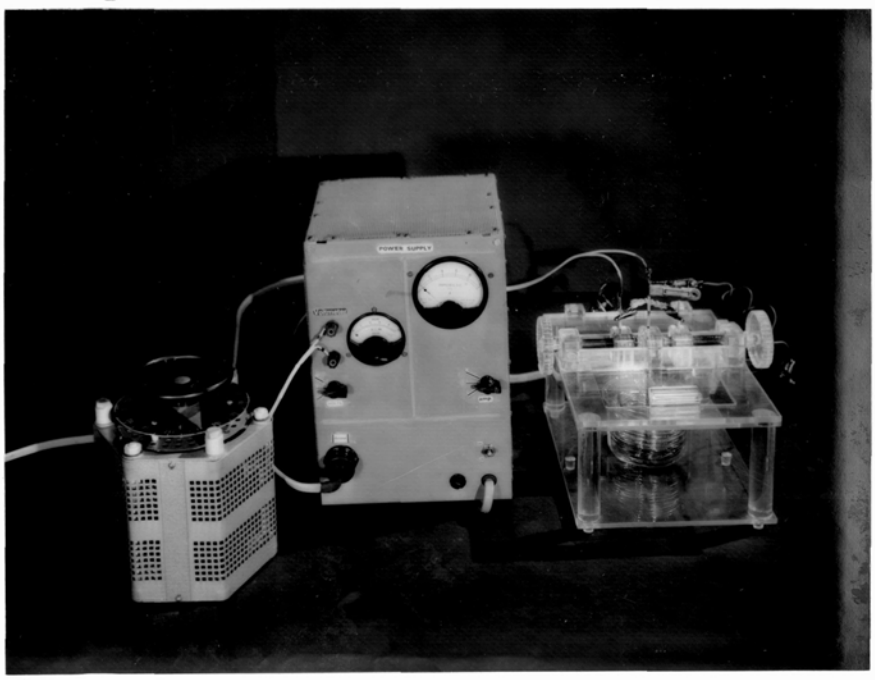


FIGURE 5. The power supply unit and the apparatus for electropolishing.

found to be sufficient and it was possible to grind the discs individually, without mounting, if the wetted silicon carbide papers were placed on a flat surface. By altering the direction of grinding, which was performed very lightly, it was possible to rectify the profiles of some discs that were not parallel-sided after cutting-off.

2.6. Electropolishing

The reduction of thickness of the discs from approximately 0.5 mm. to less than 1000 Angstrom Units for electron transmission was accomplished by two stages of electropolishing. The power supply and the apparatus which contained the electrodes were built and operated as described in the following sections (see Fig. 5).

2.6.1. Power supply unit

In order that a high degree of flexibility could be enjoyed with regard to polishing methods it was necessary to design and fabricate a very flexible power supply unit. As originally envisaged this would have been able to supply up to ten amperes at any voltage up to 100 volts. Owing to difficulty in obtaining a high inductance, heavy current choke, the specification was modified and the resulting unit could supply a maximum of ten amperes at voltages up to 75 volts, decreasing at 7.5 amperes at 100 volts so that the output load did not exceed 750 watts.

The circuit was that of a full-wave rectifier and the output from the rectifier bridge was smoothed by means of capacitors and a choke (see Fig. 6). The output voltage was controlled by altering the input voltage to the rectifier bridge, using a Variac. In order to utilise the Variac to the greatest degree, a 2:1 voltage step-down transformer was used before the rectifiers. The main on/off switch for the unit was placed in the input to the rectifiers to avoid the problem of arcing associated with heavy current switching in the direct current output. This necessitated the inclusion of a leak resistor across the output to allow the capacitor charges to dissipate when the switch was opened with no external load connected. An ammeter was included in the unit and a voltmeter was mounted with the unit but connected to separate terminals. This allowed the voltage to be monitored at any point in the output circuit, thus overcoming the effect of voltage drop in the power-carrying leads and connections.

Observations of the waveform of the output using a cathode ray oscilloscope were performed and revealed a ripple of 75 mV. peak-to-peak at 100 volts output on open circuit. When an external load of 12 ohms (the approximate resistance of the electropolishing cell) was connected across the output, the ripple increased to approximately 2.5% of output voltage peak-to-peak, which is about 1% r.m.s.

POWER SUPPLY UNIT FOR ELECTROPOLISHING.

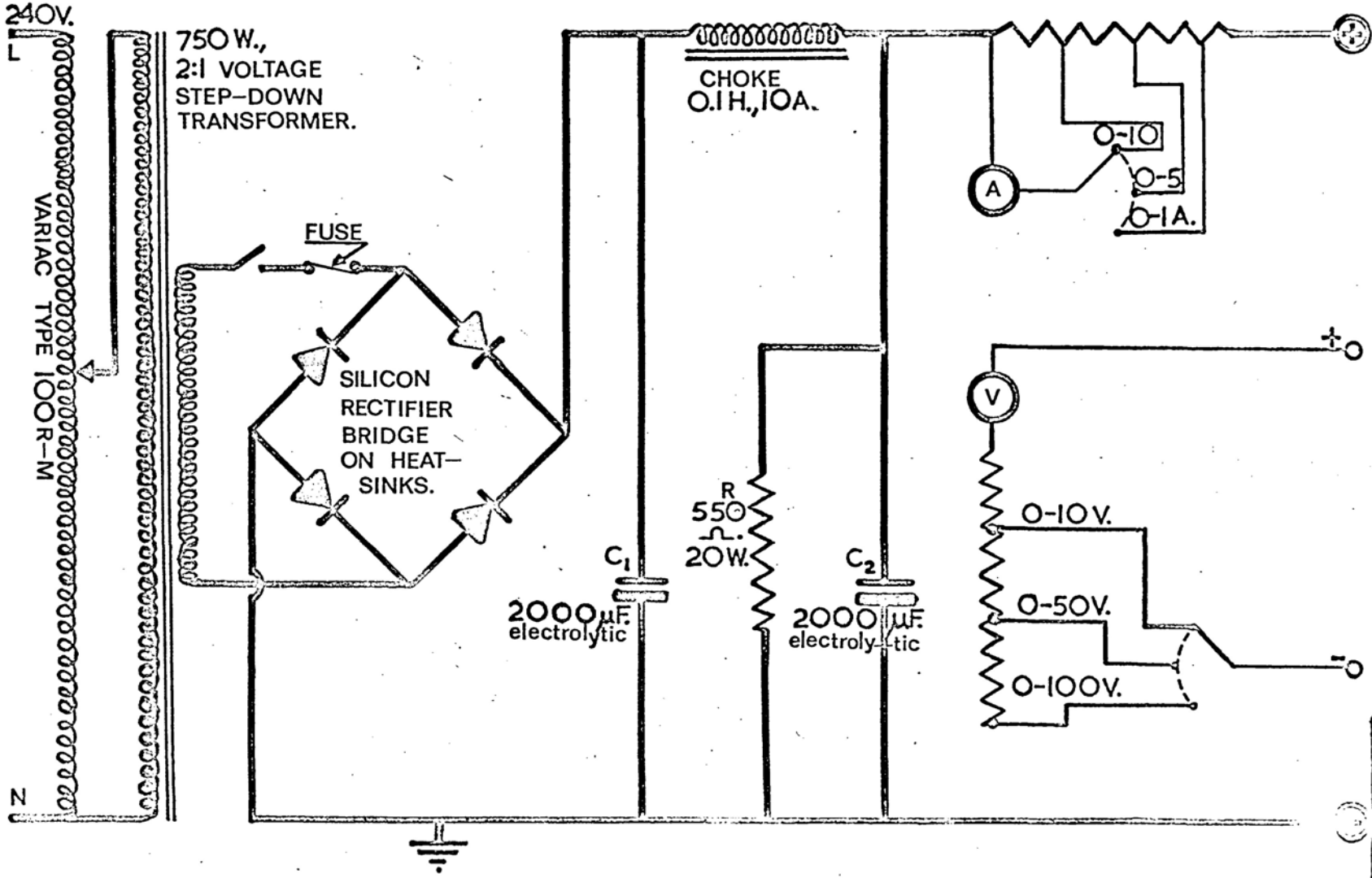


FIG. 6.

This was considered to be adequate for the proposed application, and in practice gave very satisfactory results.

2.6.2. Electropolishing apparatus

The apparatus for electropolishing had to satisfy certain requirements. It was important to have easy and rapid access to the specimen for observation and washing. Precise control of electrolyte stirring was also desirable as different polishing electrode configurations and electrolytes have different requirements for agitation.

The polishing methods that could be used with the apparatus were to be as numerous as possible and the apparatus was to be virtually unaffected by prolonged exposure to any possible electrolyte and to vapours of electrolytes.

2.6.2.(i) Perspex framework

From the above requirements it was decided to use the basic design due to Presland (ref. 38). This was constructed of transparent Perspex sheet and rod (see Fig. 7). All joints were glued and even the prop which held the lid in the vertical position was fabricated from Perspex. The only metal components were three stainless steel grubscrews and two stainless steel hinge pins. This framework gave trouble free service although it was eventually slightly affected by exposure to the extremely

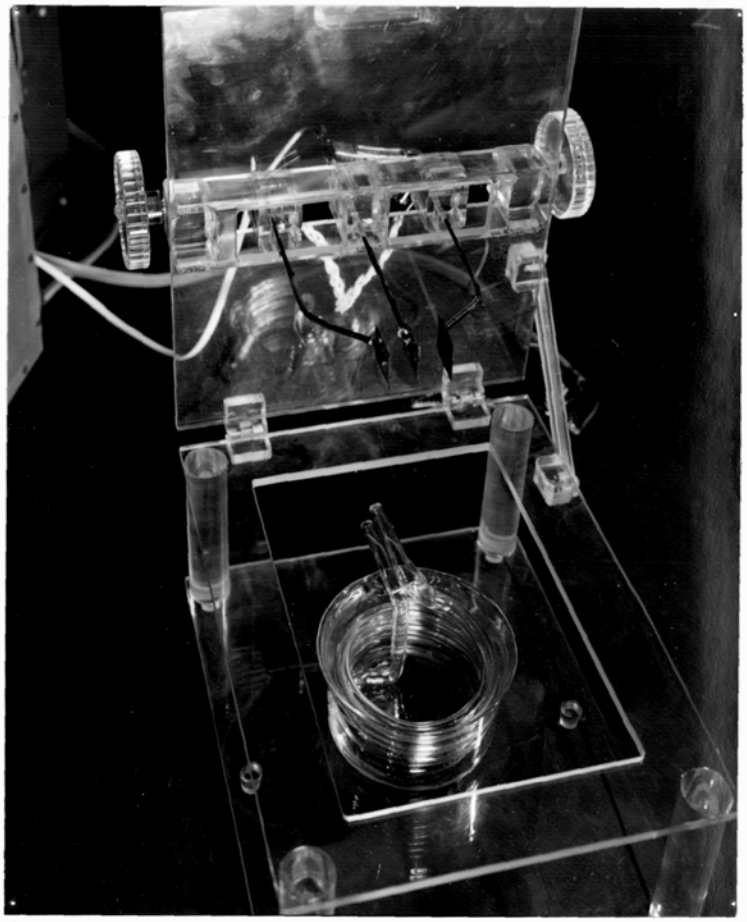


FIGURE 7. The apparatus for electropolishing.

corrosive liquids. The tightness of the main screw in the cathode holder blocks was controlled by applying Lacomit to its threads. This technique enabled all noticeable slackness in the combination to be removed. The entire framework was placed on a magnetic stirrer unit of variable speed.

The electrolyte was contained in a 460 ml. squat Pyrex beaker; inside this a helical coil of Pyrex tube was fitted through which cold tap water was passed to cool the electrolyte. 250 to 300 ml. of electrolyte was required in this arrangement to permit the total immersion of the one-inch square anode with space below it for the stirrer follower.

2.6.2.(ii) Electrode design

With the apparatus described above, either one or two cathodes may be used and these may be of any form desired. The only constraints imposed by the apparatus were the distance from base-board to lid and the requirement that the supporting rod for the cathodes should be of less than $\frac{1}{8}$ th. inch diameter. Similar design limitations applied to the anode, or specimen holder.

In order to simplify the electric field distribution in the electrolyte, the electrode support rods were masked to their ends with Lacomit and P.T.F.E. tubing. Three basic designs of cathode were constructed and tested.

It is important to choose the cathode design in combination with anode design and electrolyte. The choice was made by using a potentiometric X-Y,T chart recorder to plot the current versus voltage characteristics of each combindation of cathode and electrolyte. The three types of cathode tested were :

(i) pointed Bollman-type electrodes in 18/8 stainless steel,

(ii) square sheet electrodes in 18/8 stainless steel (see Fig. 8),

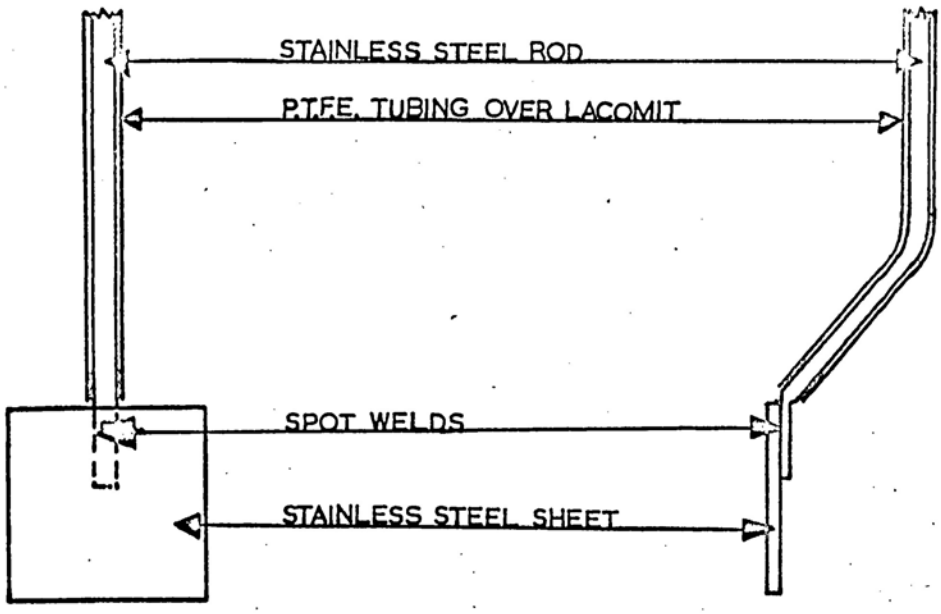
and (iii) small cylindrical billets of 0.3% carbon steel screwed to the ends of the support rods, which were bent so as to present the ends of the cylinders towards the anode.

One design of anode is shown in Fig. 8. The specimen disc was clamped between the two stainless steel sheets and, with care, good electrical contact was obtained in this way. An alternative design of anode which permitted easier removal of the specimen was sometimes used. This comprised a crocodile clip which was attached to the end of the stainless steel support rod. This spring clip was then used to clamp the two sides of the stainless steel disc-holder together, thus replacing the function of the Nichrome wire ring in the diagram, and allowing the specimen disc with its holder to be removed

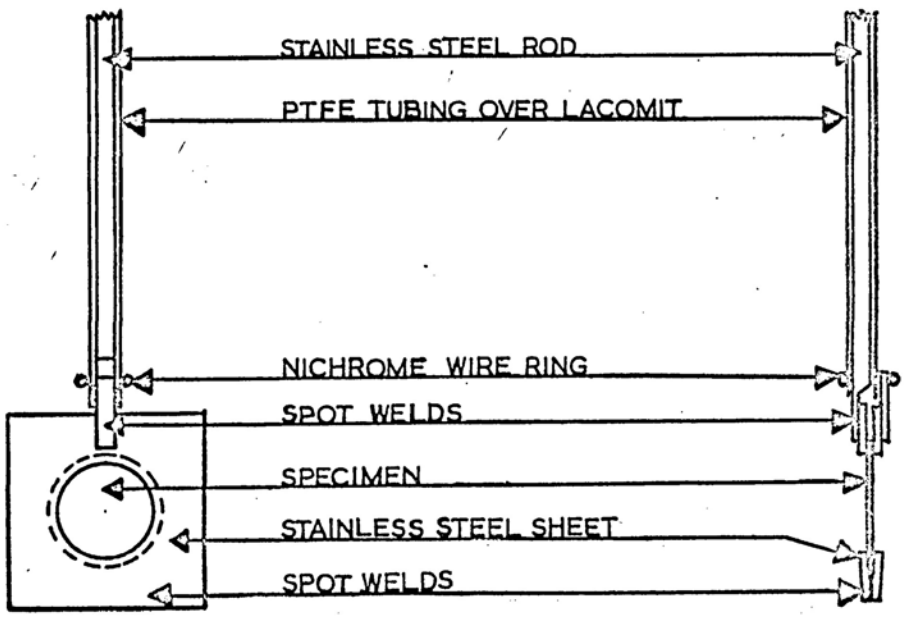
FIG. 8.

ELECTRODES FOR ELECTROPOLISHING APPARATUS.

CATHODES.



ANODES.



SCALE 1:1, i.e. actual size.

from the apparatus without disturbing the specimen support rod and its electrical connections.

2.6.3. Optimum polishing conditions

In all cases when optimum conditions were to be determined the cathodes were equidistant from the anode and the applied voltage was increased very slowly from zero using the Variac. The cell voltage was directly applied to the x-axis of the chart recorder and the potential across a very low resistance in the cathode current lead was applied to the y-axis as being proportional to the cell current. This technique enabled a rapid, although approximate, evaluation of polishing conditions to be made. Combinations of electrode design and electrolyte were chosen which showed a well-defined plateau in their current-voltage characteristics. The optimum polishing voltage was then taken to be close to the lower end of the plateau, and in all cases was found to result in very satisfactory polishing.

The profile of anode which was produced by particular cathodes was dependent on the electrode separation and this could be altered in practice to give the profile desired at any stage of thinning. The further apart the electrodes were placed, the more severe was the edge attack where the specimen disc met the contact ring. As the cathodes were brought nearer to the specimen, the rate of attack at the

centre of the disc progressively increased, so by experiment, the optimum separation for uniform thinning could be ascertained. For the apparatus used the optimum anode to cathode distance was found to be approximately 3 mm. The optimum voltages are given in Sections 2.6.4 and 2.6.5.

2.6.4. Primary electropolishing

Discs were clamped in the anode and electropolished in 5% perchloric/acetic acid at 14 volts, using the square sheet cathodes or the cylindrical billet ones at a distance of approximately 3 mm. The electrolyte was prepared by adding perchloric acid very slowly to acetic acid while stirring and cooling. Analar grade chemicals were used and great care was taken to ensure that the temperature of the mixture did not rise above 20°C. as this electrolyte tends to be explosive under some conditions.

During electropolishing the electrolyte was stirred at the minimum rate of the magnetic stirrer with a 1 cm. follower in the electropolishing bath. Cold water was passed through the glass cooling coil at a rate of about 100 ml. per minute. Under these conditions the current was approximately 2 amperes, although it was somewhat higher for a few seconds when polishing was commenced. If the current was much lower than this, etching occurred, but a significant increase in the voltage resulted in a lowering of polishing quality. The best polishing was

obtained when etching of the stainless steel specimen holder occurred towards its outside edge.

It was essential to maintain good electrical contact between the specimen disc and the anode. Since this contact was by pressure of the two discs on the rim of the disc it was desirable occasionally to rub the disc a few times on 600 grit silicon carbide paper until the whole periphery was restored to a bright condition. If electrical contact with the specimen was poor, etching of the specimen occurred.

After polishing for two minutes or so, the electrodes were raised from the electrolyte with the power still switched on. The specimen was then washed vigorously with industrial methylated spirit from a wash bottle.

The cylindrical cathodes gave more uniform polishing than the square sheet ones. This may have been due to geometrical factors, or to the fact that they were made of a 0.3% carbon steel and not 18/8 stainless steel as were the sheet electrodes. Thus, as polishing commenced, corrosion and pitting of the cylindrical cathodes occurred and this was naturally more severe where the current density was greatest. These conversion products probably increased the surface resistance and so reduced the current density at that point. It may be that in this way the current density on the cathodes tended to become uniform, and that

this was reflected to a certain degree in the current density on the anode, and hence in the rate of metal removal from the specimen disc.

The cathodes were periodically cleaned with hand-held silicon carbide papers to avoid removing the profile of the cylinders which might be produced by preferential corrosion. If this was not done, the anode was etched owing to the redistribution of potential across the anode caused by the poor electrical contact with the specimen disc. Polishing could be continued using this method until the specimen disc was approximately 0.003 inch thick (approximately 0.0075 cm.), at which stage more control of profile than could be obtained with this electrolyte was desirable if good foils were to be produced from the disc.

2.6.5. Secondary electropolishing

The final thinning of the specimen disc had to be performed very carefully, so as to control the profile of the disc and the quality of the surface finish. The electrolyte used in this stage was a chromium trioxide/acetic acid/water electrolyte, and two effective ways of preparing this were used.

Method 1. 100 g. chromium trioxide,
14 ml. water,
265 ml. glacial acetic acid.

The chromium trioxide was placed in a one litre beaker

and the water was added. A 3 cm. follower for the magnetic stirrer was added and the mixture was stirred rapidly for at least 30 minutes. The acetic acid was added slowly and the mixture stirred vigorously until all, or almost all, of the chromium trioxide had dissolved. This was best done by allowing the process to continue overnight. The results obtained with this electrolyte were greatly improved by reducing the water content to 11 or 12 ml. However this rendered the chromium trioxide even less soluble than before.

Method 2. 100 g. chromium trioxide,
10 ml. water,
250 ml. glacial acetic acid.

This method enabled the proportion of chromium trioxide to be increased, and that of water to be decreased. This was accomplished by preparing the electrolyte in the same way as in Method 1, and then by heating it for one hour at 60°C. while stirring constantly. There is a potential fire hazard in this procedure, however, so Method 1 was used wherever possible. Method 2 was particularly helpful when thinning the silicon alloy.

The cylindrical cathodes were used for completing the polishing of all six alloys, the polishing voltage being 15-30 volts. Increasing the voltage led to an

increase in current with consequent increase in metal removal rate, but also a decrease in the quality of the surface. Using a voltage of 10-15 volts gave the possibility of etching and 15-20 volts resulted in very slow polishing, but with an excellent finish. Consequently the secondary electropolishing was commenced at a voltage of about 25 volts which resulted in a cell current of around 1.5-2 amperes. The specimen was removed and washed frequently, particularly towards the end of the thinning process. Industrial methylated spirit was used for washing, although an occasional rinse in glacial acetic acid was beneficial if a bloom was noticed on the surface of the disc, which indicated the presence of an oxide film.

When the specimen disc was locally very thin, the polishing voltage was reduced to around 15 volts until initial perforation occurred. It was sometimes possible to cut a thin region off at this stage, but it was usually better to stop-off the edge of the hole with Lacomit and to continue thinning until a second perforation was produced. By experimenting with stopping-off and removing this lacquer again it was possible to prepare a few thin foils of reasonable quality from each disc thinned.

2.6.6. Mounting

Thin foils were cut from the discs by using a new blade in a scalpel and pressing this blade onto the steel

on any fairly soft but non-resilient surface such as plastic or brass. In this manner small fragments of steel were produced without bending and were handled with forceps of austenitic stainless steel (non-magnetic) or with wooden cocktail sticks. Each prospective foil was sandwiched in a copper double grid in the usual manner, ensuring that the grid was locked shut by using the small tab on the grid. A loaded grid was then mounted in the Valdre tilting holder for the goniometer stage in the Siemens Elmiskop I.

Spare foils and the remains of the specimen disc were placed in a dessicator under vacuum and the chosen foil observed in the electron microscope with as little delay as possible to minimise deterioration of the thin foil by corrosion in the atmosphere.

2.7. Replica techniques

The only type of replica used was a two stage plastic/carbon one which was easy to prepare and was capable of adequate resolution (about 200 Å.).

The fracture surface to be replicated was washed thoroughly with chloroform or acetone and allowed to dry. A small square of cellulose triacetate film was moistened with acetone and pressed firmly against the fracture surface and when any air bubbles had been expelled, was left to dry thoroughly for a few hours at least. When thoroughly dry, the film was carefully stripped from

the steel.

2.7.1. Shadowing

The cellulose triacetate film was placed in a Balzers coating unit (Mikro BA 3) and a few Angstroms thickness of 40% palladium/gold alloy was deposited at an angle of 45°, thus casting shadows on the plastic surface. Deposition was accomplished by wrapping a short length of 40% palladium/gold wire of 0.010 inch diameter around a V-shaped filament of tungsten wire which was then electrically heated in a vacuum of better than 1×10^{-4} torr. to evaporate the shadowing material.

2.7.2. Carbon coating

After shadowing, carbon was deposited on to the plastic impression by producing an arc between two carbon rods under a vacuum of 10^{-4} torr. or better. A thickness of about 250 Angstroms of carbon was deposited; this was estimated by observing the colours produced by the increasing thickness of carbon on a gold film evaporated onto an aluminium substrate, placed beside the plastic replica. As soon as the colour turned brilliant deep blue, about 240 Angstrom units thickness of carbon had been deposited, (39), which was the optimum for such a replica.

2.7.3. Mounting of replicas

The plastic with its coating of carbon was removed from the vacuum unit and a triangular fragment of the composite approximately 2 mm. on a side was cut and immersed in acetone with the carbon uppermost until the latter floated free from the plastic. After thorough washing in acetone the triangular replica was picked up on a copper grid. If the replica rolled up in acetone it was transferred to a 2% dioxane/water solution which, because of its greater surface tension and the fact that it is miscible with acetone, often flattened the replica so that it could be picked up on a grid. The dioxane content of the solution served to reduce the surface tension below that of pure water, which flattened the carbon film so violently that it broke into unusably small fragments.

2.8. The electron microscope

A Siemens Elmiskop I was used for all the thin foil transmission work. This instrument was fitted with a decontaminator cooled with liquid nitrogen to reduce the rate of contamination of the specimen, and a goniometer stage to allow the orientation of the thin foil to be altered in the microscope. These two accessories are almost essential for the successful and detailed examination of thin polycrystalline metal foils. The goniometer stage was of the Valdre type. Two tilting

motions were orthogonally arranged and these were independent of the normal translation motions of the stage. The Valdre specimen holder used with this stage was capable of a tilt of $\pm$ 20°.

The Siemens microscope was a five lens high-resolution type with sufficient resolution for thin foil studies, as discussed earlier. A J.E.O.L. JEM 7 was used for the replica studies.

2.8.1. Image contrast

Contrast in an electron image is a spatial variation of electron current density across the image. When electrons are incident on the specimen some are transmitted without being deflected whilst others are scattered through various angles. The electrons comprising these transmitted beams are focussed by the objective lens at its back focal plane, and each point in the back focal plane of the objective lens can be shown to correspond to a particular direction of scattering from the specimen. A small hole in a disc of molybdenum, known as the objective aperture, is used to select one of these focussed beams, usually the zero-order (undiffracted) beam. Therefore only electrons transmitted by the specimen in a particular direction are permitted to contribute to the image; all other beams are intercepted by the aperture and so are absent from the image. Contrast in the image thus depends on the direction

of diffraction by the specimen, and areas diffracting strongly away from the aperture will appear dark whereas areas diffracting a beam through the aperture will appear bright.

In a polycrystalline foil, the grains and subgrains have, by definition, different orientations, and so diffract the electron beam differently. The microscopes objective aperture is normally positioned to allow the zero order beam only to pass. Consequently, the image will exhibit intensity differences from grain to grain of the foil.

Very thin foils, or regions close to the edge of thicker foils may be buckled, in which case local regions may satisfy Bragg diffraction conditions. These regions are known as extinction contours, and every point on such a contour has the same orientation, and so is diffracting into the same Bragg reflection.

Dislocations or other imperfections in the crystal may give rise to local Bragg scattering, or local absence of scattering, thus altering the intensity of the zero order beam locally. However, there are complications to this and the precise way in which crystal defects affect the transmission of the electron beam depends on the nature of the defect and its orientation with respect to the beam.

In amorphous specimens or those with very small

crystallites which are randomly oriented, contrast is due to slightly different effects. Atomic number contrast arises because electrons interact with atoms in a manner which depends on the atomic number of the species involved; the higher the atomic number, the greater is the scattering effect, hence the use of heavy metals for shadowing on replicas.

Thickness contrast arises because the intensity of the transmitted zero-order beam is dependent on the thickness of the film in the direction of the beam.

For parallel-sided amorphous films, such as carbon replicas a special kind of thickness contrast is observed, namely gradient contrast whereby the gradient of the film at a particular point affects the thickness of material in the direction of the transmitted beam, and hence the contrast.

2.9. Electron-optical theories of transmission image contrast

The two principal theories which enable useful information to be gained concerning the way in which electrons are transmitted through crystals are the kinematical and the dynamical theories. The former is easily used to obtain much useful qualitative information, although the theory has a few very serious shortcomings, which may be overcome by resorting to the more sophisticated

dynamical theory. In particular, the latter theory becomes necessary when the crystal through which the electron beam is passed is greater than a certain thickness.

Thus, the kinematical theory predicts that the relative intensity of the diffracted beam, $\frac{I}{Io} = \left|\phi_g\right|^2 = \frac{\pi^2}{\xi_g^2} \cdot \frac{\sin^2(\pi ts)}{\pi^2 s^2}$, which simplifies to $(\pi t/\xi_g)^2$ at the Bragg angle, where t is the crystal thickness and s is the deviation of the diffraction vector g from the Ewald sphere. Io is the intensity of the incident beam and I is that of the transmitted beam. ξ_g is the extinction distance and refers to a particular reflection and crystal.

Thus when $t > \xi_g/\pi$, which may occur for crystal thicknesses of anything from 200 to 1500 Å. depending on the structure of the crystal and the reflection operating;

$$\left|\phi_g\right|^2 > 1.$$

This means that the intensity of the diffracted beam would exceed that of the incident beam, which obviously cannot occur. However, the kinematical theory using an elemental column approximation does allow the diffraction behaviour of crystalline foils to be semi-quantitatively explained.

2.10. Image interpretation for thin foils

Several phenomena are likely to be observed in foils of steel, namely grain boundaries, sub-grain boundaries, precipitated phases and dislocations. The contrast effects resulting from these phenomena may be explained by use of the kinematical theory of electron transmission. The theory predicts that the contrast of a dislocation will be governed by the magnitude of a parameter, $n = \underline{g}.\underline{b}$, where $\underline{g}$ is the reciprocal lattice vector of the reflection operating and $\underline{b}$ is the Burgers vector of the dislocation (in real space). In particular, if $\underline{g}.\underline{b}. = 0$, the screw dislocation will be invisible. This is found to be the case for screw dislocations but dislocations having an edge component are found to have a residual contrast even when $\underline{g}.\underline{b}. = 0$. This is also explained by the kinematical theory.

In view of the resultant variability of dislocation contrast from grain to grain, measurement of dislocation densities from transmission electron micrographs is a tedious procedure with dubious results. Not only is there uncertainty in the number of dislocations present, but also in the volume they occupy since the foil thickness is not known. For these reasons, quantitative estimates of dislocation density were not attempted.

The low-angle boundaries separating subgrains may often be distinguished from high-angle boundaries since the

dislocation network or wall comprising the former is sometimes resolved. Selected area electron diffraction in combination with the tilting specimen stage can also give an indication of the relative orientation of grains. Owing to their different crystal structures which affect the intensities of transmitted electrons, in addition to their shapes and sizes which are characteristic and quite different from those of the ferrite subgrains, carbides in the image are visually identifiable. The appearance of the carbides is only circumstantial evidence of their identity, however, and if proof is required, selected area electron diffraction must be used.

The resolution obtained during the observation of thin metal foils in the electron microscope is limited by the thickness of the specimen and also by the presence of contamination on its surfaces. This contamination consists of any film of oxides remaining from electrothinning or from tarnishing in the atmosphere before insertion in the microscope, in addition to the film of polymerised hydrocarbon formed on the metal surface as a result of irradiation in the electron beam. The oxide film may be minimised by careful attention to the final electropolishing conditions and washing procedure. The contamination rate inside the electron microscope was reduced considerably by the use of the decontaminator,

which consisted of liquid nitrogen-cooled surfaces close to the specimen in the column. With these precautions the foils could be observed for lengthy periods before the image quality deteriorated seriously.

2.11. Selected area electron diffraction

Thie technique involves the insertion of an aperture in the intermediate lens (or projector I), and the adjustment of the objective and intermediate lens currents until the specimen and the intermediate aperture are simultaneously focussed on the screen. At this stage, a particular area of the specimen may be located; if the intermediate lens current is then further reduced to image the back focal plane of the objective lens, the diffraction pattern corresponding to the area selected appears on the screen. This diffraction pattern gives crystallographic information on the material in the area selected by the intermediate aperture.

Ferrite has a body-centred cubic structure, and cementite is orthorhombic, so that the two can be easily distinguished.

An electron diffraction pattern is essentially a plane section through the reciprocal lattice of the diffracting material (ref. 38). Each diffraction spot represents a set of diffracting planes in the crystal, e.g. $(h_1k_1l_1)$. The distance between each spot and the central spot (Rhkl)

is proportional to the reciprocal of the corresponding lattice vectors, e.g. $R(h_1k_1l_1) = \frac{K}{d_{h_1k_1l_1}}$, where K is the camera constant. The angles such as $(h_1k_1l_1)(000)(h_2k_2l_2)$ are the angles between planes $(h_1k_1l_1)$ and planes $(h_2k_2l_2)$. Both interplanar spacings and angles may be found in standard tables or may be computed from equations which require the knowledge of h_1,k_1,l_1,h_2,k_2,l_2, together with the type of crystal concerned, e.g. cubic, orthorhombic, etc.

These rules are applied to the diffraction pattern and, when the spots are consistently indexed, the orientation and crystal structure of the material within the area selected has been determined. This method is not very accurate with regard to interplanar spacings, but in simple steels, the phases have very different structures, and interplanar spacings are not necessary for elucidation of the nature of a particular phase.

2.12. Image interpretation for replicas

The replicas used in this investigation were of carbon, of an average thickness of approximately 240 Å, shadowed with a small quantity of 40% palladium/gold alloy which was unevenly distributed owing to the relief of the replica and the acute angle of deposition. Both the carbon and the heavy metal shadowing material had a small

crystallite size, and, as far as the transmission of electrons was concerned, could be thought of as amorphous. Thus the replica material itself appeared to be featureless, but was shaped to follow the contours of the fracture surface. Consequently, the amount of heavy metal shadowing material present on each facet of this surface varied, and so likewise did the ease of transmission of the electron beam. (See section 2.8.1.)

The image may be interpreted in the same way as would an optical micrograph of the surface with the reminder that the shadowing material on the surface darkens the image at that point. The magnification which may be used with most effect is quite low, about x 5000, which avoids the resolution of the particles of the shadowing material.

2.13. Notched bar impact testing

The notched bar impact test was used to measure the degree of brittleness in the steels. Other testing methods, such as fracture toughness testing, would give much more information but would have taken longer to perform.

2.13.1. Testpiece design

The testpieces for impact testing were standard Izod-notched Charpy testpieces, as it was desirable for the results of the impact testing to be comparable with

other investigations performed at R.A.R.D.E., Fort Halstead. The standard radius at the notch root was used as it was not considered that a decrease in notch root radius in these reasonably ductile steels would justify the fatigue cracking procedure for initiating a crack at the root of the notch. It is also possible that fatigue stressing in steels in the hardened and tempered condition could modify the dislocation structure in relation to the carbides for a considerable distance in front of the actual fatigue crack.

2.13.2. Testing machine and procedure

The testpieces were broken over a wide range of temperatures (see Fig. 9) at Fort Halstead, using a pendulum hammer which conformed to the relevant British Standard with regard to rigidity of the striker and bearings, etc. The work was carried out by experienced operators in order to eliminate operator differences in the results when compared with other data obtained at Fort Halstead.

The means of attaining the temperatures used all comprised baths of liquids which were placed within a few inches of the anvil; trays supported the testpieces near to the centres of the baths. They were soaked in the baths at the required temperatures for 15 minutes, after which time they were extracted from the liquids, using tongs also at the temperature of the bath, and placed on

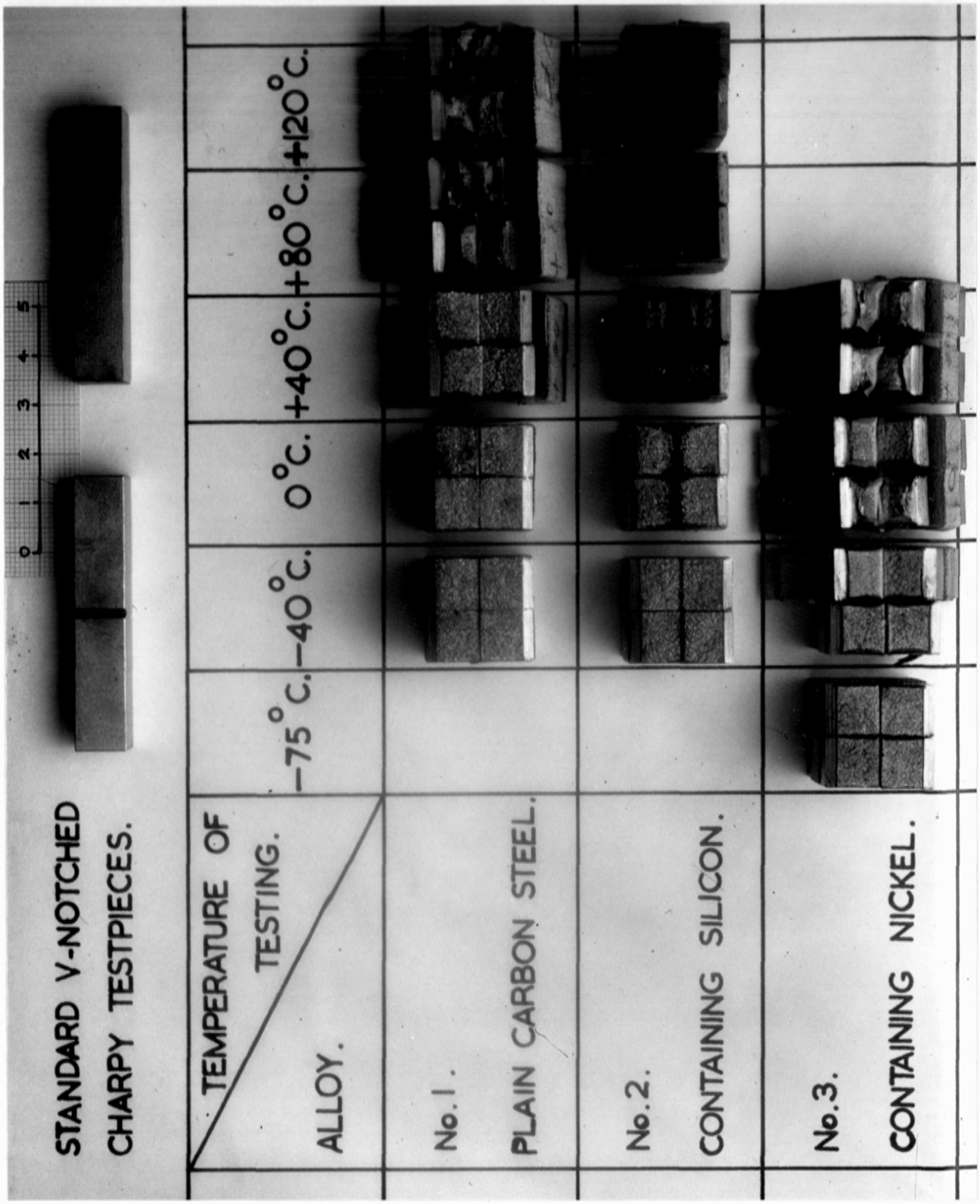


FIGURE 9. Charpy impact specimens after testing.

the anvil. An end gauge was used to enable the notch to be exactly central between the supports. The trigger release was operated and the pendulum striker fell to collide with the testpiece less than five seconds after it had been taken from the bath. The striker was secured ready for the next specimen and the energy absorbed during contact with the specimen was recorded from a dial in m.kg.

The temperatures used ranged from -196°C. using liquid nitrogen, to +250°C. using a salt bath, the intervening temperatures being covered by the use of solid carbon dioxide/acetone mixtures (-75°C. to room temperature), and glycerol (room temperature to +150°C.). Two testpieces were broken at each temperature.

2.13.3. Interpretation of results

The results were recorded in m.kg. as indicated on the testing machine, and converted to ft.lb_f. The results from each pair of testpieces were averaged and these averages were plotted versus testing temperature for each alloy and each heat treatment condition tested. The usual manner of expressing results from this test was adopted, namely a graph of energy absorption during fracture versus testpiece temperature, and a ductile/brittle transition temperature determined (see section 3.2.2.) for each alloy in each heat treated condition studied.

Within each pair of testpieces, the two results

occasionally differed quite widely. This was probably due to chance effects on the nucleation of the cracks by the machining marks at the base of the notches. Plotting the average of the values obtained using two specimens at each temperature enabled smooth curves to be constructed.

CHAPTER 3. EXPERIMENTAL RESULTS

3.1 Characterisation of microstructure

3.1.1 Optical microscopy

Figures 10 to 14 inclusive are examples of the appearance of etched sections of some of the alloys. In all cases the grain size was very small and the prior austenite grain boundaries may be observed owing to their effect on the morphology of the martensite. The martensite formations appear somewhat different in each alloy. Some alloys show a very sharp, fine needle morphology of the martensite whereas others, notably the nickel steel (No. 3), reveal a coarser structure which even approaches the appearance of massive martensite in places.

The carbides could not be resolved under the optical microscope in any of the alloys, indicating that they were less than about 1 μm. long. The black marks appearing on some of the photomicrographs are etching artefacts.

3.1.2 Electron microscopy after tempering for 1 hr.

(i) Plain carbon steel, alloy No. 1

The structure revealed in this alloy was found to be generally typical of the other alloys. The difference between alloys were largely differences of scale rather than of type. The ferrite grain and subgrain boundaries were easily visible but not always easy to distinguish from

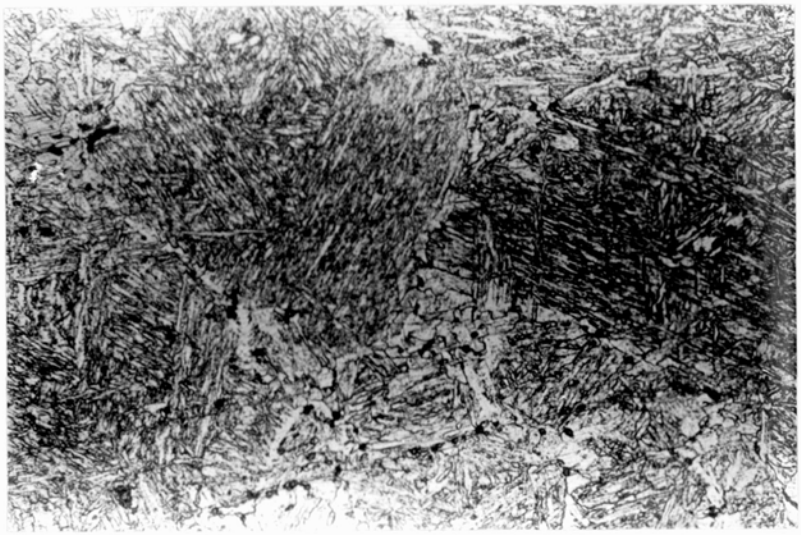


FIGURE 10. Silicon steel tempered for 1 hour. (x 240)



FIGURE 11. Nickel steel tempered for 1 hour. (x 240)

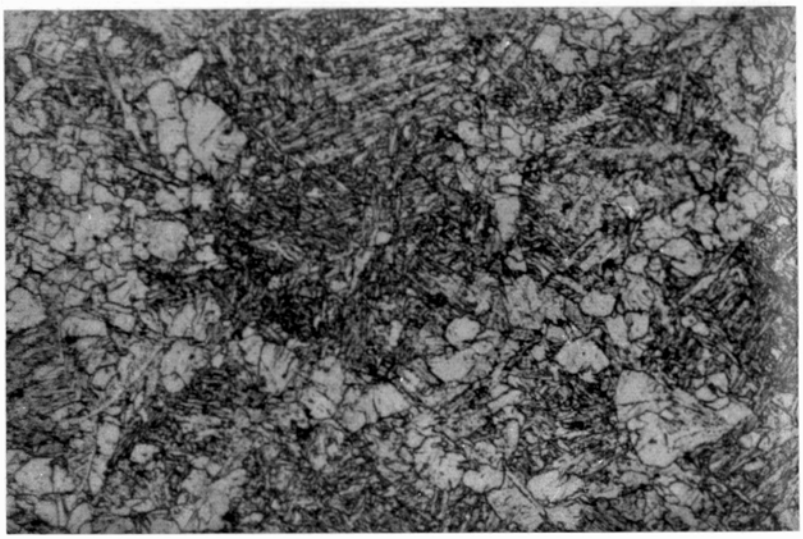


FIGURE 12. Tin steel tempered for 1 hour. (x 240)

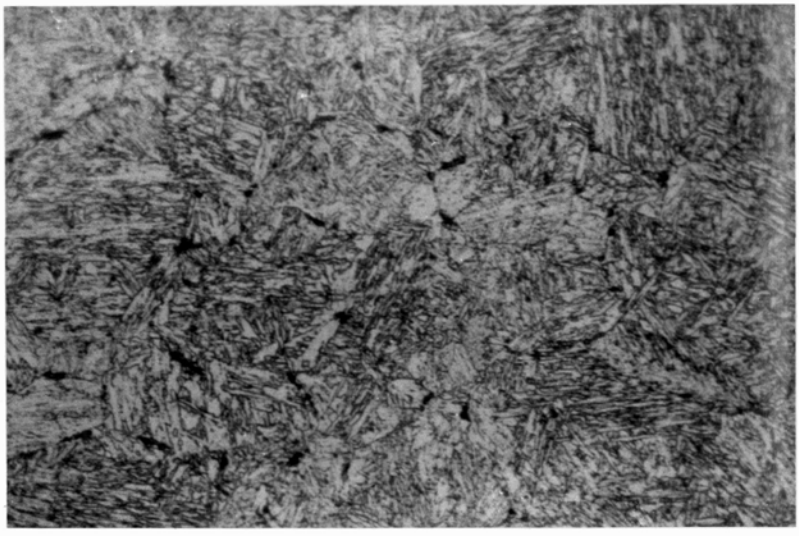


FIGURE 13. Silicon steel tempered for 17 hours. (x 240)

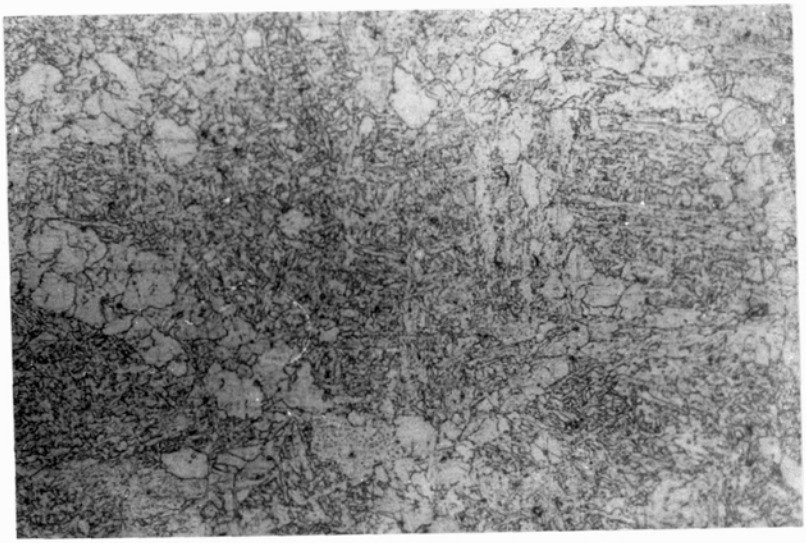


FIGURE 14. Tin steel tempered for 17 hours. (x 240)

one another (see Figs. 15-17). The carbides were located on both types of boundaries and were readily identified by virtue of their rounded shapes as well as by differential electron diffraction (see Section 2.11).

Dislocations occurred inside grains and subgrains as well as in the boundaries. As the subgrain formation in this alloy was well advanced, the number of dislocations not forming boundaries was quite low ($< 10^6 cm^{-2}$).

The carbides were elongated with aspect ratios between 3:1 and 1:1. In this alloy after tempering for one hour at 650°C, the average value of the major axis of the carbides was 0.29 μm. This dimension was obtained by measuring the images on photographic plates or paper using a steel rule of reasonable accuracy. As many carbides as possible were measured, but it must be realised that the number in practice was not as great as it should be owing to the sparse distribution of the carbides. However in all cases, more than thirty carbides were considered, and these were quite similar in size.

The mean diameter, D, of a subgrain in this alloy after tempering for one hour was 0.54 μm; subgrains tended to be rectangular in section owing to the morphology of the prior martensite crystals, which were apparently thin laths or needles, and the boundaries between these crystals were retained through the tempering process. The high disloca-

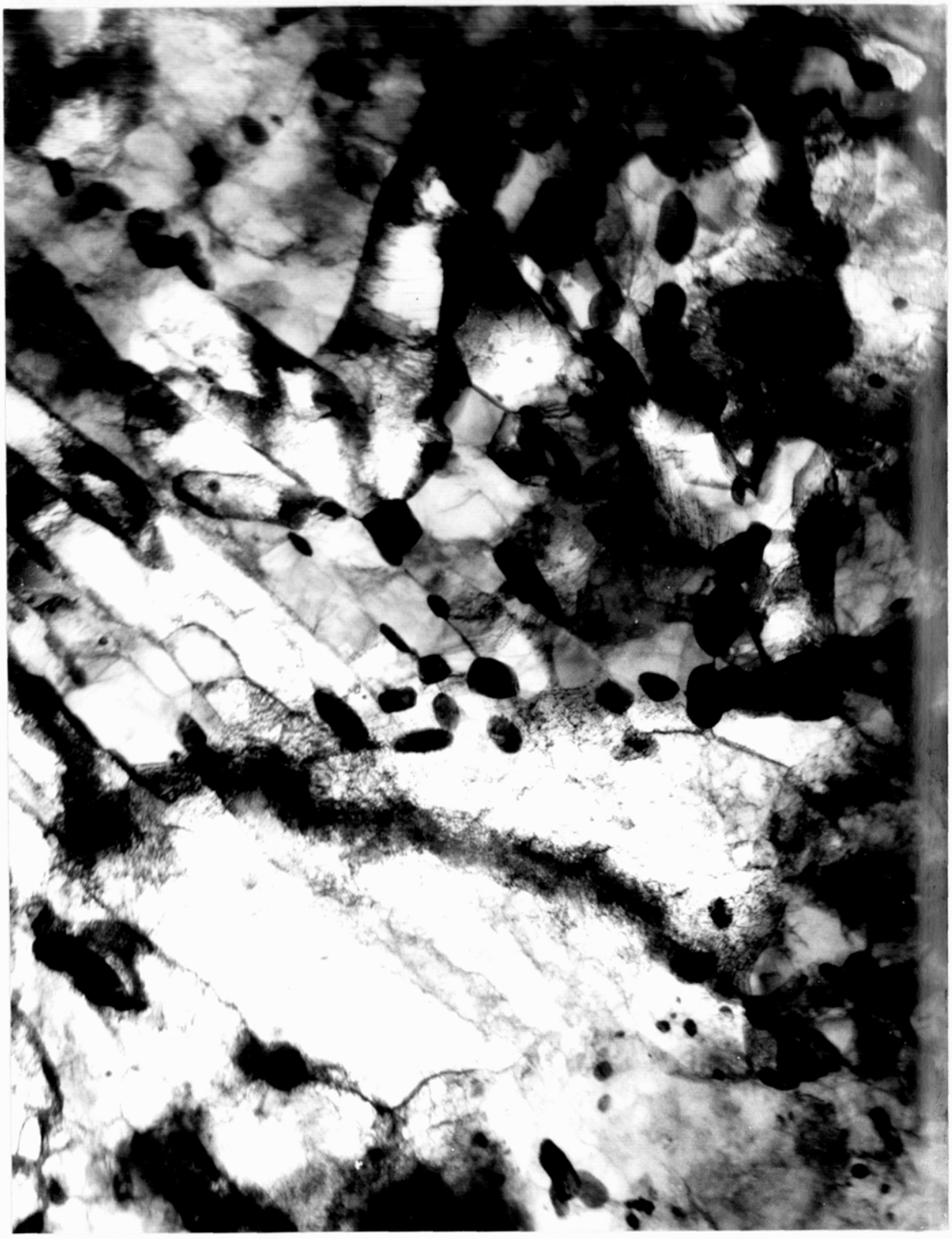


FIGURE 15. Plain carbon steel tempered for 1 hour.

(x 24 000)



FIGURE 16. Plain carbon steel tempered for 1 hour.

(x 60 000)



FIGURE 17. Plain carbon steel tempered for 1 hour.

(x 60 000)

tion density inside the martensite crystals was then reduced by the formation of grains and subgrains of ferrite in each prior martensite crystal. These boundaries seem to have formed so as to span the least possible distance, which would account for the large number of boundaries which traversed the width of the prior martensite crystals, approximately at 90° to the latter. The average area of a subgrain, A, was estimated by calculating the area covered by a particular photographic print and dividing this by the number of subgrains visible on the print. This was carried out for as many prints as possible and the various answers averaged. The values appeared to be quite close from print to print. The mean diameter, D, of subgrains was taken as $\lambda\sqrt{A}$.

(ii) Silicon steel, alloy No. 2

The type of structure in this alloy was similar to the basic plain carbon steel (alloy No. 1). However, the carbides were much smaller and so were the subgrains (see Figs. 18-20). There appeared to be a slightly higher dislocation density in the subgrains which indicated that the structure was relatively less tempered than the plain carbon steel. The mean subgrain diameter was 0.46 μm (85% of that of alloy 1).

The 2.0 weight % silicon present in this alloy amounted to 3.9 atom % which was 24 times the quantity of silicon



FIGURE 18, Silicon steel tempered for 1 hour.
(x 24 000)



FIGURE 19. Silicon steel tempered for 1 hour.

(x 60 000)



FIGURE 20. Silicon steel tempered for 1 hour.

(x 60 000)

which would be required to provide a close-packed monomolecular layer of silicon along all grain and subgrain boundaries and interphase boundaries (see Appendix 1).

(iii) Nickel steel, alloy No. 3

The addition of 2.78 weight % of nickel (amounting to 2.94 atom %) hardly affected the subgrain and carbide sizes. There was some tendency for the subgrains to be more equiaxed than the generally rectangular ones in the plain carbon steel (see Figs. 21-23). The average subgrain diameter was 0.60 μm., 11% greater than that of alloy 1, and the dislocation density inside these subgrains was very low. The carbides were slightly smaller than those in alloy 1.

The difference in the subgrain shapes was probably inherited from the prior martensite phase. Nickel addition usually modifies the morphology of the martensite and tends to coarsen the needles and even, with sufficient nickel, produces massive martensite (37).

The amount of nickel present was 25 times the quantity which would be required to provide a close-packed monomolecular layer of nickel atoms on all boundaries.

(iv) Phosphorus steel, alloy No. 4

Both carbides and subgrains were smaller than in alloy No. 1 and the dislocation density in the subgrains was generally quite high (see Figs. 24-26). This suggests that



FIGURE 21. Nickel steel tempered for 1 hour.

(x 24 000)



FIGURE 22. Nickel steel tempered for 1 hour.

(x 60 000)



FIGURE 23. Nickel steel tempered for 1 hour.

(x 60 000)

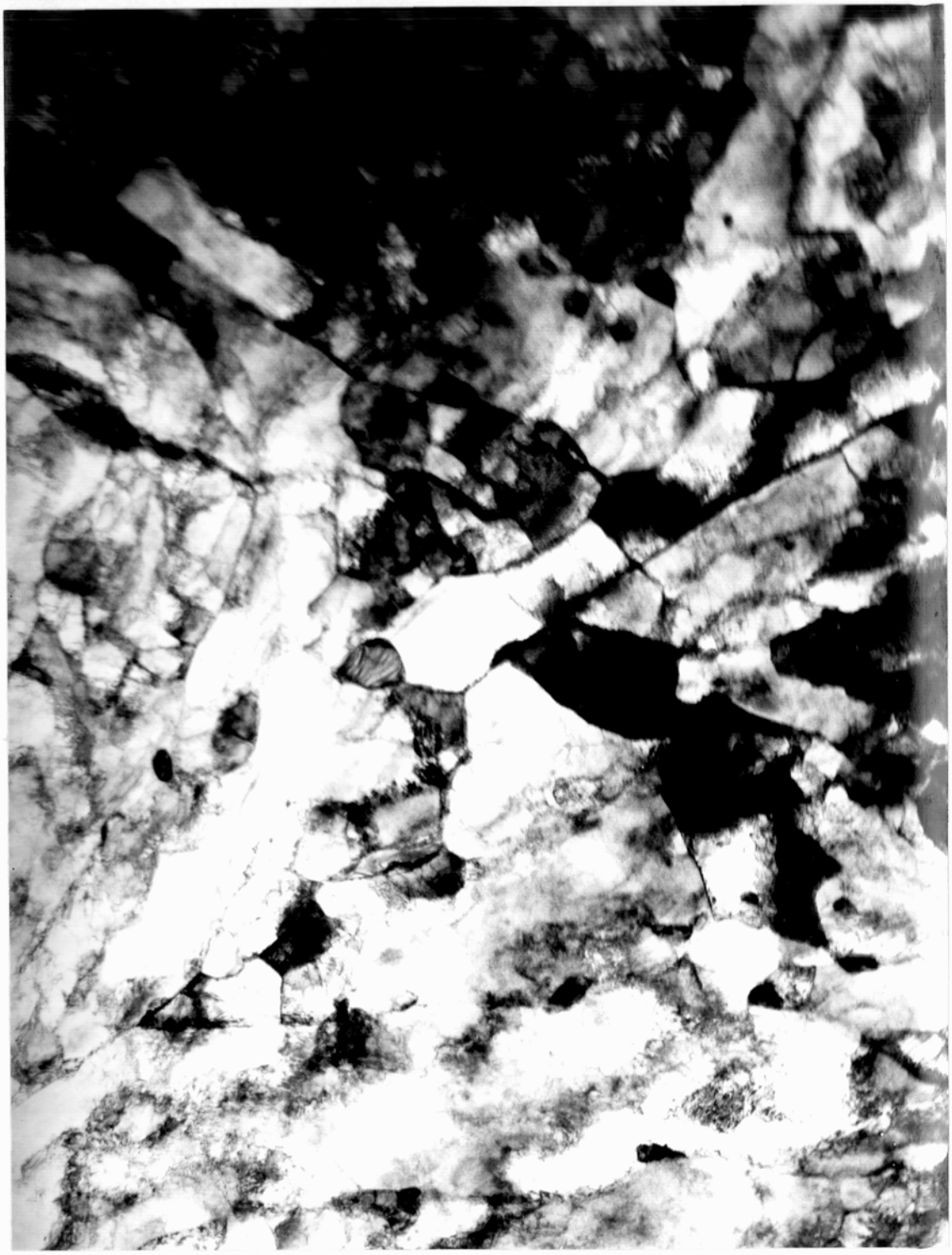


FIGURE 24. Phosphorus steel tempered for 1 hour.

(x 24 000)



FIGURE 25. Phosphorus steel tempered for 1 hour.

(x 60 000)



FIGURE 26. Phosphorus steel tempered for 1 hour.

(x 60 000)

tempering was not as far advanced as in alloy No. 1. The mean subgrain diameter was only 76% of that in alloy No. 1.

The 0.026 weight % phosphorus present in this alloy was 0.047 atom %, which was only 22% of that necessary for the formation of a close-packed monomolecular film along all boundaries in the steel.

(v) Tin steel, alloy No. 5

1.03 weight % tin in this alloy was 0.485 atom % which was 5.5 times the amount required to provide a close-packed monomolecular layer on all the boundaries. The subgrains were very narrow and somewhat smaller than in alloy No. 1, and the carbides were very small (50% of mean length of those in alloy 1) (see Figs. 27-30). The dislocation densities inside the subgrains were sometimes quite high and the dislocations tended to be uniformly distributed.

(vi) Nitrogen steel, alloy No. 6

The amount of nitrogen present was 0.014 weight %, which was 0.055 atom %. This amount was only 7% of that which would be required to provide a close-packed monomolecular layer on all boundaries in the steel. However, the carbides and the subgrains were smaller than those in alloy No. 1. The mean subgrain diameter was 87% of that for alloy No. 1, and the dislocation density within them was quite high (see Figs. 31-33).



FIGURE 27. Tin steel tempered for 1 hour.

(x 60 000)



FIGURE 28. (x 60 000)

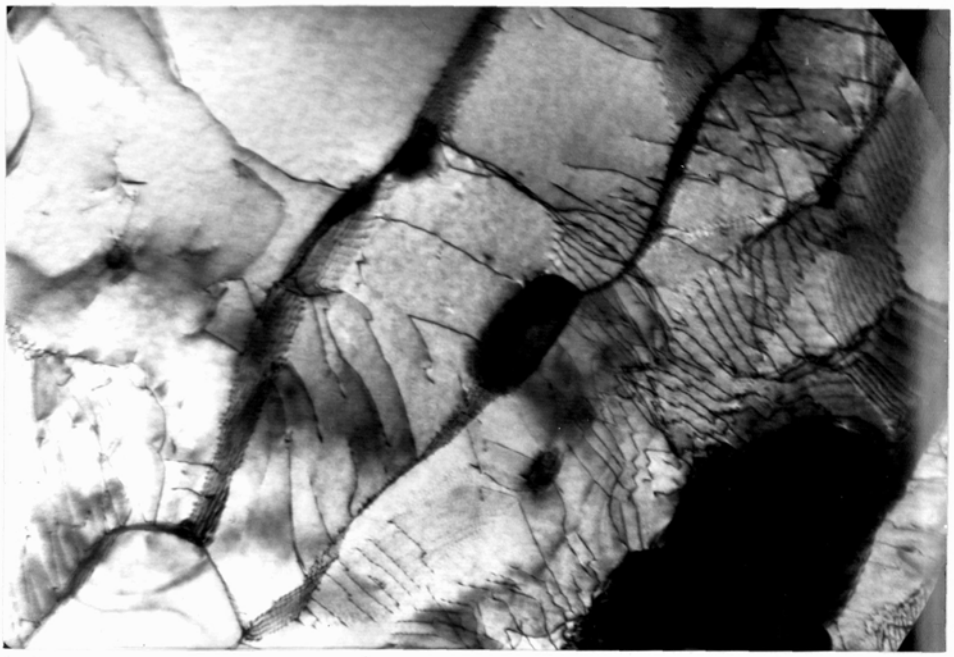


FIGURE 29. (x 60 000)

Figs. 28, 29 both tin steel tempered for 1 hour.



FIGURE 30. Tin steel tempered for 1 hour.

(x 120 000)

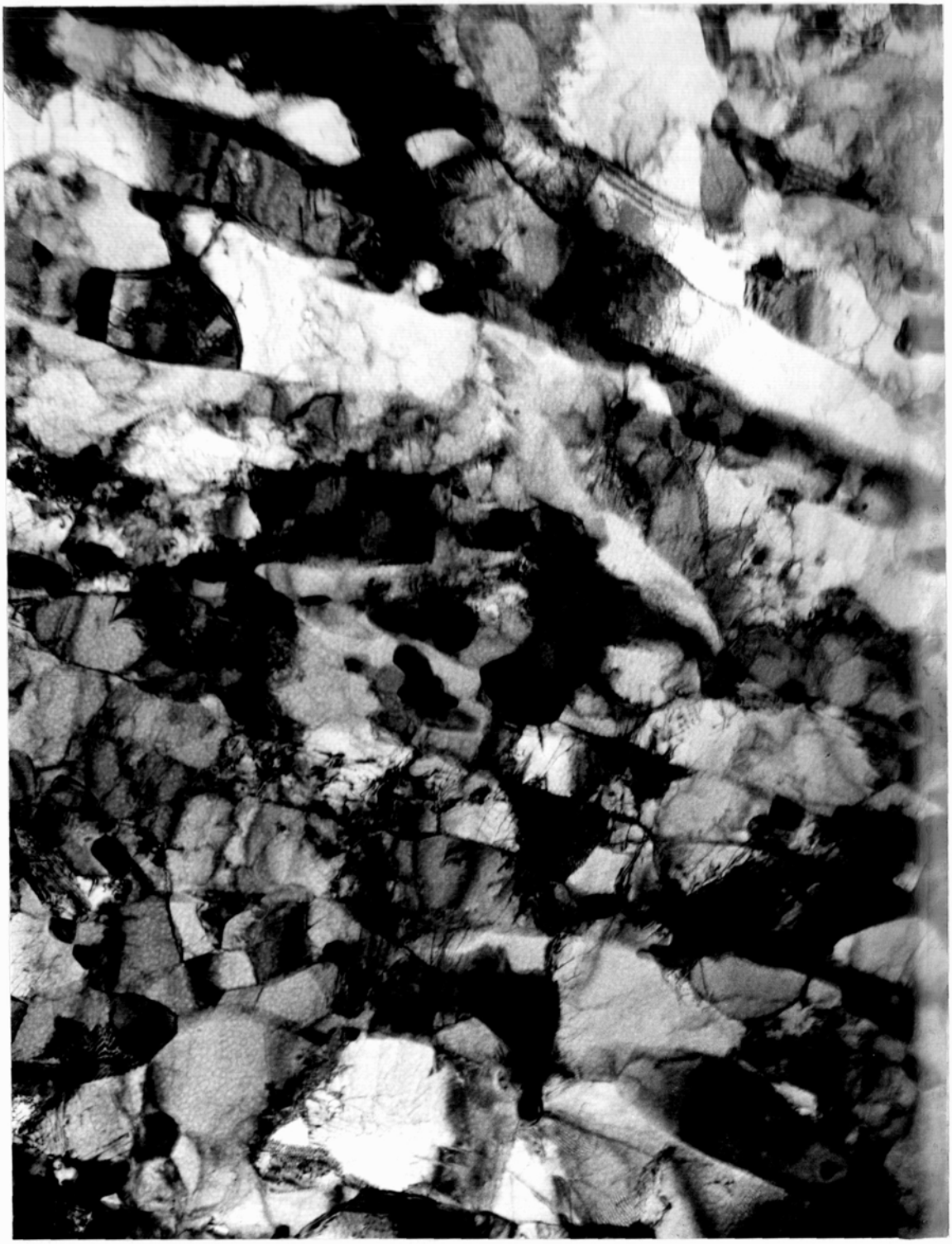


FIGURE 31. Nitrogen steel tempered for 1 hour.
(x 24 000)



FIGURE 32. Nitrogen steel tempered for 1 hour.

(x 60 000)



FIGURE 33. Nitrogen steel tempered for 1 hour.

(x 60 000)

3.1.3 Electron microscopy after tempering for 17 hrs.

(i) Plain carbon steel, alloy No. 1

The subgrains were very well-developed (see Figs. 34-37). There were very few dislocations which were not contained in subgrain boundaries ($< 10^5 cm^{-2}$). In the low-angle boundaries the dislocations were usually observed to have formed regular networks. The carbides still occurred at grain and subgrain boundaries; those on high-angle boundaries were larger than those on low-angle ones, however, and this observation applies to all six alloys when tempered for seventeen hours.

The mean value of the major axes of carbides on high-angle boundaries was 0.58 μm. and of those on low-angle boundaries was approximately half this. The larger of these is twice that occurring when the alloy is tempered for one hour. The mean subgrain diameter was 1.0 μm. which is also about twice greater than when tempered for one hour.

(ii) Silicon steel, alloy No. 2

The structure after seventeen hours' tempering was not very different from that after one hour's tempering for this alloy. Carbides and subgrains were very slightly enlarged (see Figs. 38-40), and the carbides exhibited the same duplex populations of size as did those in all six alloys when tempered for seventeen hours. In this alloy



FIGURE 34. Plain carbon steel tempered for 17 hours.

(x 24 000)



FIGURE 35. Plain carbon steel tempered for 17 hours.

(x 60 000)

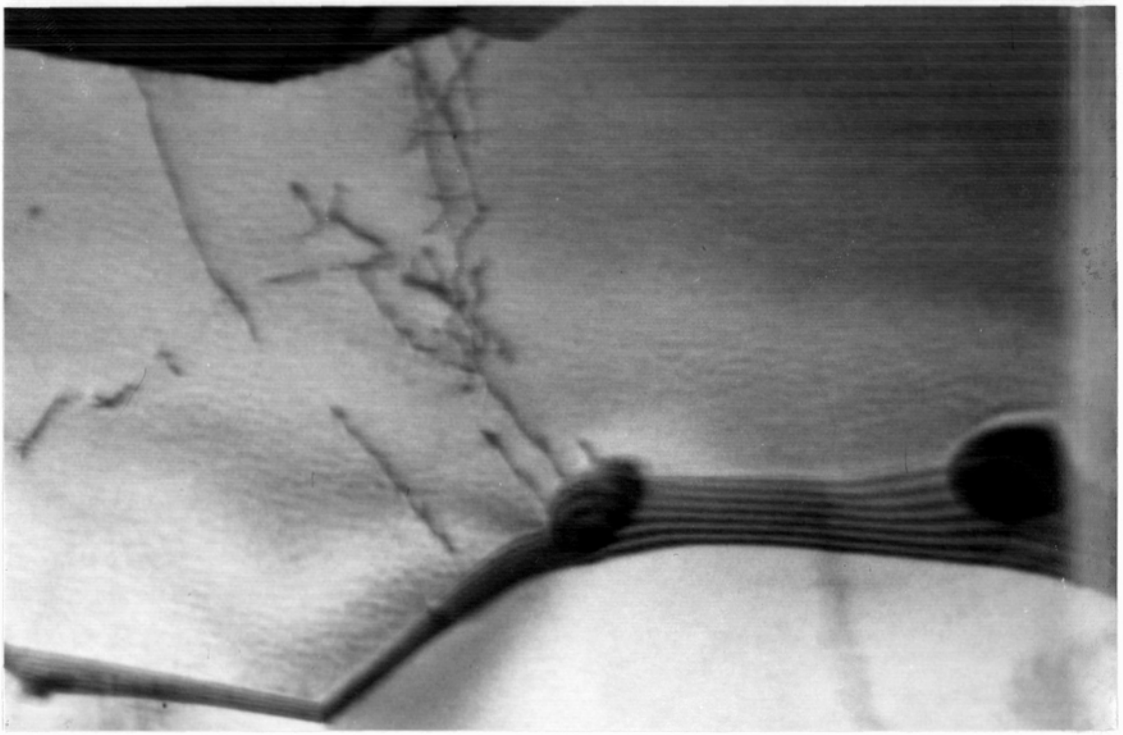


FIGURE 36. (x 60 000)

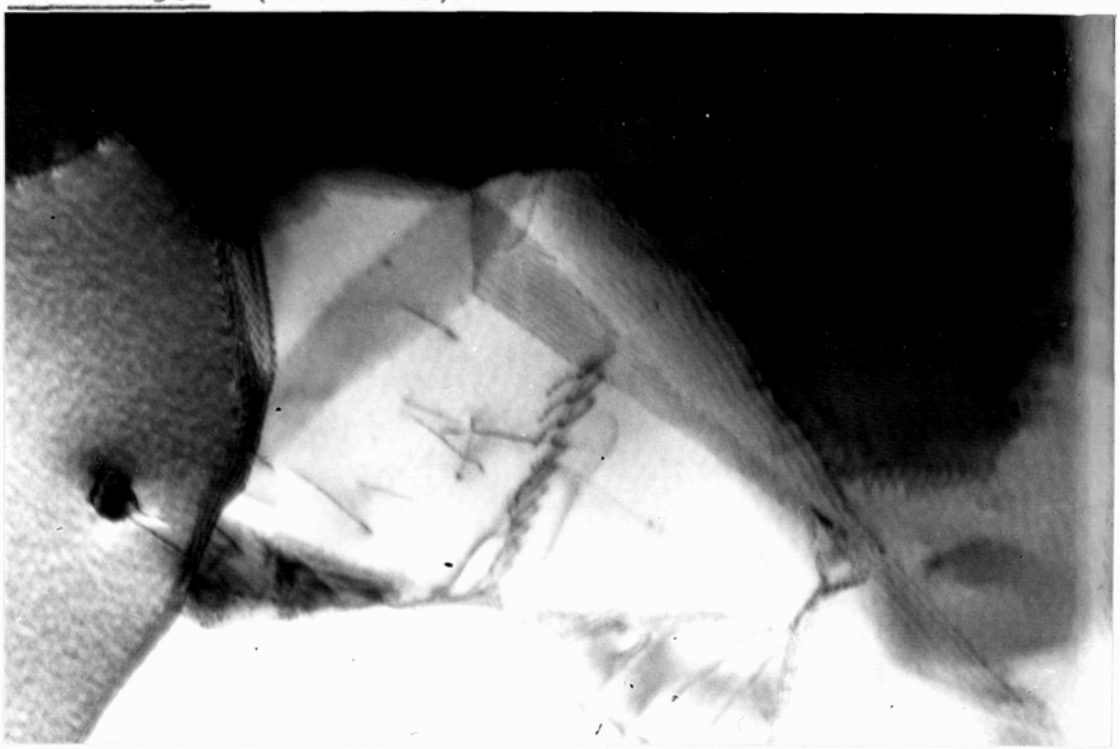


FIGURE 37. (x 60 000)

Figs. 36, 37 both plain carbon steel tempered for 17 hours.

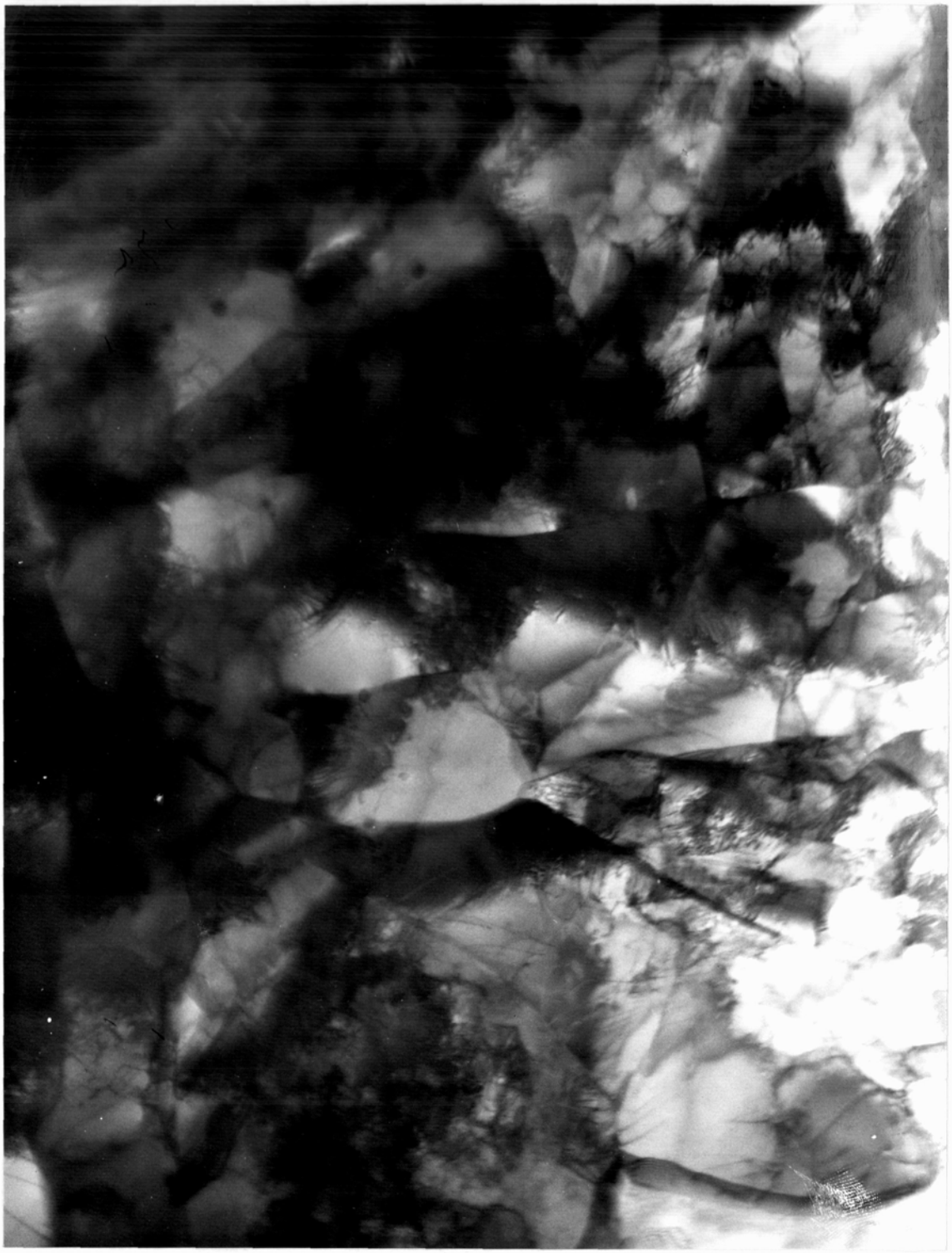


FIGURE 38. Silicon steel tempered for 17 hours.

(x 24 000)

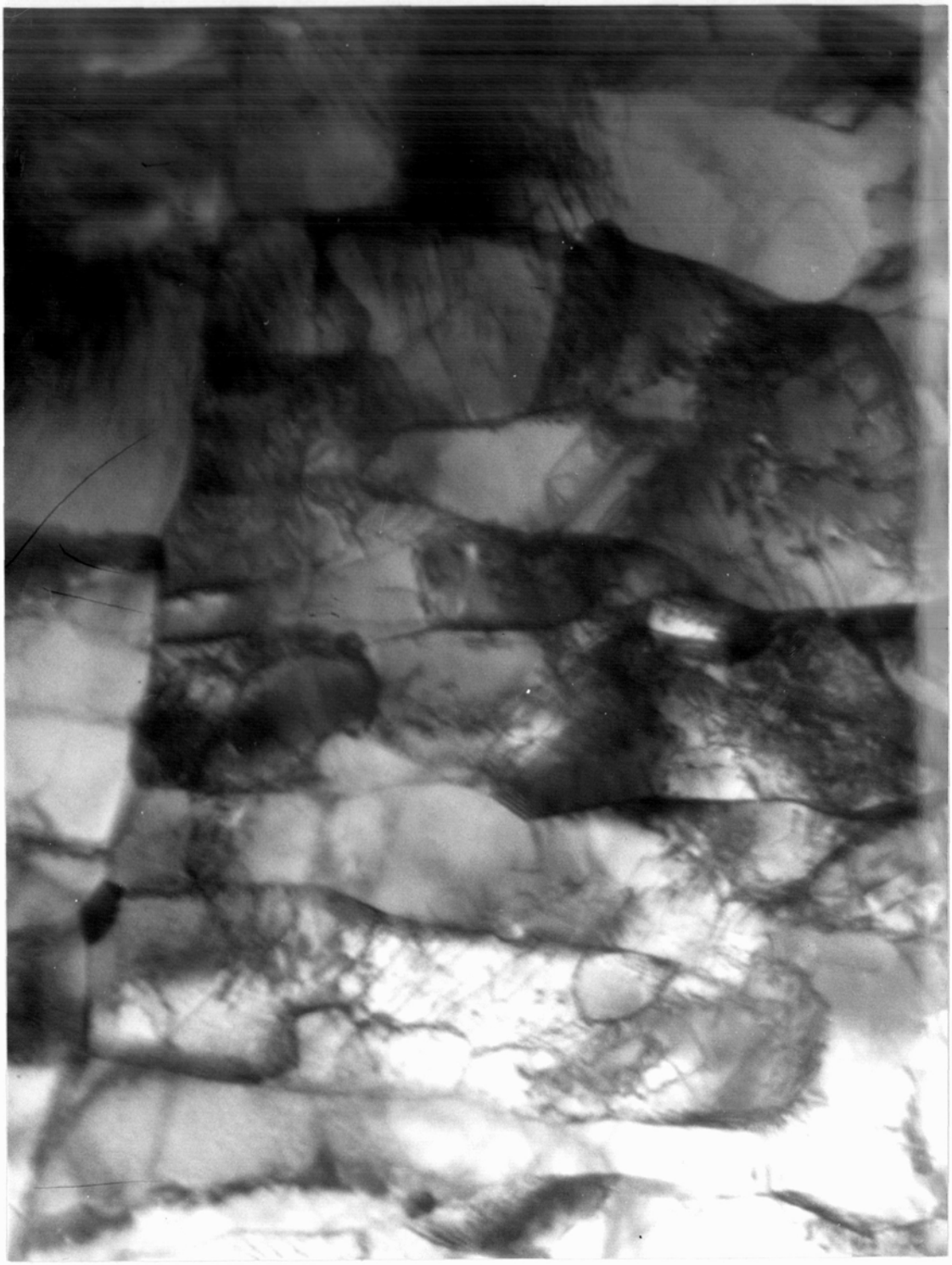


FIGURE 39. Silicon steel tempered for 17 hours.

(x 60 000)



FIGURE 40. Silicon steel tempered for 17 hours.

(x 60 000)

there was even some indication of precipitation on dislocations within the subgrains (see Fig. 40).

The amount of silicon present was 26 times the amount which would be required to form a continuous monomolecular layer along all boundaries in the steel. The dislocation density in the subgrains was still comparatively high. In general then, the substructure of this alloy was changed very little by tempering for the extra time.

(iii) Nickel steel, alloy No. 3

The subgrain size was not increased very much during the increased tempering time. The mean subgrain diameter was 0.64 μm. whilst the carbides on the high-angle boundaries averaged 0.71 μm. long and those on the low-angle boundaries averaged 0.38 μm. long (see Figs. 41-44).

The amount of nickel present was 27 times the amount which would be required to provide a close-packed monomolecular layer over all boundaries in this alloy.

(iv) Phosphorus steel, alloy No. 4

The subgrain size had been considerably increased by the extra tempering and the carbides were also much enlarged, particularly those on high-angle boundaries (see Figs. 45-47). There were very few dislocations which were not involved in the structure of boundaries; and the low-angle boundaries were quite uniform arrays of dislocations.

The amount of phosphorus present in this alloy would



FIGURE 41. Nickel steel tempered for 17 hours.

(x 24 000)



FIGURE 42. Nickel steel tempered for 17 hours.

(x 60 000)

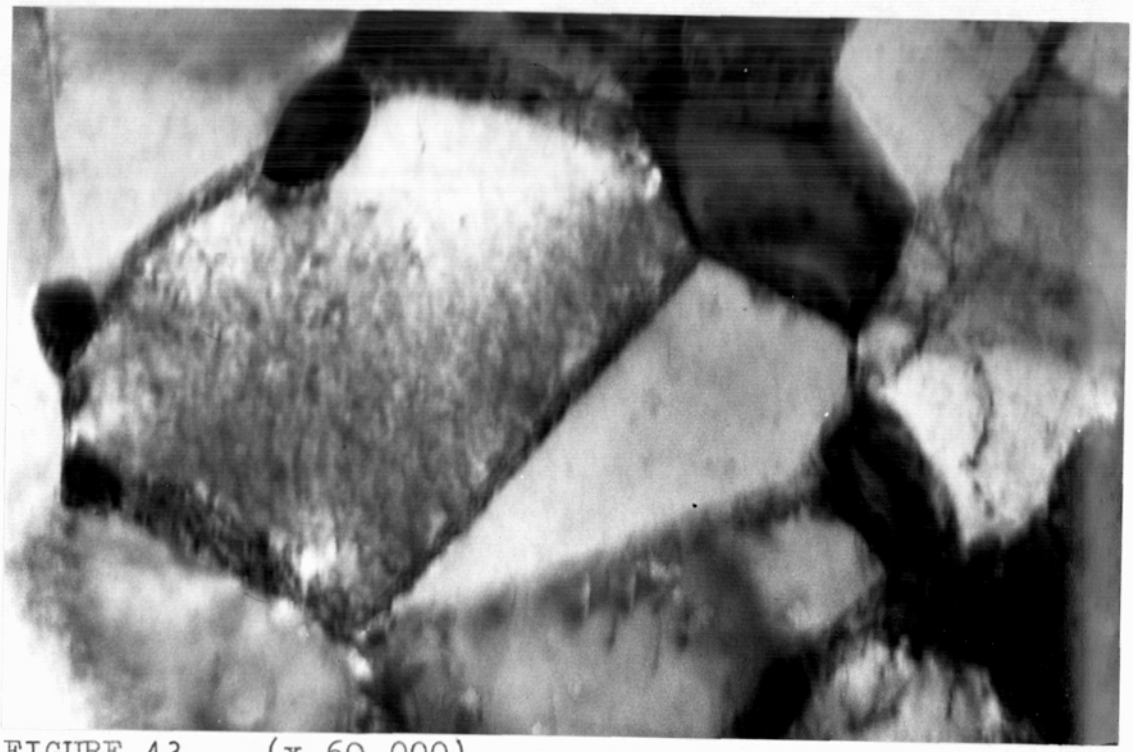


FIGURE 43. (x 60 000)



FIGURE 44. (x 60 000)

Figs. 43, 44 both nickel steel tempered for 17 hours.



FIGURE 45. Phosphorus steel tempered for 17 hours.

(x 24 000)



FIGURE 46. Phosphorus steel tempered for 17 hours.
(x 60 000)



FIGURE 47. Phosphorus steel tempered for 17 hours.

(x 60 000)

have been 36% of that required to form a monomolecular close-packed layer of phosphorus atoms on all boundaries in the structure.

(v) Tin steel, alloy No. 5

The mean subgrain size exhibited a considerable increase from the condition after one hours' tempering. The carbides were larger also and those on high-angle boundaries were larger than those in alloy No. 1 tempered for the same time. There were still dislocations within subgrains and some precipitation had occurred on them (see Figs. 48-50).

(vi) Nitrogen steel, alloy No. 6

Some precipitation had occurred on dislocations within subgrains as was observed in alloy No. 5, and the mean subgrain diameter was approximately twice that after one hours tempering (see Figs 51-53).

The amount of nitrogen present was 13% of that which would have been required to provide a close-packed monomolecular layer of nitrogen atoms along all boundaries.



FIGURE 48. Tin steel tempered for 17 hours.

(x 24 000)



FIGURE 49. Tin steel tempered for 17 hours.

(x 60 000)

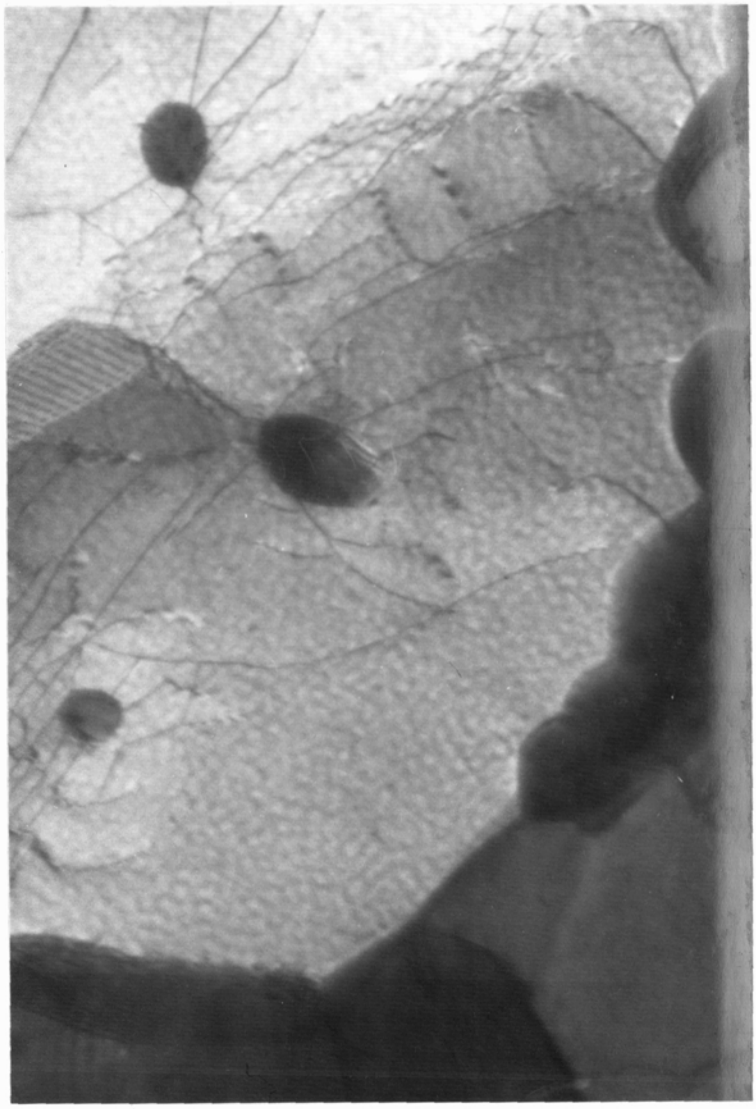


FIGURE 50. Tin steel tempered for 17 hours.

(x 60 000)



FIGURE 51. Nitrogen steel tempered for 17 hours.

(x 24 000)



FIGURE 52. Nitrogen steel tempered for 17 hours.
(x 60 000)



FIGURE 53. Nitrogen steel tempered for 17 hours.

(x 60 000)

TABLE 2. QUANTITATIVE RESULTS FROM MICROSTRUCTURAL INVESTIGATION

	TEMPERING TIME, hrs.	ALLOYS					
		1	2	3	4	5	6
		plain	+Si	+Ni	+P	+Sn	+N
SUBGRAIN MEAN AREA μm^2 = A.	1	0.29	0.21	0.36	0.17	0.26	0.22
	17	1.00	0.26	0.41	0.44	0.67	0.75
SUBGRAIN MEAN DIAM., $D = \sqrt{A}$, μm.	1	0.54	0.46	0.60	0.41	0.51	0.47
	17	1.00	0.51	0.64	0.66	0.82	0.87
CARBIDE MEAN MAJOR AXIS, μm.	1	0.29	0.14	0.26	0.22	0.19	0.24
	17	0.58	0.18	0.71	0.67	0.70	0.55

3.1.4 Selected area electron diffraction results

No extensive diffraction experiments were performed, as in all the alloys in all conditions observed, the carbides present were easily recognisable. With further tempering these would have been resolvable in optical microscopes and identified visually as cementite rather than more metastable carbides such as the epsilon phase. This was only possible because the initial stages of tempering were not investigated. However, some single crystal diffraction patterns were obtained and these

appear as Figs. 54 to 60 inclusive.

3.1.4(i) Ferrite matrix

TABLE 3.

Figure No.	Assumed Value	Measured Value, Å.	A.S.T.M. Value Å.	Beam Axis
54	$d_{(110)} = 2.03$Å	$d_{(200)} = 1.42$	1.43	[001]
56	$d_{(110)} = 2.03$Å	$d_{(211)} = 1.17$	1.17	[111]
57	$L\lambda = 4.25$ cm.Å.	$d_{(110)} = 1.98$	2.03	
		$d_{(200)} = 1.42$	1.43	
		$d_{(310)} = 0.884$	0.91	[001]
60	$L\lambda = 4.25$ cm.Å.	$d_{(110)} = 2.04$	2.03	
		$d_{(200)} = 1.46$	1.43	
		$d_{(310)} = 0.91$	0.9	[001]

The camera constant, $L\lambda$ was (4.25 ± 0.10) cm.Å. for the patterns in Figs. 54 to 60 with the exceptions of Figs. 55 and 58 which are discussed later.

Fig. 57 is the same pattern as the ferrite part of Fig. 54, and very faint spots may be observed due to the streaked reflections from the next plane in reciprocal space. This indicates that the foil was very thin. Such streaked reciprocal lattices allow considerable

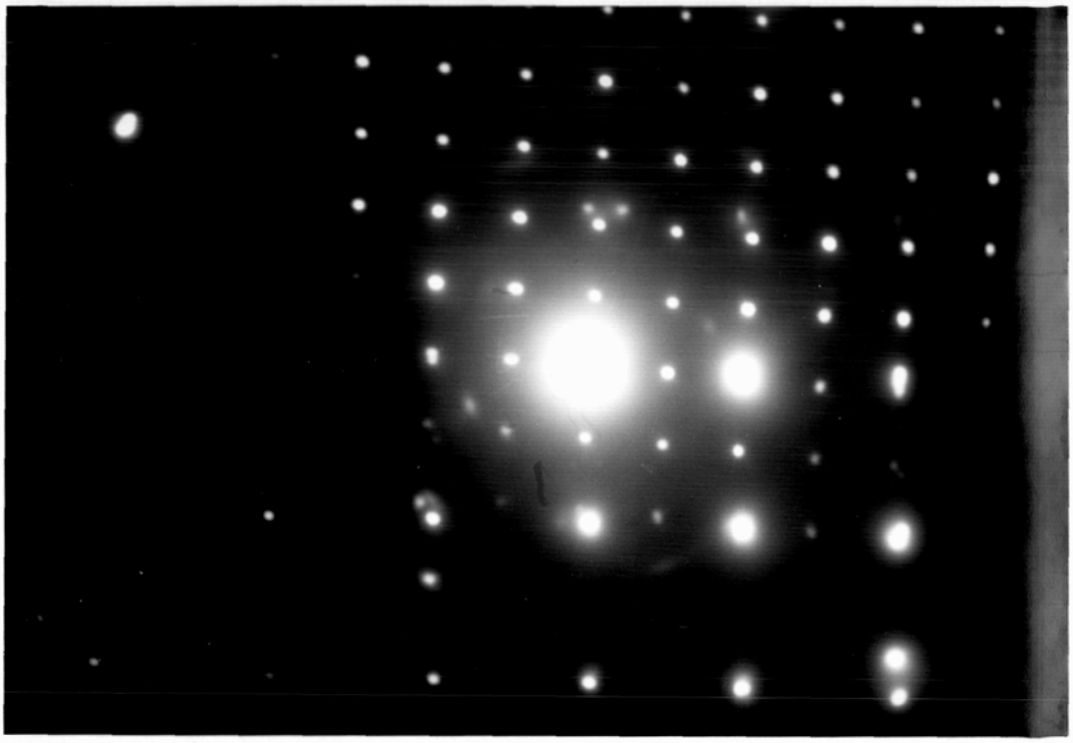


FIGURE 54. Phosphorus steel tempered for 17 hours.

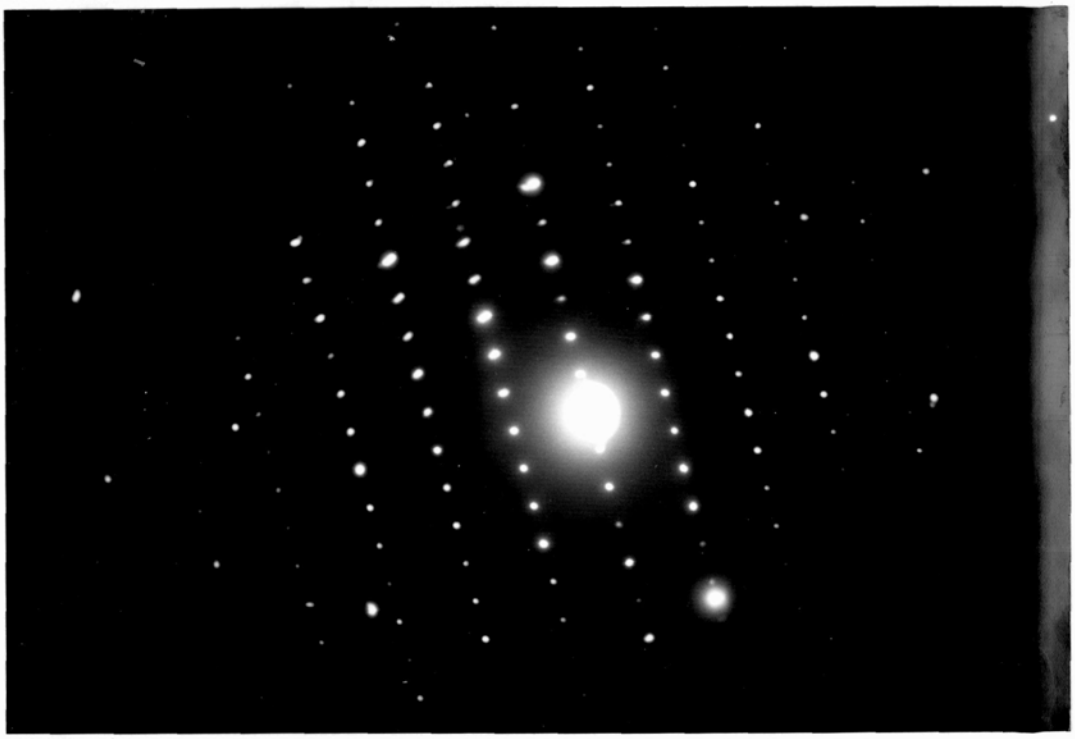


FIGURE 55. Phosphorus steel tempered for 17 hours.



FIGURE 56. Phosphorus steel tempered for 17 hours.

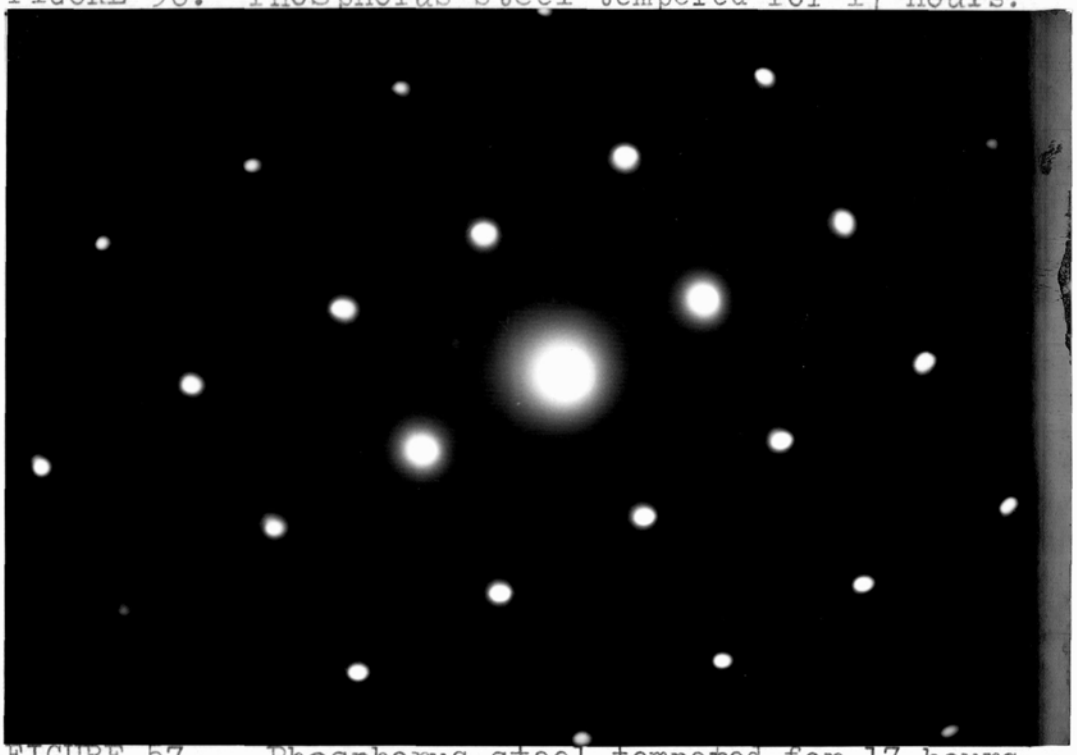


FIGURE 57. Phosphorus steel tempered for 17 hours.

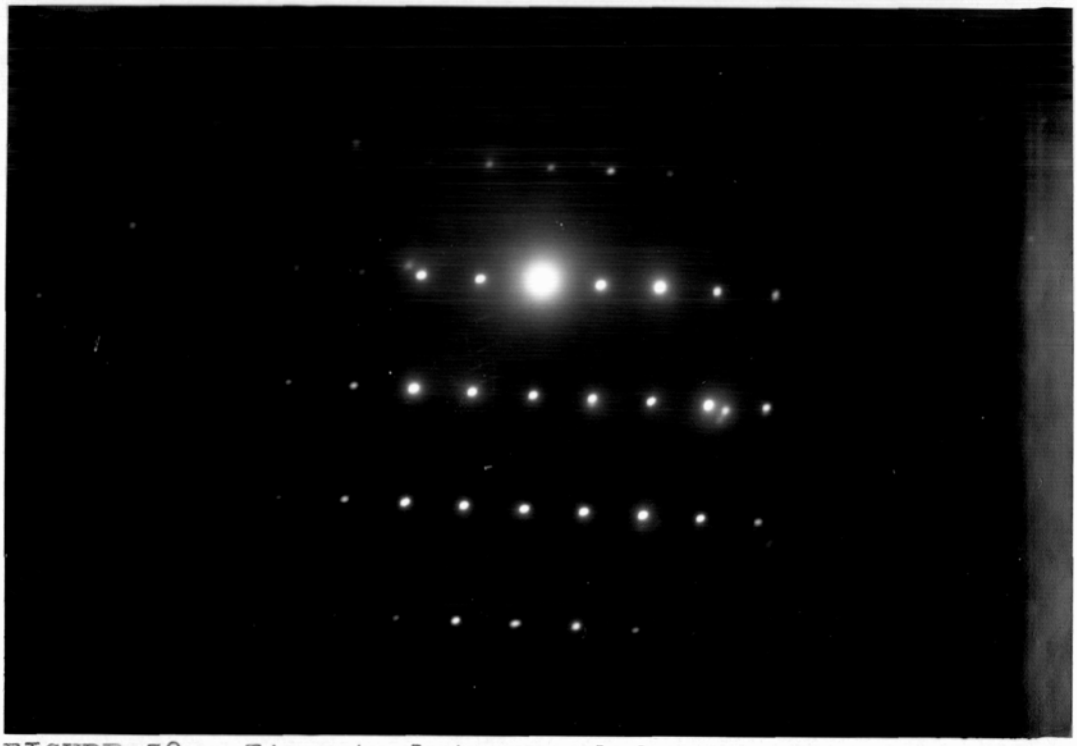


FIGURE 58. Tin steel tempered for 17 hours.



FIGURE 59. Tin steel tempered for 17 hours.

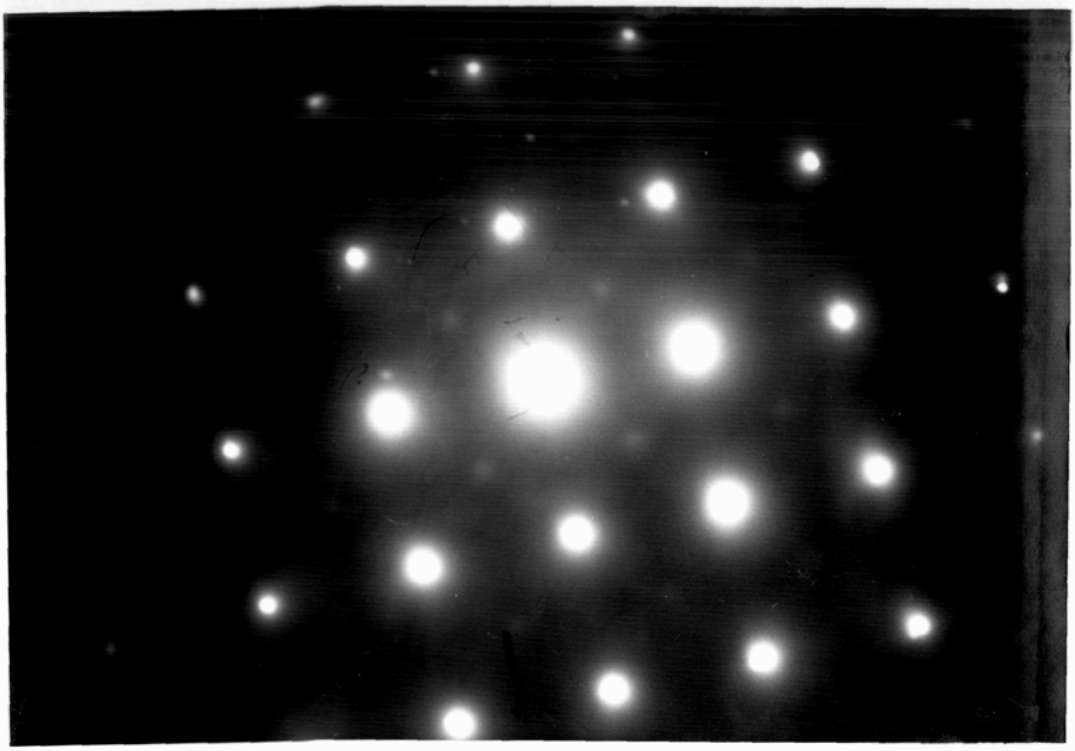


FIGURE 60. Tin steel tempered for 17 hours.

misorientation of the foil while still giving a good spot pattern. Fig. 60 also exhibits these faint additional spots.

3.1.4(ii) Cementite precipitates

Fig. 54 also contains a pattern derived from cementite which has a primitive orthorhombic structure (see Table 4).

In order to obtain good single crystal diffraction patterns from the relatively few carbides it was necessary to utilise the capabilities of the Valdre tilting stage to the utmost degree. This had the effect of varying the height of the specimen carbide with respect to the objective lens, which necessitated re-focussing as tilting was performed. In practice it was possible to exceed the adjustment range of the objective lens current on the high end of the range. (This was partly due to the non-standard pole-piece in the objective lens of the particular Siemens microscope used.) Because of the electron-optical conditions during selected area diffraction, in particular the short focal length of the objective lens, the height of the specimen greatly affected the magnitude of the camera constant, $L\lambda$. This is illustrated by Fig. 55 where $L\lambda$ is 3.52 cm.Å., and by Fig. 58 where $L\lambda$ is 5.15 cm.Å.

TABLE 4.

Figure No.	Assumed value of $L\lambda$, cm.Å.	Measured lattice parameter, Å.	A.S.T.M. value, Å.
54	4.25	$d_{(100)} = 4.47$	4.52
		$d_{(0\bar{1}1)} = 4.09$	4.06
		$d_{(1\bar{1}1)} = 3.01$	3.02
55	4.25	$d_{(001)} = 6.74$	6.74
		$d_{(1\bar{1}0)} = 3.47$	3.38
		$d_{(1\bar{1}2)} = 2.43$	2.38
58	5.15	$d_{(001)} = 6.74$	6.74
		$d_{(1\bar{1}0)} = 3.42$	3.38
59	4.25	$d_{(0\bar{1}0)} = 5.12$	5.09
		$d_{(101)} = 3.76$	3.75

The values of some interplanar spacings were obtained from the A.S.T.M. Card File and others were calculated from the equation :-

$$\frac{1}{d^2} = \frac{(h)^2}{(a)} + \frac{(k)^2}{(b)} + \frac{(l)^2}{(c)}$$

Diffraction patterns were obtained to confirm that the precipitates were orthorhombic cementite, as appeared probable from the micrographs, and not epsilon carbide.

Detailed study of the ways in which the solute elements affected the lattice parameters of the cementite was not attempted.

3.2 Characterisation of fracturing

3.2.1 Fractography

The appearance of the fracture surfaces of a Charpy test-piece is characteristic of the mode of fracture. A brittle fracture is usually lustrous and should pass through the specimen at 90° to its longitudinal axis, no macroscopic plastic deformation occurring. At temperatures well above the brittle/ductile transition range, the specimen may not be completely fractured. Such specimens exhibited very extensive plastic deformation and pronounced shear lips. Examples of these extreme forms of fracture may be seen in Fig. 9, together with some in the transition range of temperature which exhibit some macroscopic evidence of plastic flow but where the fracture surface is still quite flat.

Observation of brittle fracture surfaces was performed by replication and electron microscopy, and the results are shown as Figs. 61 to 64 inclusive. It is apparent that a certain amount of plastic deformation has occurred locally but that the major part of the fracture had occurred by brittle cleavage. The river markings so characteristic of this type of fracture are best revealed on Fig. 61.

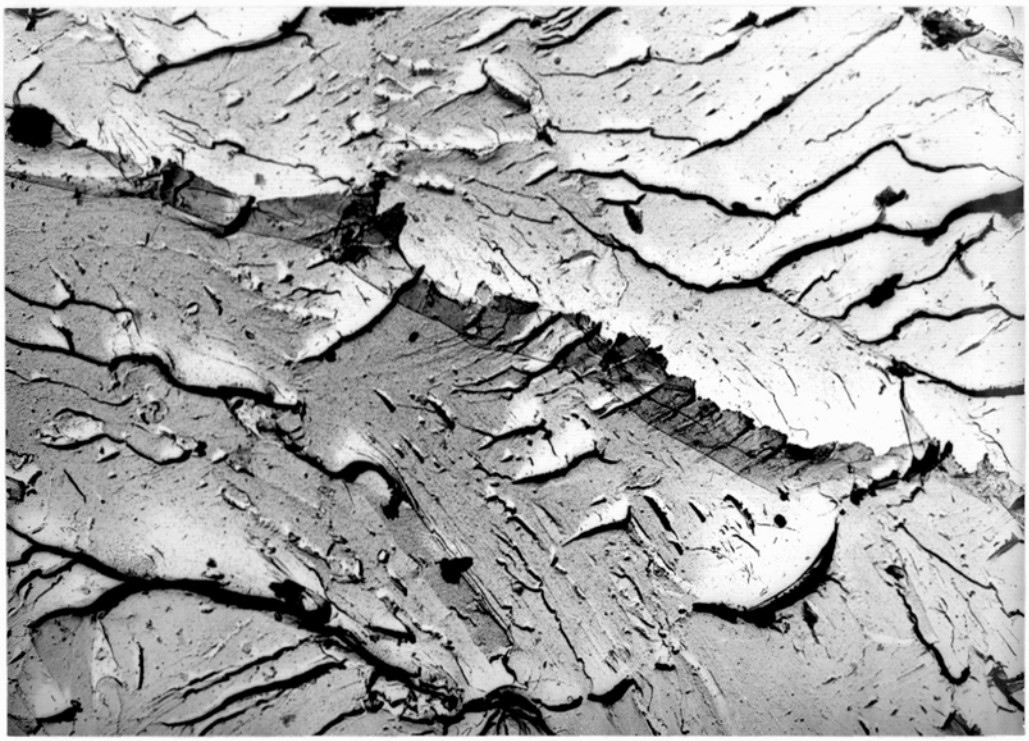


FIGURE 61. (x 5 000)

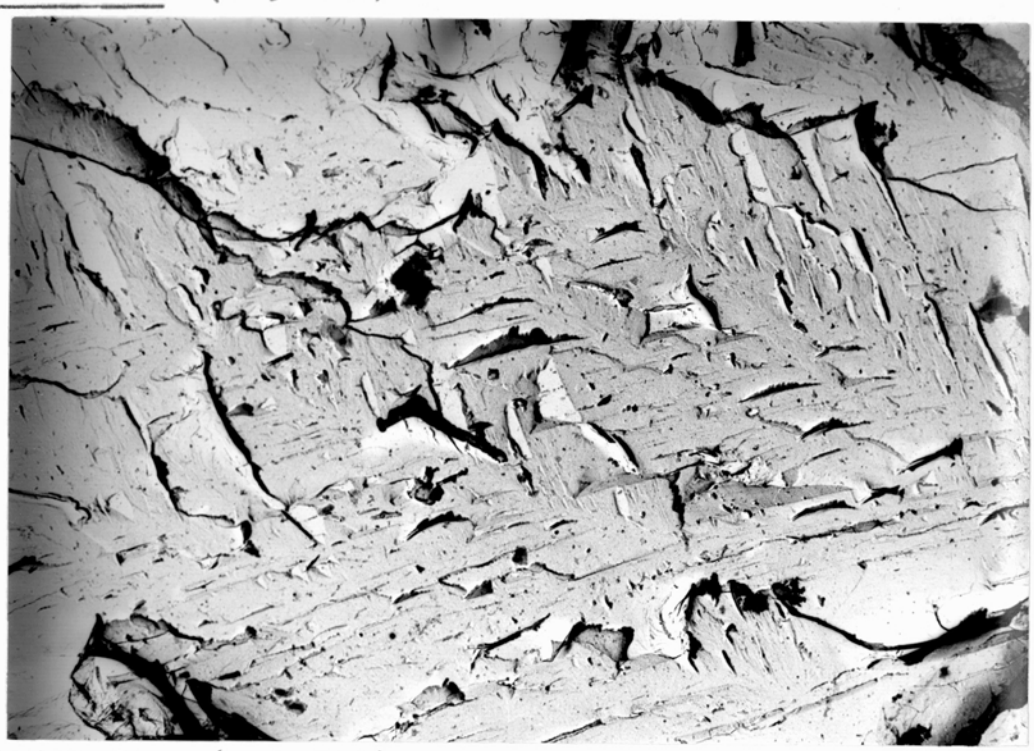


FIGURE 62. (x 5 000)

Figs. 61, 62 both l.A.T.l. broken at -196°C.



FIGURE 63. (x 5 000)

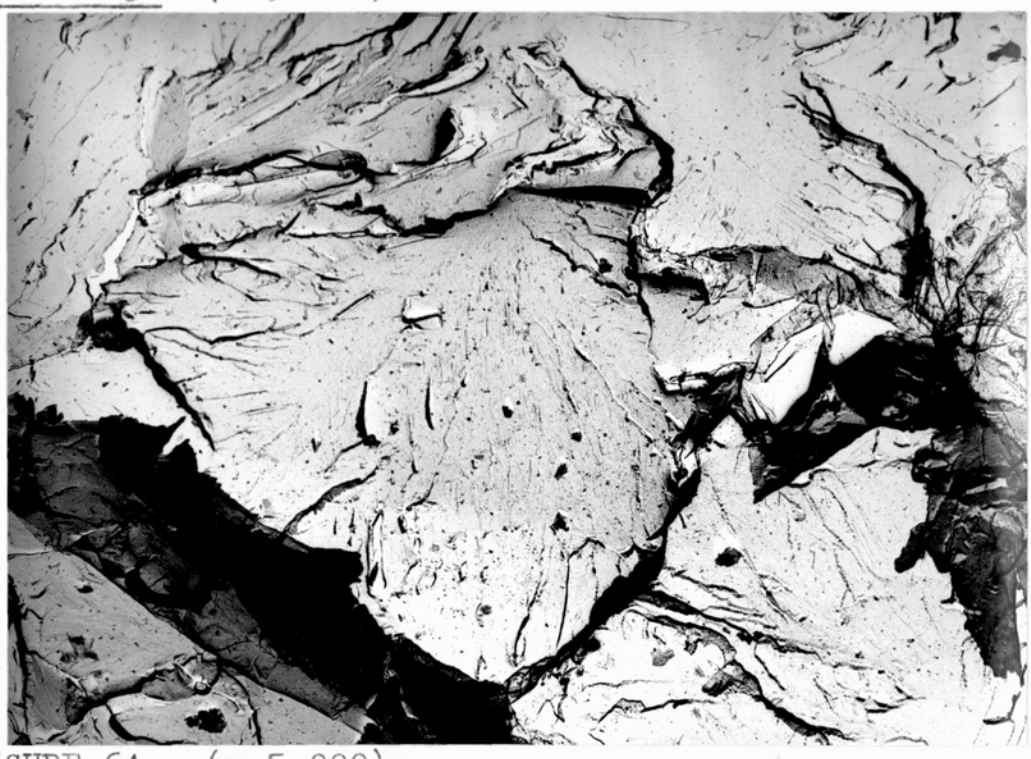


FIGURE 64. (x 5 000)

Figs. 63, 64 both l.A.T.l. broken at -196°C.

Figs. 62 and 63 show regions containing many tongues on the fracture surface which are caused by the brittle cleavage of deformation twins produced ahead of the propagating crack.

Fig. 64 reveals an area with a fan-like array of river markings indicating a source of fracture in that area. Surrounding areas had different directions of propagation of cracks. This indicates that general failure was preceded by many local fractures which finally joined by secondary cleavage or by ductile shearing locally as the surfaces were forced to separate.

3.2.2 Charpy results

Izod-notched standard Charpy specimens were broken under impact conditions in 3-point bending at various temperatures within the range from -196°C to +250°C. Specimens of all six alloys were available in four heat-treated conditions as follows.

All the steel was austenitised at 950°C for three hours at temperature in a protective atmosphere of argon. This was followed by quenching into iced brine and tempering at 650°C in argon for the following times :

(1) One hour. Terminated by natural convection cooling in air. Total cooling time to approximately 100°C was about 4 minutes, an average of 2.6°C/sec.

(2) One hour. Terminated by quenching in cold water. Total cooling time to approximately 100°C was approximately 4 seconds, averaging 160°C/sec., although the outermost regions of the cylindrical billets must have been cooled in a small fraction of this time.

(3) 6 hr. 43 min. Terminated by quenching as above.

(4) 17 hours. Terminated by quenching as above.

The results were expressed in ft.lb_f. for ease of comparison with past results, and were plotted for each alloy against testing temperature. Two test-pieces of each alloy in all heat treatment conditions were broken at each temperature. The average of the two values of energy absorbed during fracture was used for the graphs (Figs. 65 to 70 inclusive).

Each pair of test-pieces often gave identical or very close results, but sometimes quite wide differences could be obtained, particularly in the transition range of temperature. The specimen testing procedure was carefully standardised to reduce machine error to a minimum value and the testing was performed by experienced operators to reduce operator error to a minimum. Consequently, when wide differences in results were obtained for members of a pair of test-pieces the most likely reasons were :

(1) possible variations in notch root radius or machining marks which might have influenced crack nucleation.

(2) possible variation in notch root position and

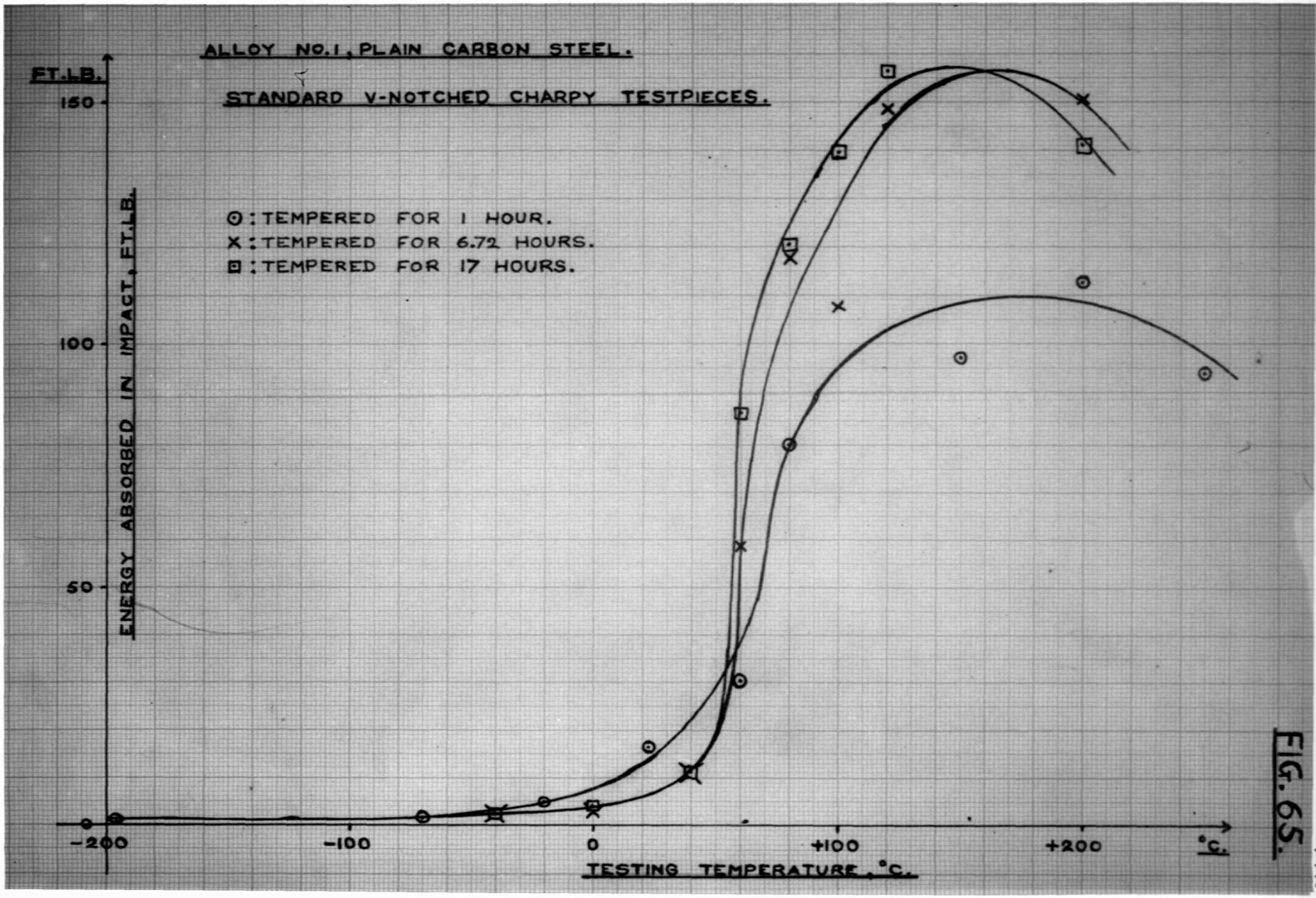

ALLOY NO.1, PLAIN CARBON STEEL.
STANDARD V-NOTCHED CHARPY TESTPIECES.
⊙ : TEMPERED FOR 1 HOUR.
× : TEMPERED FOR 6.72 HOURS.
⊡ : TEMPERED FOR 17 HOURS.
FT.LB.
150
100
50
ENERGY ABSORBED IN IMPACT, FT.LB.
-200
-100
0
+100
+200
°C.
TESTING TEMPERATURE, °C.

FIG. 65.

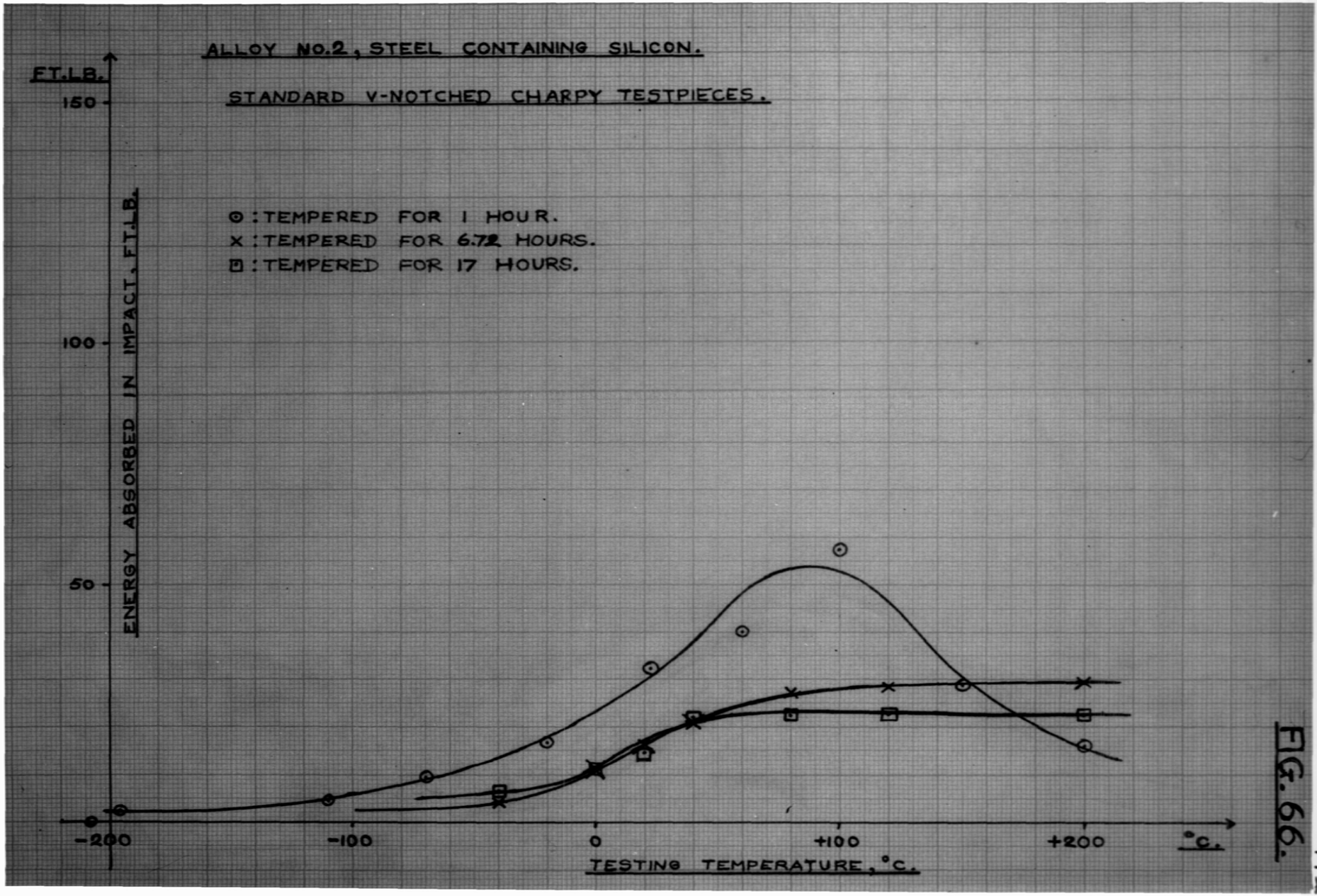

ALLOY NO.2, STEEL CONTAINING SILICON.
STANDARD V-NOTCHED CHARPY TESTPIECES.
⊙ : TEMPERED FOR 1 HOUR.
× : TEMPERED FOR 6.72 HOURS.
⊡ : TEMPERED FOR 17 HOURS.
FT.LB.
150
100
50
ENERGY ABSORBED IN IMPACT, FT.LB.
-200
-100
0
+100
+200
°C.
TESTING TEMPERATURE, °C.

FIG. 66.

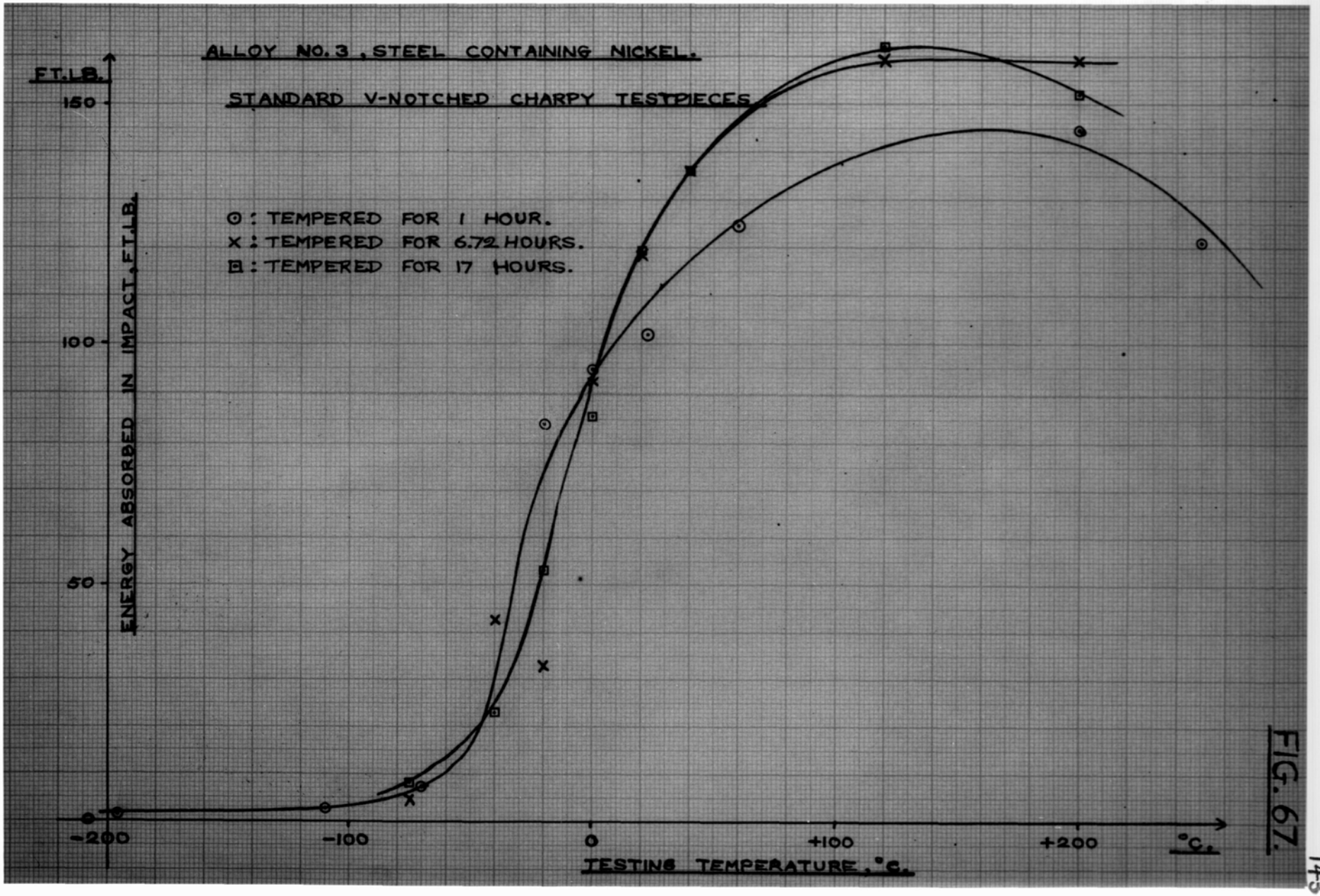

ALLOY NO. 3, STEEL CONTAINING NICKEL.
STANDARD V-NOTCHED CHARPY TESTPIECES.
⊙ : TEMPERED FOR 1 HOUR.
× : TEMPERED FOR 6.72 HOURS.
⊡ : TEMPERED FOR 17 HOURS.
FT.LB.
150
100
50
ENERGY ABSORBED IN IMPACT, FT.LB.
-200
-100
0
+100
+200
°C.
TESTING TEMPERATURE, °C.

FIG. 67.

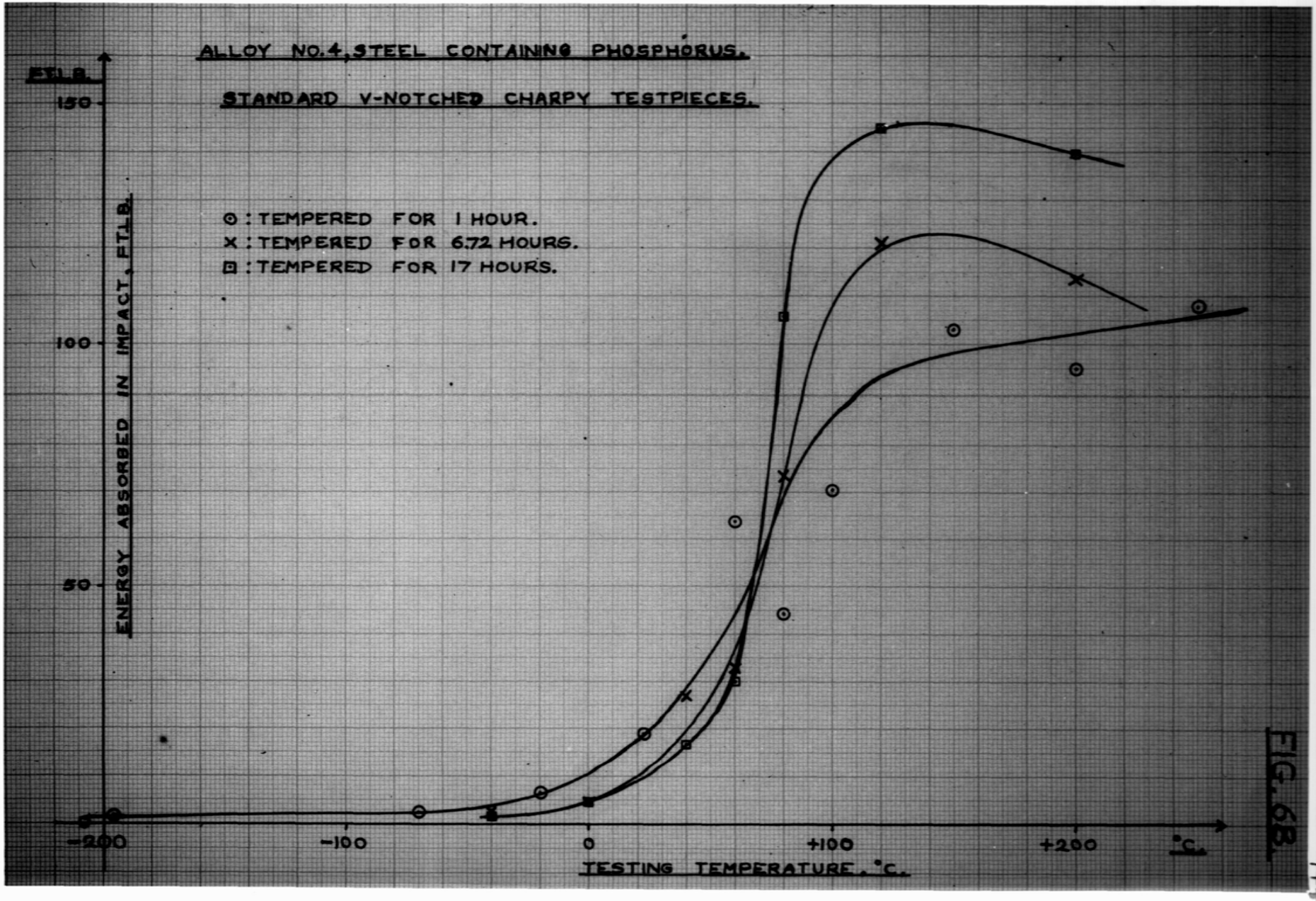

ALLOY NO. 4, STEEL CONTAINING PHOSPHORUS.
STANDARD V-NOTCHED CHARPY TESTPIECES.
⊙ : TEMPERED FOR 1 HOUR.
X : TEMPERED FOR 6.72 HOURS.
⊡ : TEMPERED FOR 17 HOURS.
FT.LB.
150
100
50
ENERGY ABSORBED IN IMPACT, FT.LB.
-200
-100
0
+100
+200
°C.
TESTING TEMPERATURE, °C.

FIG. 68.

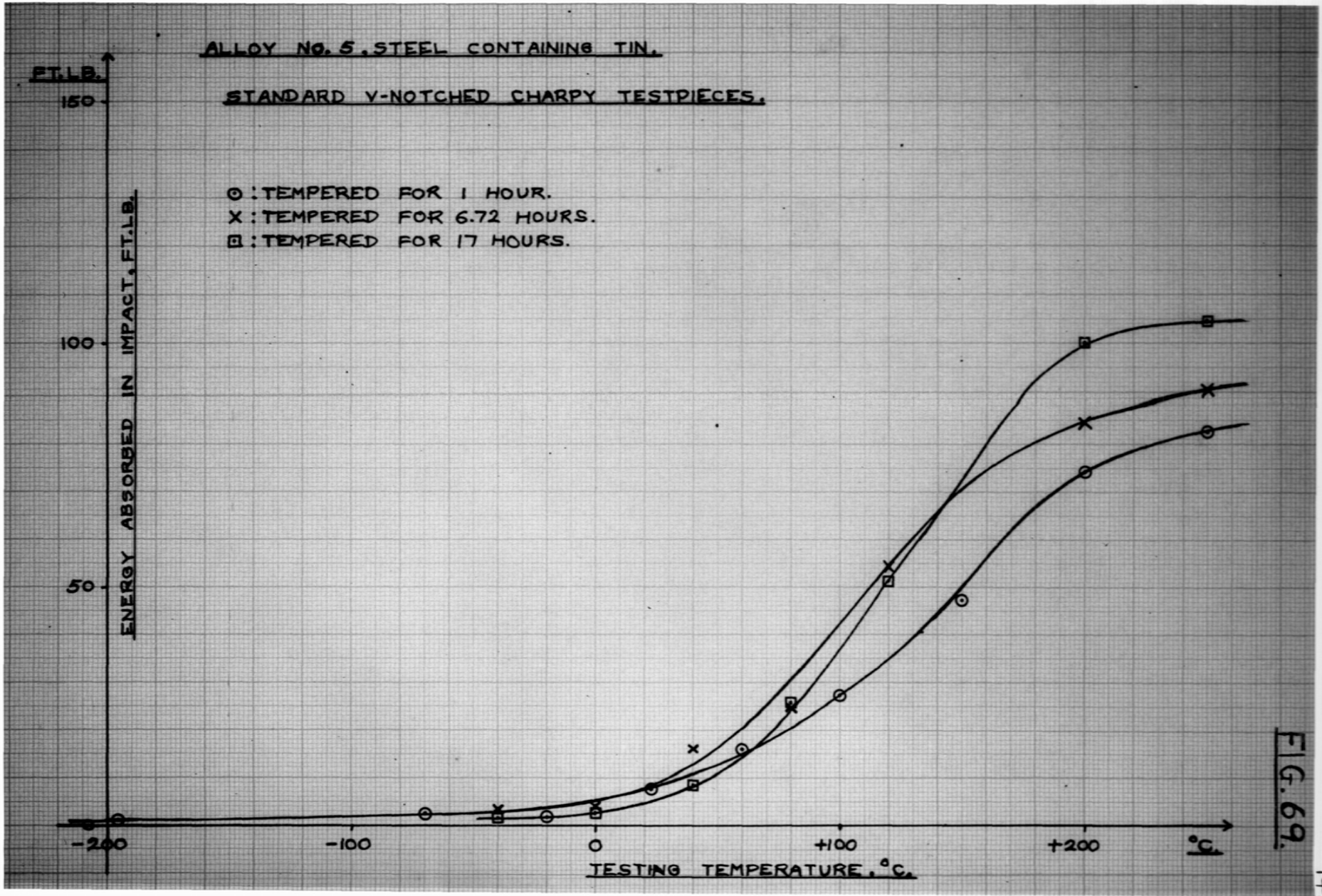

ALLOY NO. 5, STEEL CONTAINING TIN.
STANDARD V-NOTCHED CHARPY TESTPIECES.
⊙ : TEMPERED FOR 1 HOUR.
X : TEMPERED FOR 6.72 HOURS.
⊡ : TEMPERED FOR 17 HOURS.
FT.LB.
150
100
50
ENERGY ABSORBED IN IMPACT, FT.LB.
-200
-100
0
+100
+200
°C.
TESTING TEMPERATURE, °C.

FIG. 69.

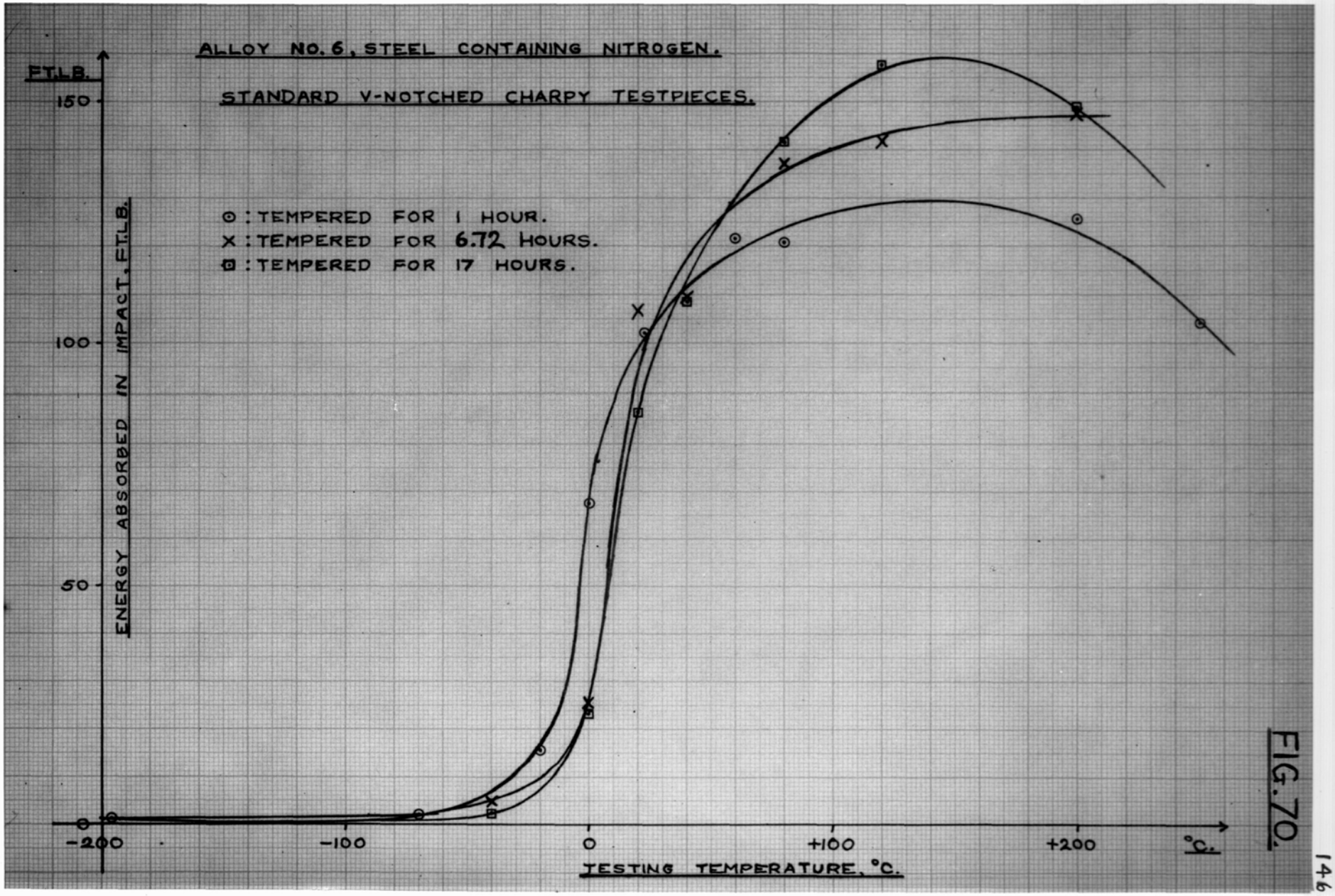

ALLOY NO. 6, STEEL CONTAINING NITROGEN.
STANDARD V-NOTCHED CHARPY TESTPIECES.
⊙ : TEMPERED FOR 1 HOUR.
X : TEMPERED FOR 6.72 HOURS.
⊡ : TEMPERED FOR 17 HOURS.
FT.LB.
150
100
50
0
ENERGY ABSORBED IN IMPACT, FT.LB.
-200
-100
0
+100
+200
°C.
TESTING TEMPERATURE, °C.

FIG. 70.

alignment with respect to the microstructural features in the steel.

In view of the fact that the steels were all difficult to machine the first possible reason cannot be discounted even though the machine was performed by R.A.R.D.E. workshops to high standards. Both the mechanisms would affect the nucleation energy but not the propagation energy since this is more likely to be affected by the microstructure encountered rather than by the mechanism of initial crack nucleation.

The graphs produced using averages of pairs of results allowed reasonably smooth curves to be constructed which suggests that the random errors were not too great.

3.2.2(i) Plain carbon steel, alloy No. 1

This alloy exhibited a very definite transition temperature which decreased slightly as the tempering time was increased from one to seventeen hours. The gradient of the curve at the transition temperature was very great and the upper region of the transition curves for 6.72 and 17 hours tempering both peaked at around 155 ft.lb. (see Fig. 65).

3.2.2(ii) Silicon steel, alloy No. 2

The presence of 2% silicon had a very great effect on the transition curves. Although the transition temperatures were decreased somewhat from those of the plain carbon steel

in the three degrees of tempering, the energy absorption was very much less (see Fig. 66). Only when tempered for one hour did the alloy produce more than 30 ft.lb. energy absorption on fracturing. However, when tempered for one hour the gradient at the transition temperature was quite small and the energy absorbed at -40°C was still significant, at 13 ft.lb_f. as compared with 3 ft.lb_f. for the plain carbon steel.

3.2.2(iii) Nickel steel, alloy No. 3

This alloy exhibited well-defined transition curves for all the studied tempering times. The transition temperatures were low and the maximum energies absorbed at higher temperatures were about 160 ft.lb_f. for tempering times of 6.72 and 17 hours (see Fig. 67).

The energy absorbed during fracture at -40°C was 25-30 ft.lb_f. which indicated that about 15% of the fracture was ductile.

3.2.2(iv) Phosphorus steel, alloy No. 4

The addition of phosphorus resulted in little change in the transition behaviour of this material. The transition temperature were around +70°C and the maximum energies were between about 100 ft.lb_f. to about 145 ft.lb_f. according to the length of time for which tempering was performed (see Fig. 68).

3.2.2(v) Tin steel, alloy No. 5

Tin had a very strong effect on the transition curves of this steel. Although the maximum energies were between 85 and 105 ft.lb$_f$., the transition temperatures had been raised intolerably so that fracture at room temperature was virtually completely brittle (see Fig. 69).

3.2.2(vi) Nitrogen steel, alloy No. 6

Nitrogen did not change the shape of the transition curve but lowered the transition temperature to around 0°C (see Fig. 70).

TABLE 5. RESULTS FROM NOTCHED BAR IMPACT TESTING

TRANSITION CURVE PARAMETERS, see Section 4.5	TEMPERING TIME, hrs.	ALLOYS					
		1	2	3	4	5	6
		plain	+Si	+Ni	+P	+Sn	+N
TRANSITION TEMPERATURE, TT (°C).	1	+70	+15	-20	+65	+140	0
	6.72	+65	+20	-5	+75	+110	+10
	17	+60	+5	-5	+75	+125	+20
ENERGY ABSORBED AT TT, E_{TT}, (ft.lb$_f$.)	1	57	28	74	51	44	66
	6.72	80	16	81	63	48	75
	17	80	13	82	74	54	81
DIFFERENCE BETWEEN PLATEAUX, ΔE(ft.lb$_f$.)	1	110	52	143	98	83	128
	6.72	155	28	157	121	91	145
	17	156	21	160	144	103	157
TRANSITION TEMPERATURE AT 15 ft.lb$_f$., TT_{15} (0°C).	1	+25	-15	-50	+15	+60	-20
	6.72	+45	+15	-55	+30	+45	-5
	17	+45	+10	-55	+35	+60	-5

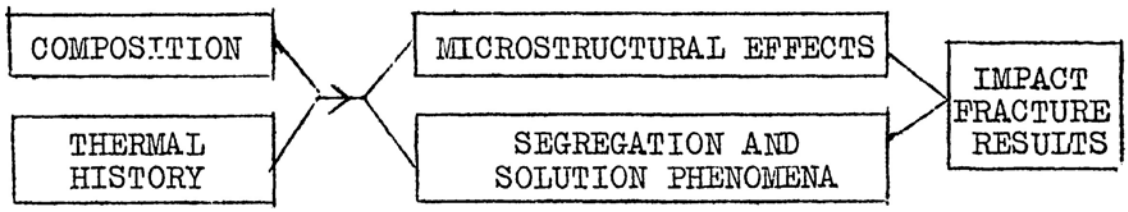
3.2.2(vii) Summary of notched-bar impact test results

The relative merits of the six alloys under impact conditions is dependent on the temperature at which their behaviours are compared. For example, at -40°C (equivalent to -40°F) the alloy exhibiting the highest degree of ductility was alloy No. 3, containing nickel, in all three states of tempering considered, which developed 25-30 $ft.lb_f$. This was followed by Alloy 2, containing silicon, which, when tempered for one hour developed 13 $ft.lb_f$. Even the steel containing nitrogen, alloy No. 6, exhibited a small amount of ductility at -40°C.

However, at +80°C the silicon steel was worse than any of the alloys except for the tin steel.

CHAPTER 4. DISCUSSION

The factors which influence the microstructure can result in changes in impact fracture properties. The inter-relationship between causes and effects is shown on the Schematic diagram below.



4.1 Composition

Six alloys were specified, allowing investigation of the effects produced by five alloying elements, silicon, nickel, phosphorus, tin and nitrogen. Each of these was present in very small amounts in each alloy where it was not supposed to predominate, and in the one where its effects were to be observed was present in considerably enhanced degree. In this way it was hoped that the effects of carbon, sulphur and manganese could be entirely neglected, and the effects of the other elements neglected in all alloys except for the ones where they predominated.

4.2 Thermal history

Because of the many possible ways of varying the heat treatment parameters, as many as possible were kept constant by the selection of suitable values as tabulated below :

(a) austenitising temperature = +950°C.

(b) austenitising time = 3 hours at temperature.

(c) quenching rate from austenitising temperature = natural convection in ice/brine mixture.

(d) lowest temperature after quenching = -196°C.

(e) tempering temperature = +650°C.

Two factors remain, namely the tempering time and the rate of cooling from the tempering temperature, which were varied.

4.2.1 Tempering times

Three tempering times were used for fracture behaviour, and two of these were used for structural observations. Even the shortest time was sufficient to give a well-tempered structure of (ferrite + cementite). The times chosen were 1 hour, 6 hours 43 minutes, and 17 hours. These are well-spaced both on linear scales and on logarithmic ones.

4.2.2 Rate of cooling from tempering temperature

The influence of the rate of cooling on the impact behaviour was briefly investigated by allowing one batch of test-pieces to cool by natural convection in air. The impact fracture ductile/brittle transition curves from this batch were compared with those from alloys which had been quenched from the tempering temperature. There was no

statistically significant difference between the two batches for any of the alloys tempered for one hour. It can be concluded therefore that mean cooling rates from 650°C of between 2.6°C/sec. and 160°C/sec. had no effect on the impact fracture behaviour of any of the alloys investigated here. This suggests that considerable variation in the cooling rate from the tempering temperature is permissible without affecting the impact behaviour noticeably.

Following these results, all further batches of specimens were quenched from the tempering temperature.

4.3 Microstructural effects

The important microstructural parameters concerned in the fracturing of well-tempered low alloy steels have been shown in Section 1.4 to be :

(a) grain size,

(b) subgrain size,

(c) carbide size.

The prior austenite grain size was maintained constant; the effects of subgrain and carbide size have therefore been examined.

4.4 Solution and segregation effects

The presence of solutes in the alloys is not visible in thin foils. In addition, segregation of solutes is not resolvable by transmission electron microscopy, unless

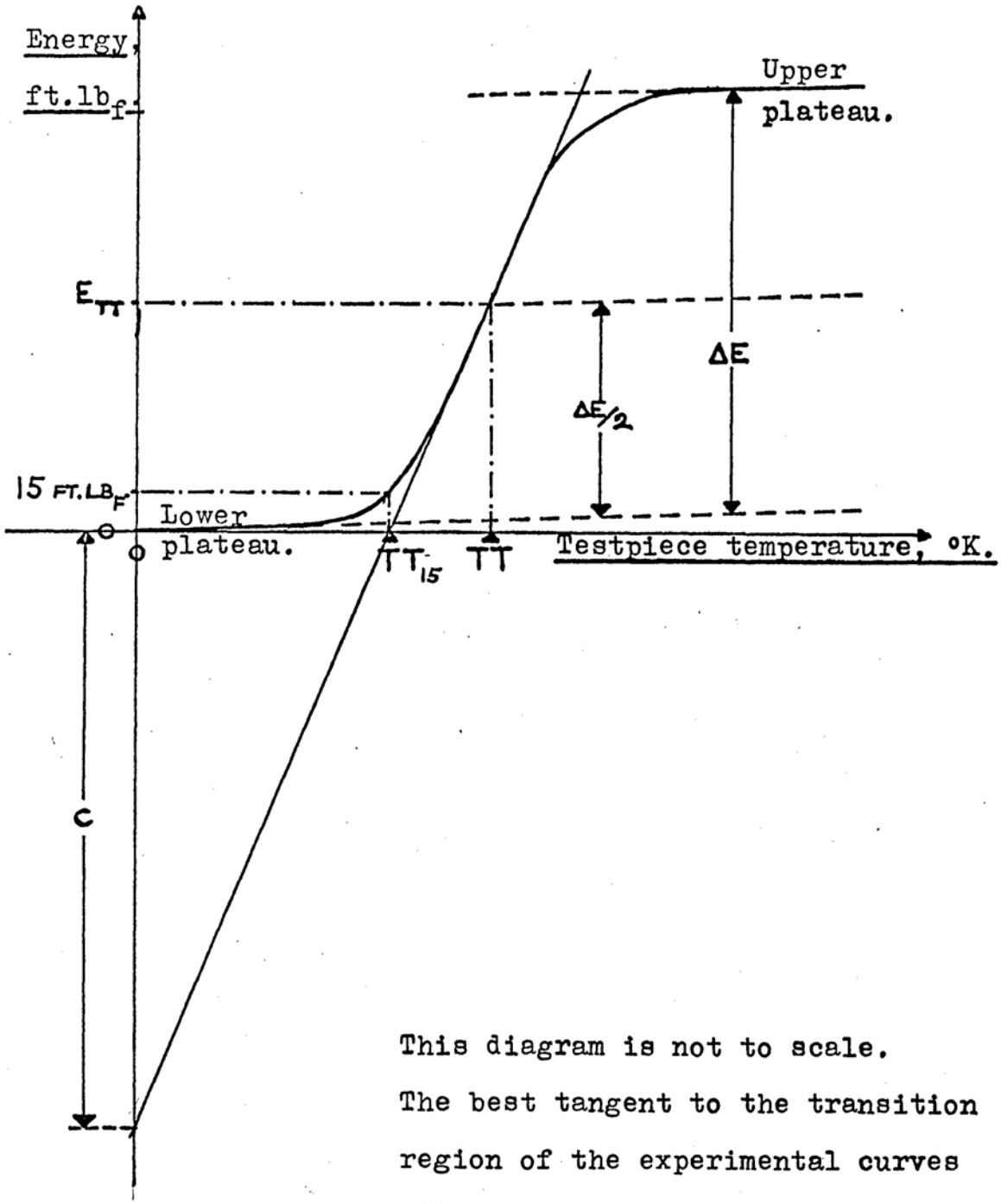
precipitates greater than approximately 20Å in size are formed. However, in these alloys, no precipitates resulting from the presence of Si, Ni, P, Sn or N were observed. Thus any effects not attributable to the microstructure could be due to effects of the solutes on the ferrite solid solution, e.g. via the Peierls-Nabarro stress, or to segregation of the solutes at interfaces in the steel.

4.5 Impact fracture characteristics

Various parameters may be used as a measure of brittleness. When the notched-bar impact test is used the most useful parameter is the transition temperature (henceforth referred to as TT.) at which the energy absorbed during fracture is halfway between the upper and lower plateaux on the transition curve (see Fig. 71). This point may be ascertained reasonably accurately for a wide range of shapes of transition curves. If there is no upper plateau, the maximum of the curve is taken. The additional energy absorption represented by the difference between the upper and lower plateaux is henceforth referred to as ΔE.

However, the transition temperature gives no information on the shape of the curve, so it is helpful to associate it with other parameters. These may be the energy dissipated during fracture (referred to as E_{TT}) at the above-defined transition temperature, and the gradient

FIGURE 71. DIAGRAM OF DUCTILE/BRITTLE TRANSITION CURVE.



This diagram is not to scale.
The best tangent to the transition region of the experimental curves often intersects the x-axis at TT_{15}, as depicted above.

of the transition portion of the curve. Respectively, these auxiliary parameters give some information concerning the value of the upper plateau (approx. = 2 x E_{TT}), and the rate at which the transition is made from the lower plateau to the upper one (or to the maximum).

The gradient used could be defined in a number of ways according to which part of the curve (upper or lower) is of interest. The one used here is a mean gradient of the lower half of the transition region and is defined as : $\left[E_{TT} / (TT - TT_{15})\right]$, which is found to be a reasonable approximation to the transition curves obtained in this investigation, as the tangent to the straight part of the transition region of the curves often intersects the x-axis at the temperature where the energy absorbed during fracture of a testpiece is 15 ft. lb_f.

If energy dissipation of less than 15 ft. lb_f. is of no interest from the engineering point of view, the part of the curves below 15 ft. lb_f. may be considered constant and negligible. The upper plateau or maximum may be viewed as the upper limit of applicability of the straight line approximation to the transition part of the curve. Hence all important information may be obtained from TT_{15}, TT, E_{TT} and ΔE; and the experimental transition curve may be approximated by a straight line between certain limits, namely $E = 0$ and $E = \Delta E$ or $2.E_{TT}$.

The gradient and the intercept at E = 0 of this approximation for any steel in any condition can give a good indication of the lower regions of the transition curve, provided that the upper limit of validity is stated. Therefore a list of straight line equations of the type $E = mT + c$, with associated upper limit of E for each one, could replace the transition curves in theoretical discussion. Such a list is given in Table 6 overleaf.

TABLE 6.

ALLOY NO.	TEMPERING TIME, hrs.	E = mT + c	ΔE	TT., °C.
1. plain carbon steel	1	1.27 T -377	110	+70
	6.72	4.00 T -1272	155	+65
	17	5.33 T -1695	156	+60
2. silicon steel	1	0.93 T -241	52	+15
	6.72	3.20 T -922	28	+20
	17	not applicable	21	+5
3. nickel steel	1	2.47 T -551	143	-20
	6.72	1.62 T -353	157	-5
	17	1.64 T -358	160	-5
4. phosphorus steel	1	1.02 T -294	98	+65
	6.72	1.40 T -424	121	+75
	17	1.85 T -570	144	+75
5. tin steel	1	0.55 T -183	83	+140
	6.72	0.74 T -235	91	+110
	17	0.83 T -277	103	+125
6. nitrogen steel	1	3.30 T -835	128	0
	6.72	5.00 T -1340	145	+10
	17	3.24 T -868	157	+20

4.6. Effects of alloying elements on fracture characteristics.

4.6.1. Effect of alloying elements on TT after tempering.

The results may be regrouped and presented as follows to clarify this effect. In Table 7 below,

$\Delta TT = TT_{alloy} - TT_{plain\ carbon\ steel}$.

TABLE 7.

TEMPERING TIME, hrs.	ALLOY	Si(2)	Ni(3)	P(4)	Sn(5)	N(6)
1	Δ TT, °C.	-55	-90	-5	+70	-70
	Δ TT/atom % alloying element	-14.3	-32.4	-107	+144	-1270
6.72	Δ TT, °C.	-45	-70	+10	+45	-55
	Δ TT/atom % alloying element	-11.7	-25.2	+214	+92.8	-995
17	Δ TT, °C.	-55	-65	+15	+65	-40
	Δ TT/atom % alloying element	-14.3	-23.4	+322	+134	-724

Silicon is seen to lower the transition temperature somewhat, the magnitude of the effect being 12 to 14 degrees C. per atom % silicon. Silicon also modified the shapes of the transition curves, however, particularly in the higher temperature regions, so that the lowered

transition temperature does not give a true picture of the effect of silicon.

Nickel (alloy No. 3) dramatically reduced the transition temperature. Its greatest effect was in the least-tempered condition when it reduced the transition temperature by 32.4 °C. per atom % nickel. When the tempering time was increased the effect of the nickel decreased slightly, to 25.2 °C. per atom % nickel after 6.72 hours and to 23.4 °C. per atom % nickel after 17 hours tempering. This indicates that the effects of nickel are not very greatly affected by the tempering duration.

Phosphorus had a beneficial effect in the earlier stages of tempering and, after one hour, reduced the transition temperature by 107 °C. per atom %. However, the element later became deleterious and, by 6.72 hours, had increased the transition temperature by 214 °C. per atom %. After 17 hours tempering this had increased to 322 °C. per atom %. Thus the small amount of phosphorus incorporated in this steel lowered the TT in the early stages of full tempering. However, in the event of over-tempering the phosphorus appeared to raise the TT by an amount which increased as tempering was continued.

Alloy No. 5 contained tin and gave consistently very high transition temperatures. For the three tempering times used here, the effect of tin was to increase the

transition temperature by 144, 92.8 and 134 °C. per atom % tin in ascending order of tempering times. The presence of significant amounts of tin in steel containing about 0.3 % carbon therefore could result in severe embrittlement.

The nitrogen steel, alloy No. 6, exhibited a consistent improvement over the plain carbon steel. The effect of the introgen appeared to decrease progressively as the tempering time was increased. It must be remembered, however, that this gas will tend to diffuse very rapidly at high temperatures, so that the long tempering treatments at 650 °C. in argon may have reduced the nitrogen content of this alloy. However, the 17-hour tempering treatment still resulted in a very significant effect. Thus, small introgen additions appear to improve toughness, although not much nitrogen can be included without compound formation.

These results may be summarised by stating that nickel and nitrogen have been found to improve toughness and phosphorus may do likewise for fairly short tempering times. However, tin embrittles consistently and phosphorus may do so if overtempered. Silicon does reduce the transition temperature but cannot be said to improve toughness as the upper regions of the transition curves are severely modified by its presence.

4.6.2 Effect of alloying elements on ΔE after tempering

In Table 8 below,

$\Delta(\Delta E) = \Delta E_{alloy} - \Delta E_{plain\ carbon\ steel}$.

TABLE 8.

TEMPERING TIME, hrs.	ALLOY	Si(2)	Ni(3)	P(4)	Sn(5)	N(6)
1	$\Delta(\Delta E)$(ft.lb.$_f$)	-48	+33	-12	-27	+18
	$\Delta(\Delta E)$/atom % alloying element	-12.5	+11.9	-251	-55.6	+325
6.72	$\Delta(\Delta E)$(ft.lb.$_f$)	-127	+2	-34	-64	-10
	$\Delta(\Delta E)$/atom % alloying element	-33.0	+0.7	-730	-132	-181
17	$\Delta(\Delta E)$(ft.lb.$_f$)	-135	+4	-12	-53	+1
	$\Delta(\Delta E)$/atom % alloying element	-35.0	+1.4	-251	-109	+18.1

Silicon additions drastically affected the transition curves and this is reflected by the substantial effect of this element on ΔE. This effect is seen to increase with tempering time and after 17 hours has reduced ΔE by 35 ft. lb.$_f$ per atom %.

Although nickel had an imitial tendency to raise ΔE substantially, on further tempering the effect became very much less and may not be significant.

Phosphorus has lowered ΔE considerably for all

tempering times as has tin.

The effects of nitrogen are not well defined but are negligible after 17 hours tempering.

4.7. Effect of alloying elements on subgrain and carbide sizes during tempering

4.7.1. Effect on subgrain size, D.

The mean subgrain diameter, D, for the plain carbon steel after tempering for one hour was 0.54 μm. which was only exceeded by the 0.60 μm. for the nickel steel. The remaining alloys had smaller subgrains in the descending order tin, nitrogen, silicon and phosphorus, the last having a subgrain diameter 76% of that in the plain carbon steel. Nickel was the only element studied which increased the mean subgrain diameter. This increase was 11% which is probably significant. After tempering for 17 hours, all the elements have reduced the subgrain size. The silicon has had the greatest effect and the subgrain diameter in that alloy was only 51% of that in the plain carbon alloy. The remaining elements in order of increasing magnitude of the reduction of subgrain size are nitrogen, tin, phosphorus, and nickel.

4.7.2. Effect on carbide length, L.

After tempering for one hour the plain carbon steel had the longest carbides, averaging 0.29 μm., and those in the nickel and nitrogen steels were closely similar.

These were followed by the phosphorus and tin alloys. The silicon steel had carbides only about one third the length of those in the plain carbon steel.

After tempering for 17 hours the carbides in all alloys except the silicon steel had increased in size relative to the plain carbon steel. The silicon, in alloy No. 2, appears to have severely impeded the growth of the carbides, which were only 31% of the length of those in the plain carbon steel. The nickel steel possessed the largest carbides followed by the phosphorus steel and then the tin one. The nitrogen steel had the same size carbides as did alloy No. 1.

Tin, phosphorus, and nickel therefore seem to have enhanced carbide growth during the later stages of tempering. Silicon still had a retarding effect on the growth of carbides even after 17 hours tempering.

4.7.3. Comparison of effects on subgrain and carbide sizes

The alloying additions have influenced the carbide parameters to a different degree to the subgrain ones. Silicon has decreased the carbide length more than the subgrain diameter, and tin had a similar effect although of smaller magnitude. Phosphorus and nitrogen had the opposite effect; while both still reducing both carbide length and subgrain area, the subgrain areas were decreased

to a greater degree than were the carbide lengths.

Thus, the alloying elements, with the exception of silicon, have all influenced the subgrain sizes more than the carbide sizes.

4.8. Microstructural changes during tempering

For carbide growth, carbon must diffuse to the carbide which is growing. In steels which are well-tempered, the diffusing carbon originates at other carbides, which are situated on grain and subgrain boundaries. Consequently it tends to diffuse along the grain and subgrain boundaries very much more readily than through the ferrite lattice itself (the activation energy for diffusion along the boundaries is very much less than that for lattice diffusion (49)). The migration of carbon along such boundaries will be affected by the presence there of segregated alloying elements.

Grain growth occurs by self diffusion of iron across grain and subgrain boundaries; the presence of solute elements segregated at these boundaries may affect this process too. Thus the variability of the microstructures of the alloys after tempering may be partly, at least, due to segregation of impurities at boundaries in the steel.

4.9. Analysis of effects of microstructural changes on impact parameters

Comparison of Tables 2 and 5 shows that the relationships between microstructural and impact parameters, if they exist, are extremely complicated. In this section an attempt is made to analyse these results in a manner which brings out more clearly the extent to which these properties are co-variant (or not, as the case may be).

The method depends upon the fact that both impact and microstructure parameters are functions of tempering time, so that each alloy follows a path in three-dimensional space. In general the x-axis will represent a microstructure parameter, the y-axis an impact parameter, and the z-axis will correspond to tempering time.

Since the microstructures were characterised at only two tempering times (1 hr. and 17 hrs.) only two points on the three-dimensional path of each alloy were available. These two points were projected onto the x-y plane and joined by a vector directed from the shorter to longer time.

In order to extend the usefulness of this approach it was found desirable to normalise each parameter with respect to the plain carbon steel (tempered for the same time) by subtraction. Thus the 'state path' for plain carbon steel was the z-axis. The normalised values of impact and microstructure parameters for each alloy are

shown in Table 9. Figs. 72-5 show the method applied to alloys 2 - 6.

TABLE 9.

Changes in parameters with respect to alloy No. 1.

ALLOY	TIME	2,Si	3,Ni	4,P	5,Sn	6,N
TT ($\pm$ 5° C.)	1	-55	-90	-5	+70	-70
	17	-55	-65	+15	+65	-40
ΔE ($\pm$ 5 ft.lb.)	1	-58	+33	-12	-27	+18
	17	-135	+4	-12	-53	+1
carbide diam. ($\pm$ 0.4 μm.)	1	-.15	-.03	-.07	-.10	-.05
	17	-.40	+.13	+.09	+.12	-.03
subgrain area ($\pm$ .07 μm.^{2})	1	-.08	+.07	-.12	-.03	-.07
	17	-.74	-.59	-.56	-.33	-.25

TT and ΔE are plotted against subgrain size, D, and carbide length, L, in turn. Clearly the upper halves of Figs. 72 and 73 and the lower halves of Figs. 74 and 75 represent embrittlement and are marked B in the Figures.

In Figs. 72 and 74 the marked quadrants correspond to the expected relationship between D and brittleness, applying the Petch relationship between yield stress and subgrain size (see section 1.2.2.). Similarly, Figs. 73 and 75 indicate the expected effect of carbide length, L, on brittleness (see section 1.4.3.).

FIGURE 72.

Relationship between ΔTT and Δ(subgrain diameter), ΔD.

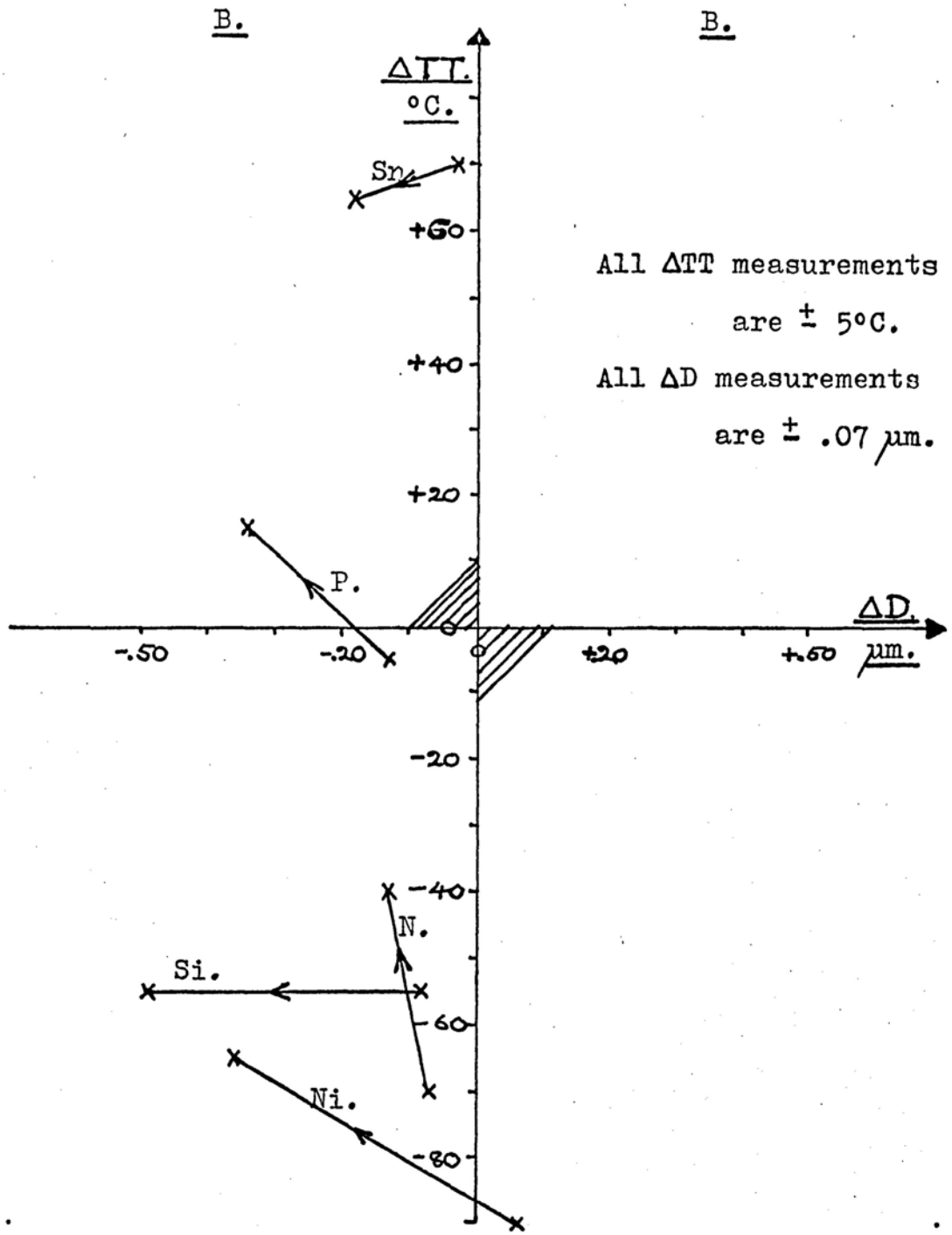


FIGURE 73.

Relationship between ΔTT and Δ(carbide length), ΔL.

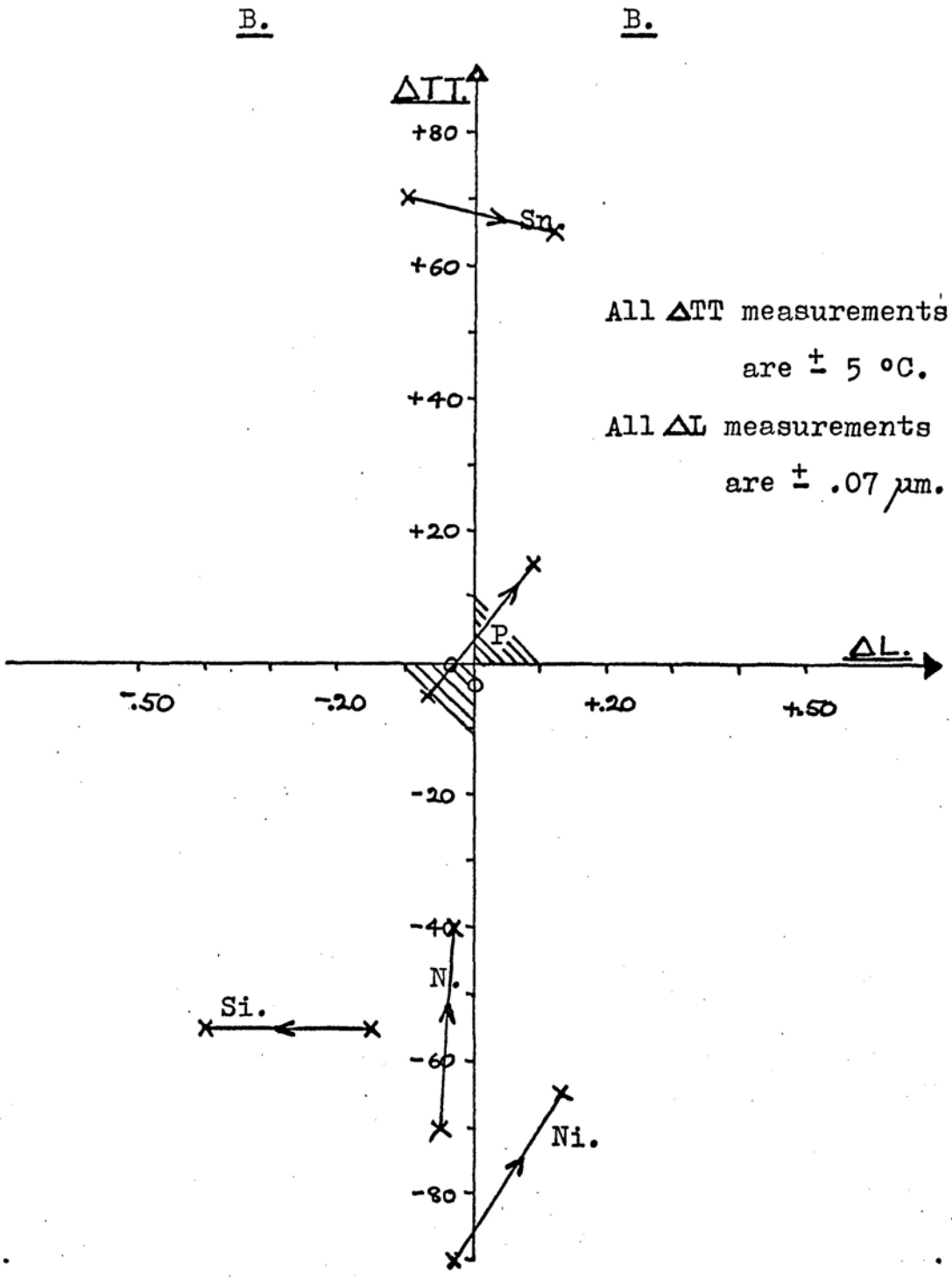


FIGURE 74.

Relationship between ΔE and Δ(subgrain diameter), ΔD.

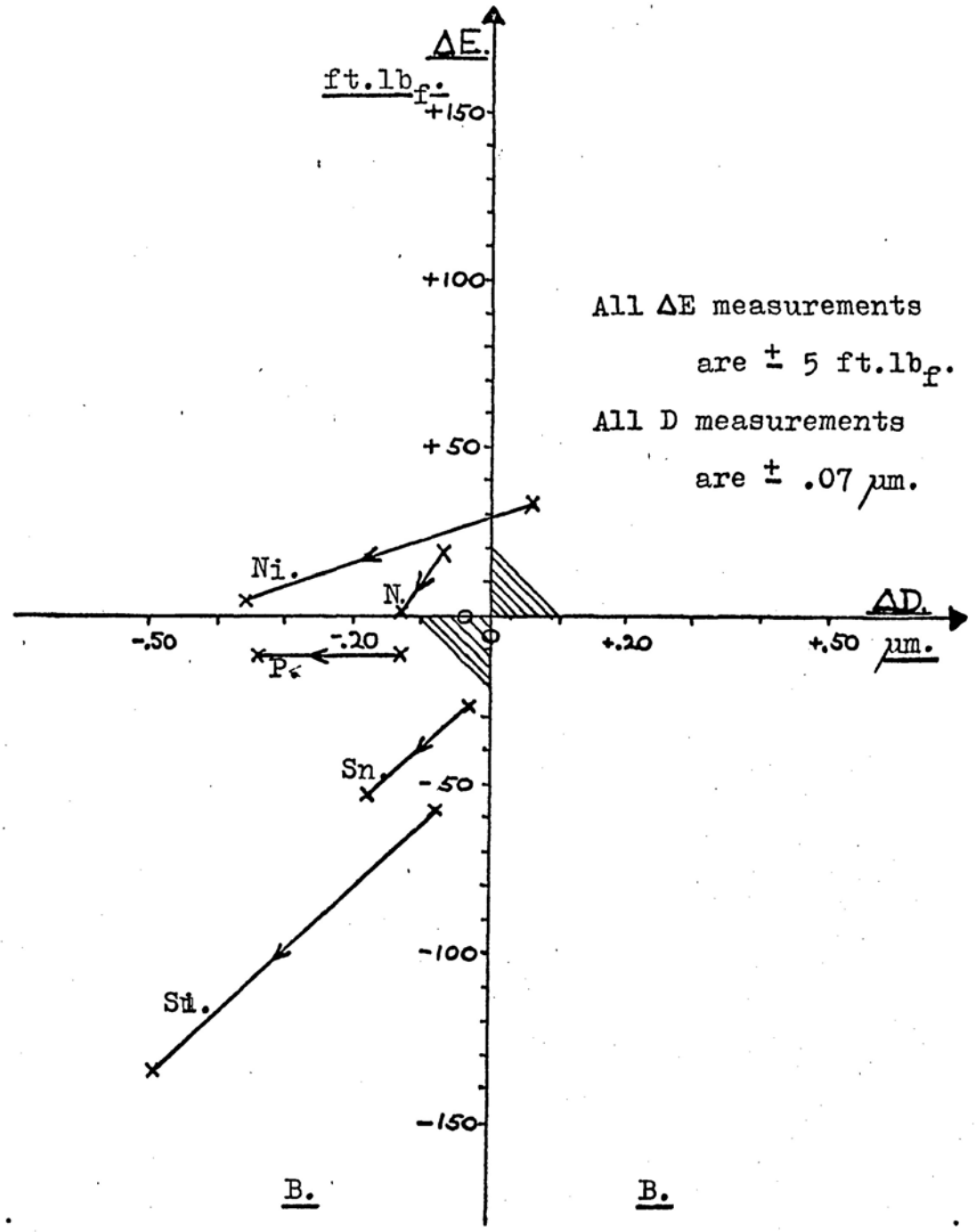
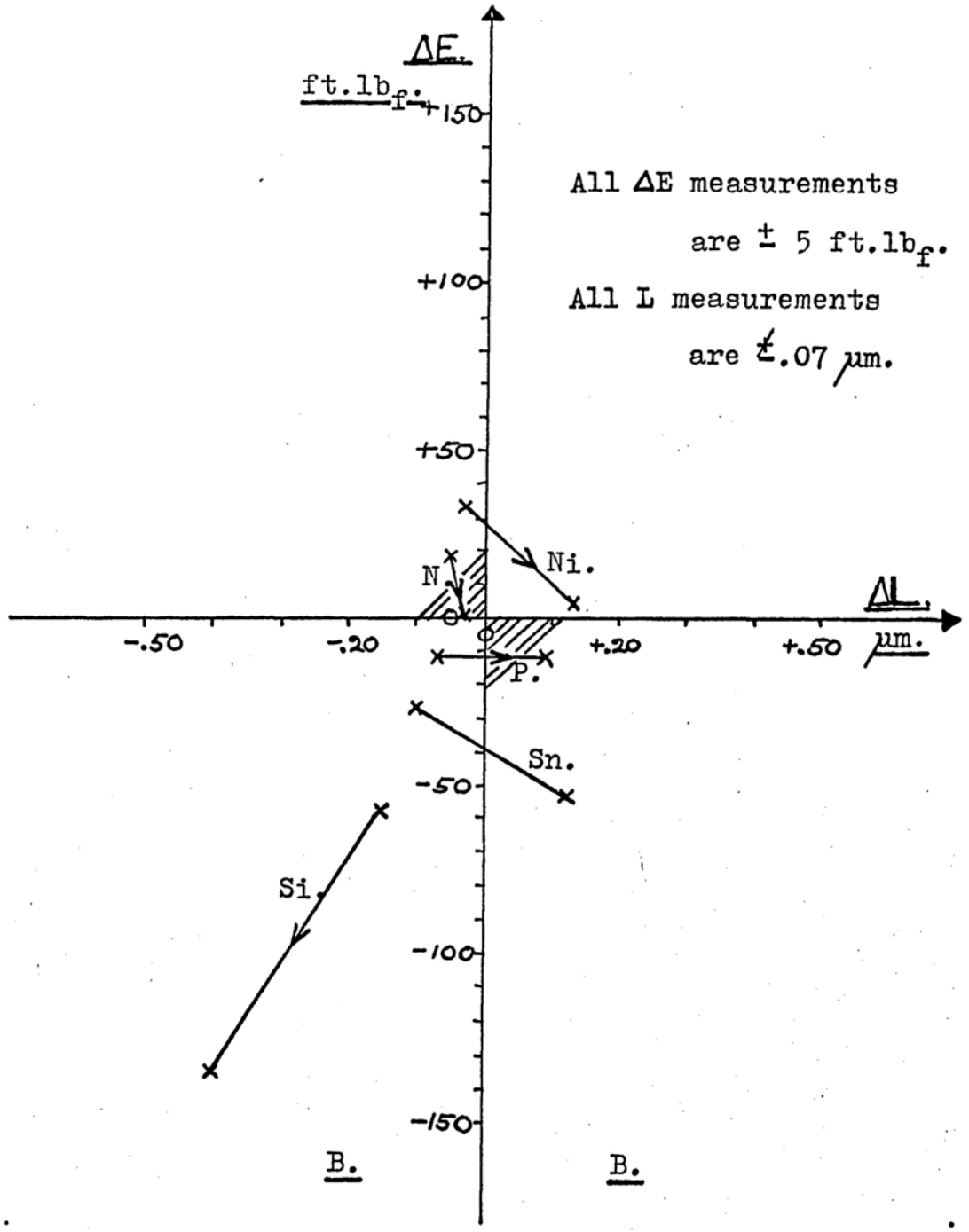


FIGURE 75.

Relationship between ΔE and Δ(carbide length), ΔL.



4.10. Effect on subgrain size on impact parameters

It can be seen from Fig. 72 that the vectors for nickel, phosphorus and nitrogen would, if transferred to the origin, lie in the second quadrant, indicating that for these elements, the subgrain diameter could be influencing the TT in the manner expected from application of the Petch model. The vectors for silicon and tin are effectively horizontal indicating that D has no effect on their TTs. Similarly, Fig. 74 shows the correct relationship to hold for each element except phosphorus whose ΔE is unaffected by D.

4.11. Effect of carbide size on impact parameters

Figs. 73 and 75 show the effect of carbide length, L, on impact properties. In Fig. 73, nickel, phosphorus and nitrogen, transferred to the origin, would lie in the first quadrant indicating obedience to the Petch relationship while silicon and tin are again unaffected. Fig. 75 shows a less satisfactory result in that only nickel and tin appear to lie in the fourth quadrant. Phosphorus appears to be unaffected by L, and the nitrogen alloy has undergone no change in relative carbide length. The behaviour of silicon in this plot is completely anomalous.

4.12. Effect of alloying elements on impact parameters

4.12.1. Silicon

Silicon has proved to be anomalous in its behaviour from the point of view of the analysis developed in section 4.9. Thus, in only one plot, that of $\triangle E$ versus D, have the results been explicable in terms of the models used. This, however, may be due to an inherent unreliability in the impact parameters themselves due to the anomalous transition curves which were obtained for this element.

4.12.2. Nickel

Both TT and $\triangle E$ were found to vary in the expected way with D and L (it must be pointed out of course, that in view of the shortage of data, such variation refers only to direction). It is at this stage, of course, not possible to separate the effects of D and L.

4.12.3. Phosphorus

Both D and L are found to influence TT in the expected direction but no change is observed in $\triangle E$.

4.12.4. Tin

Tin behaves in the opposite manner to phosphorus in that $\triangle E$ is covariant with both D and L but the change in TT is negligible.

4.12.5. Nitrogen

The relationship between D and TT has the expected direction but the changes in L are so small that the effects of this parameter are inconclusive.

4.12.6. Concluding remarks

Of the twenty possible relationships shown in Figs. 72-75, eleven are explicable in terms of the Petch relationship or the Griffith crack theory (this is not to say, of course, that these are the only possible explanations). Of the remaining nine only one is contravariant and this may be due to the generally anomalous behaviour of the silicon transition curves. The remaining eight relationships are inconclusive as one of the parameters in each case exhibits no significant change with the tempering times used.

Thus it seems reasonable to conclude that some of the variations in brittleness which occur during extensive tempering may be due merely to a change in subgrain size or carbide size rather than to such less easily characterised factors as segregation of solute elements. It is not suggested that solution and segregation effects are unimportant but that simpler microstructural features may play an important part and one which has not yet been fully evaluated.

CHAPTER 5. SUMMARY

0.3% carbon alloys containing silicon, nickel, phosphorus, tin and nitrogen have been fully hardened and tempered at 650°C. for periods of time up to 17 hours. Charpy impact specimens have been used to obtain transition curves between -196°C. and +250°C. and two impact parameters, the transition temperature and the differential plateaux energy obtained in each case.

Samples of each alloy have been examined by transmission electron microscopy, and mean subgrain diameter and carbide size have been measured.

A simple vector technique has been used to correlate microstructural and impact parameters and it has been shown that in a number of cases one or both microstructural parameters could have been responsible for the observed embrittlement or toughening.

Suggestions for future work

In view of the apparent predictability of nickel as an alloying element further work should concentrate on a detailed study of the behaviour of a simple low-carbon alloy containing this element in a range of concentrations. These alloys should be tempered for a number of different times so that the detailed behaviour of the "state path" can be examined. In this way it may be possible to

separate the effects of carbide and subgrain size and quantify them.

This approach should be combined with instrumented impact testing in an attempt to relate the dynamic yield and flow stresses during fracture to (for example) the subgrain size.

APPENDIX 1. Calculation of boundary area and close-packing saturation of this for the five alloying elements.

Let the number of subgrains in a length of 1 μm. be N;
then $N = \left\{\frac{1}{D}\right\} = \frac{1}{\sqrt{A}}$, see Fig. 76 overleaf.

Area of boundary in one-micron cube,

$$= (N \times 1 \times 1) + (N \times 1 \times 1) + (N \times 1 \times 1) = 3N = \frac{3}{\sqrt{A}}$$

From Fig. 77, the total number of atoms that could be close-packed on a surface in a monomolecular layer,

$$= \left(\frac{1}{\text{c.d.a.}} \times \frac{1}{0.866 \text{ c.d.a.}}\right) \text{ per } 1\ \mu m^2.$$

1 gm. atom Fe weighs 55.9 gm.

Density of Fe = 7.87 gm./cm^3

$\therefore$ 1 gm. atom Fe occupies $\left\{\frac{55.9}{7.87}\right\}$ cm^3.

$\therefore$ $\left(\frac{55.9}{7.87}\right)$ cm^3. Fe contains 6.02×10^{23} atoms.

$\therefore$ 1 μm^3 Fe contains $\left\{\frac{6.02 \times 7.87}{55.9} \times 10^{23} \times 10^{-12}\right\}$ atoms,

$$= (8.47 \times 10^{10}) \text{ atoms.}$$

Hence atom % solute required to give monomolecular layer on boundaries, $= \left\{\frac{3 \times 100}{0.866\ (\text{c.d.a.})^2 . \sqrt{A} \ . \ 8.47 \times 10^{10}}\right\}$

where c.d.a. and $\sqrt{A}$ are in μm.

TABLE 1C.

	Si	Ni	P	Sn	N
1	0.162	0.110	0.214	0.088	0.779
17	0.146	0.103	0.131	0.055	0.422

FIGURE 76. Schematic subgrains in a micron cube.

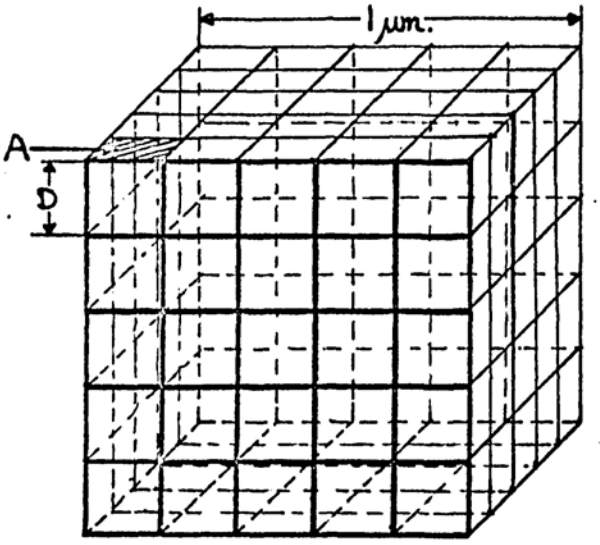
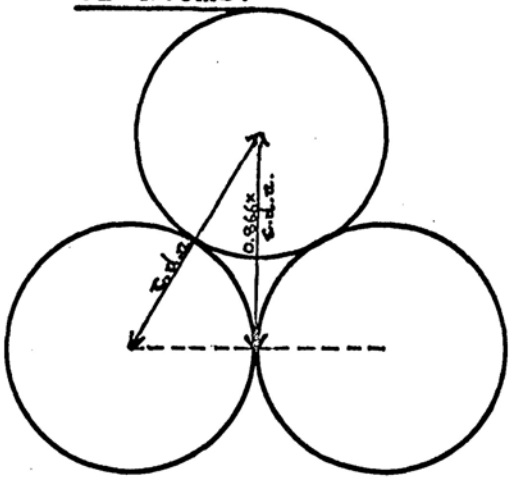


FIGURE 77. Schematic closest two-dimensional packing of atoms.



c.d.a. is the closest distance of approach of two atoms in the solid element.

APPENDIX 2.

(a) Acknowledgements

Most of the work was performed at the Department of Chemical Engineering and Chemical Technology, Imperial College, University of London. Thanks are due to Professor Ubbelohde, F.R.S., for research facilities in the above department, and especially to Dr. A. E. B. Presland for supervising the programme and giving very great assistance in the form of valuable discussions during the course of the practical work and during preparation of the thesis.

The Royal Armaments Research and Development Establishment, Fort Halstead, Kent, sponsored the research. Thanks are due, therefore, to the Director of R.A.R.D.E. and to Mr Barron for formulating and initiating the programme. Thanks are especially due to Dr. A. R. Cox of R.A.R.D.E. for helpful discussions and very valuable assistance in arranging for the machining and testing of the Charpy testpieces.

The staffs of the departmental and glassblowing workshops at I.C. and of the workshop and laboratories at R.A.R.D.E. are thanked for constructing some apparatus, loan of apparatus, machining, and testing respectively.

Finally, the receipt of a bursary from R.A.R.D.E. for two years is gratefully acknowledged.

(b) Statement

The experimental work was performed between 1st October, 1966, and 30th September, 1968. The thesis was prepared after leaving college.

(i) Work performed in person :

Design and construction of two furnaces except machining and glassblowing.

Design and construction of power supply unit.

Design of Perspex electrode holder for electropolishing.

All heat treatment.

All sectioning and electrothinning.

All electron microscopy and photomicrography (including developing and printing).

Assistance during testing of Charpy impact specimens.

(ii) Work performed by departmental workshops and R.A.R.D.E. staff :

Machining end flanges of one furnace in stainless steel.

Construction of Perspex electrode holder for electro-polishing.

Machining of Charpy Impact specimens.

Testing of Charpy Impact specimens.

Constructing one furnace of fused silica tube.

APPENDIX 3.

REFERENCES :

1. SHANK, M. E. A critical survey of brittle failure in carbon plate steel structures other than ships, in A.S.T.M. Special Technical Publication No. 158, 1953, p.45 onwards.

2. The water tower failure at Gravesend, Long Island, Engineering News (U.S.A.), Vol. 16, October 23rd, 1886, p.264.

3. ALLEN, N. P. Studies of the brittle fracture of steel during the past 20 years, in Sendai Conference, 1965.

4. PAUL, Col. Thurston T. Interest of the army in brittle failures, in A.S.T.M. Special Technical Publication No. 158, 1953.

5. WILSHAW, T. R., P. L. PRATT. The effect of temperature and strain rate on the deformation and fracture of mild-steel Charpy specimens, in Sendai Conference, Vol. 2, 1965.

6. PELLOUX, R. M. N., J. C. McMILLAN. The analysis of fracture surfaces by electron microscopy, in Sendai Conference, Vol. 2, 1965.

7. VERBRAAK, C. A. Propagation mechanism of brittle fractures in steels and weld metal as derived from ultra-high-speed photographic recordings, in Sendai Conference, Vol. 2, 1965.

8. RINEBOLT, J. A. Effect of metallurgical structures on the impact properties of steels, in A.S.T.M. Special Technical Publication No. 158, 1953.

9. HODGE, J. M., R. D. MANNING, H. M. REICHHOLD, Jnl. Inst. Metals, A.I.M.M.E., March 1949.

10. MEAKIN, J. D., N. J. PETCH. Atomistic aspects of fracture, in Met. Soc. Conferences Vol. 20, A.I.M.E., Fracture of Solids, Maple Valley, 1962.

11. SAKUI, Seita, Tsutomu Mori. Pseudo-brittle fracture of fine-grained iron and steel at impact tensile test, in Sendai Conference, Vol. 2, 1965.

12. BAEYERTZ, M., W. F. CRAIG, Jr., J. P. SHEEHAN. Effects of alloying elements on impact properties of quenched and tempered steels. Report No. 22, O.N.R. Contract N6 onr 274 T.O.I. Project NR 031-115, September 1st, 1949.

13. BAEYERTZ, M., W. F. CRAIG, Nr., E. S. BUMPS. Effect of ferrite grain structure upon impact properties of 0.80% C spheroidite. Trans. A.I.M.M.E. 188, 1950.

14. RINEBOLT, J. A., W. J. HARRIS, Jr. Effects of alloying elements on notch toughness of pearlitic steels. Trans. A.S.M., 43, 1951, p.1175.

15. WESTBROOK, J. H., D. L. WOOD. Nature, 192, 1961, p.1280.

16. AINSLIE, N. G., V. A. PHILLIPS, D. TURNBULL. Acta Met., 8, 1960, p.528.

17. LOW, J. R., Jr. Microstructural aspects of fracture, in Met. Soc. Conferences Vol. 20, A.I.M.E., Maple Valley, 1962.

18. BAEYERTZ, M., W. F. CRAIG, Jr., J. P. SHEEHAN. The notched-bar impact properties of tempered martensite in medium-carbon medium-alloy grades of steel, in A.S.T.M. Special Technical Publication No. 158, 1953.

19. GRIFFITH, A. A. The phenomena of flow and rupture in solids. Phil. Trans., Roy. Soc., London, A221, p.163, 1921.

20. OROWAN, E. Energy criteria of fracture. Weld. Jnl. Research Supplement, March 1955.

21. IRWIN, G. R. Fracture mechanics in "Structural Mechanics", Pergamon Press, 1960.

22. McLEAN, D. Mechanical properties of Metals, Wiley, 1962.

23. BARTENEV, G. M. The Mechanism of Energy Dissipation at Brittle Fracture, in Sendai Conference Vol. 1, 1965.

24. McEVILY, A. J., Jr., T. L. JOHNSTON. The role of cross-slip in brittle fracture and fatigue, in Sendai Conference Vol. 2, 1965.

25. GRUNTFEST, I. J. A note on thermal feedback and the fracture of solids, in Met. Soc. Conferences Vol. 20, Fracture of Solids, A.I.M.E., Maple Valley, 1962.

26. CRUSSARD, C., R. BOROINE, J. PLATEAU, Y. MORILLON, F. MATRAY. J.I.S.I., 183, 1956, p.146.

27. ZENER, C. Fracturing of Metals, Am. Soc. Metals, Cleveland, Ohio, 1948, pp.3-31.

28. CAHN, R. W. J. Inst. Metals, 83, 1955, p.493.

29. HULL, D. U.K. Atomic Energy Report R.2918, 1959.

30. ARGON, A. S., E. OROWAN. Nature, 192, 1961, p.447.

31. OROWAN, E., in Cohen, M., editor, Dislocations in Metals, A.I.M.E., N.Y., 1954, p.69.

32. HULL, D. Twinning and the nucleation of cracks in b.c.c. metals. A chapter in Fracture of Solids, Met. Soc. Conferences, Vol. 20, Maple Valley, 1962, A.I.M.E.

33. OWEN, W. S., D. HULL, in Semchyshen M., and I. Perlmutter, editors, Refractory Metals and Alloys, II, Interscience, N.Y., 1963, p.1.

34. SMITH, S. W. J., A. A. DEE, J. YOUNG. Proc. Roy. Soc. (London), A.121, 1928, p.477.

35. SMITH, E. Fracture at stress concentrations, in Sendai Conference, 1965, Vol. 1.
(Japanese Society for Strength and Fracture of Materials, Proceedings of the First International Conference on Fracture, 3 volumes, published 1966.
Editors: T. Yokobori, T. Kawa Saki, J. L. Swedlow.)

36. TETELMAN, A. S. The plastic deformation at the tip of a moving crack, in Fracture of Solids, Met. Soc. Conferences Vol. 20, A.I.M.E., Maple Valley, 1962.

37. BAIN and PAXTON. Alloying elements in steels. A.S.M.

38. KAY. Techniques for electron microscopy. 2nd edition.

39. Balzers High Vacuum Ltd. Private communication.